ISBN ISBN 978-82-471-3424-5 (printed ver.)
ISBN ISBN 978-82-471-3426-9 (electronic ver.)
ISSN 1503-8181

Doctoral theses at NTNU, 2012:76

Anders Løvstad

Detection of localised corrosion in pipes using guided waves

NTNU
Norwegian University of
Science and Technology
Thesis for the degree of
philosophiae doctor
Faculty of Information Technology, Mathematics and
Electrical Engineering
Department of Electronics and Telecommunications

NTNU
Norwegian University of
Science and Technology

Doctoral theses at NTNU, 2012:76

NTNU

NTNU
Norwegian University of
Science and Technology

Anders Løvstad

Detection of localised corrosion in pipes using guided waves

Thesis for the degree of philosophiae doctor

Trondheim, February 2012

Norwegian University of
Science and Technology
Faculty of Information Technology, Mathematics and Electrical Engineering
Department of Electronics and Telecommunications

NTNU
Norwegian University of
Science and Technology

NTNU
Norwegian University of Science and Technology

Thesis for the degree of philosophiae doctor

Faculty of Information Technology, Mathematics and Electrical Engineering
Department of Electronics and Telecommunications

ISBN ISBN 978-82-471-3424-5 (printed ver.)
ISBN ISBN 978-82-471-3426-9 (electronic ver.)
ISSN 1503-8181

Doctoral Theses at NTNU, 2012:76

Printed by Fagtrykk Trondheim AS

Abstract

The work in this thesis is motivated by a need to improve non-destructive testing (NDT) techniques as petrochemical production moves towards harsher environments, with increasing presence of CO_2 and/or H_2S in the production lines, which in turn lead to an increasing risk of shutdown due to localised corrosion. From a practical NDT point of view, the maximum corrosion depth within the area inspected is the most important parameter to quantify accurately. However, localised corrosion exhibits a large scatter in shape and growth rate, making it insidious and difficult to detect and size in practice.

Initially, relatively simple shaped defects such as infinite notches and single through-thickness holes in plates are considered, comparing the reflection and scattering from them with available results from the literature for validation, before attention is given to more complex defects in pipes, with the fundamental torsional guided wave, T(0,1), incident.

Firstly, a parametric study of the reflection from two and three small circular holes is presented. FE analyses estimating the reflection coefficients (RC) for both part- and through thickness holes at different relative positions are presented, and the validity limits of employing the superposition technique in doing so assessed. Results show that the RC for the T(0,1) mode is dependent on absolute frequency and axial separation, and independent of circumferential position of the holes. Employing superposition is found to be valid down to defect centre to centre separation distances of two diameters in the worst case, with improved validity with shallower defects.

Then the reflection of the T(0,1) mode from a large number of pit clusters consisting of a random number of pits that have developed randomly in size and depth following certain growth rules is investigated, assessing the relationship between maximum pit depth and maximum RC. Problematic cases where low maximum RCs are obtained from pit clusters with deep maximum pit depth are investigated in detail. Results show that the majority of such clusters consist of a single small and deep pit, with otherwise shallow attack only; such corrosion morphologies are unlikely to occur in practice. With more realistic pit cluster morphologies, where the pit clusters are part of a larger, wider corrosion attack, fewer cases with deep maximum pit depth result in a low maximum RC.

A 2D FFT approach is used to further assess the problematic features identified by studying the relationship between the spatial frequencies of corrosion patches and their RC spectra. Results indicate that sharp changes in depth result in significant reflections at high frequencies, and only to a minor extent affect RCs at lower frequencies. A subsequent analysis of whether pit clusters with sharp sided pits can be represented as a single, complex defect showed that it is not a valid approximation; as a consequence of the poor agreement found, the maximum depth of the problematic corrosion profiles cannot be well estimated without consideration of the high spatial frequency content of the corrosion profiles.

Preface

This thesis is submitted to the Norwegian University of Science and Technology (NTNU) for partial fulfilment of the requirements for the degree of Philosophiae doctor (Ph.d.).

The research work was done from January 2008 to October 2011 at the Dept. of Electronics and Telecommunications, NTNU, Trondheim, Norway, with Prof. Hefeng Dong as main supervisor, and Prof. Ulf Kristiansen as co-supervisor. During this time I spent around 17 months as a visiting Ph.d. student at the NDT group, Dept. of Mechanical engineering, Imperial College, London, UK, under the supervision of Prof. Peter Cawley.

The work is financed through SINTEF project no. 805108 SmartPipe, which is supported by a consortium of industrial partners: Bredero Shaw, British Petroleum, Conoco Philips, Eni, Force technology, Gassco, NTNU, Roxar, Shell, Sicom, SINTEF, The Research Council of Norway, and Total.

Acknowledgements

I am most grateful to my supervisor Prof. Hefeng Dong for her support and faith in me throughout this project, despite us being in different parts of the world for longer time periods. Likewise, my co-supervisor Prof. Ulf Kristiansen deserves credit for his help, especially during the early stages. Furthermore, I would like to thank everyone at the acoustics group at IET, NTNU for discussions and a pleasant working environment. Special thanks go to Dr Tarjei Rommetveit and my office mates Dr Assaf Mar-Or and Mr Erlend Viggen; also Dr Henrik Tollefsen for his friendship.

I would also like to thank Prof. Roy Johnsen at DMSE, NTNU for helpful contributions and discussions on corrosion science and material degradation, and likewise to Dr Ole Øystein Knudsen at SINTEF and Mr Per Olav Gartland at Force Technology. I would also like to thank Multiconsult AS, and especially the acoustics group.

A significant part of the work leading to this thesis was done at the NDT group at Imperial College, London, UK. My deepest thanks and gratitude goes to Prof. Peter Cawley for his insightful guidance and support, and for making me feel like a true member of the NDT lab from day one; also, it is not unlikely that I will pay some extra attention to the well-being of the Owls in the future.

The work on complex defects would not have been so enjoyable and good without the daily collaboration with Dr Carandente, whose friendship, inspiring demeanor and love for coffee has been much appreciated; although she must expect regular orders of Kimbo as a consequence.

Many thanks to all the people in the NDT lab, especially Drs Prabhu Rajagopal, Fred Cegla, Jian (Ken) Ma, Jake Davies, and Pierre Belanger for discussions, assistance and friendship during my stay at Imperial. The experimental work would not have been possible without assistance from Mr David Tomlin and Mr Guljar Singh at the Mechanical Engineering workshop, and Drs Jimmy Fong and Alessandro Demma at Guided Ultrasonics Ltd.

For inspiration and never-ending support, I would like to thank my father, mother, and brother. Finally, this work could not have been done without the continuous belief, encouragement and love of Karen, who have sacrificed at least as much as I have in order for this thesis to happen.

Contents

Chapter 1

Introduction

The current trend in the offshore petroleum industry is to move operational activities to harsher environments with higher pressure, temperatures and depth, all of which, in addition to economical moves towards multi-phase transportation through subsea completions and the use of long infield pipelines, increase the risk of corrosion [1]. Corrosion in oil and gas pipelines occurs in many forms, among which CO_2 (sweet) and/or H_2S (sour) corrosion are the most common. Production in environments with CO_2/H_2S present always imply a risk of material damage and shutdown due to corrosion attack, and then especially localised corrosion [2]. In fact, the majority of oilfield corrosion failure results from CO_2 (sweet) corrosion of carbon and low alloy steels [1]. One of the main causes of degradation of subsea pipelines is internal pitting corrosion [3], which has a random and complex nature [4], and is difficult to detect using conventional inspection methods.

The economic and environmental impact of a subsea pipeline failure can potentially be enormous. The risk of pipeline failure due to corrosion can be mitigated by educated choice of pipeline material, and by inspection monitoring the structural state of the pipelines. The work in this thesis is done as a part of the SmartPipe project, which is a SINTEF administrated project, funded by a consortium of industrial partners [5]. The vision of SmartPipe is to develop and implement a self-contained, on-line system consisting of distributed sensor packages with locally produced power and wireless communication, reporting the technical condition of the pipeline. Figure 1.1 shows the basic idea, with sensor belts mounted periodically along the length of the pipeline. The sensors are intended to provide measurements that can be used (a) directly to monitor degradation (e.g. wall thickness reduction) and (b) as input to flow degradation models.

Corrosion attacks are commonly divided into two main groups: uniform/ general and localised corrosion. General corrosion is defined as corrosion that proceeds at about the same rate over a metal surface and consequently results in approximately even reduction in thickness over the surface, and is assumed to

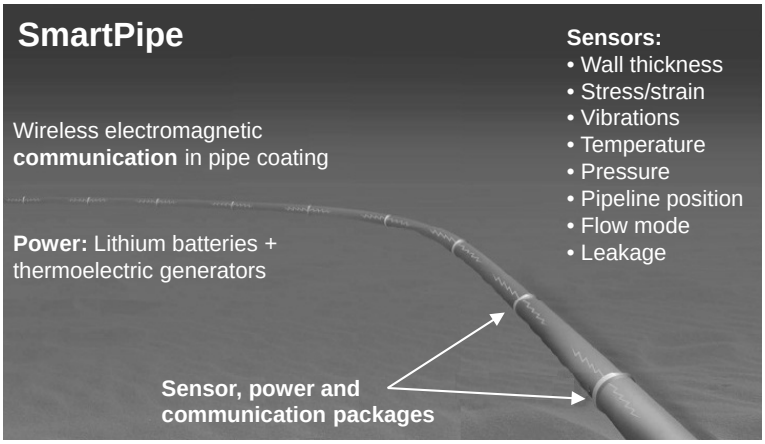

Figure 1.1: SmartPipe project outline.

be the most widespread type of corrosion, and the type that leads to the largest material loss [6]. On the other hand, it is relatively easy to predict, prevent and measure, and is thus not the most dangerous and insidious corrosion type with respect to possible leakage or fatigue. In contrast, localised corrosion occurs at discrete sites, and may deviate both in geometry and appearance compared with uniform corrosion. Localised attacks can be classified either by appearance of the corroded surface or by mechanism. The former is considered the most convenient, as classification by mechanism can be difficult, as it in some cases can be unknown [2]. The advantage of such a classification is that a corrosion failure can be identified as a certain corrosion form by visual inspection, after which necessary steps to a complete diagnosis can be made since each form of corrosion has its characteristic causes [6].

Inspection of structures in service usually requires the implementation of non-destructive testing (NDT) techniques. Presently, pipeline integrity is primarily obtained using a limited number of ultrasonic sensors that only cover a small area in the vicinity of each sensor, which is a slow process that becomes very expensive if large structures are to be inspected, and also results in partial coverage only, which makes localised corrosion difficult to detect. Use of an internal probe (pig) that runs through the pipe length is another option, a method that requires shut-down in production during inspection. This thesis investigates the use of guided waves as non-destructive testing and evaluation technique. Guided waves will not be employed in the SmartPipe project as such, so the work presented in this thesis stands on its own with respect to the project implementation.

One of the main advantages of guided wave techniques is that they enable long-range screening of pipelines, which will be focused on in this thesis,

mainly using frequencies below 100 kHz. Guided waves are frequently divided into three regimes, each of which has been extensively researched: short range ($\ll 1$ m), medium range (up to about 5 m), and long range (up to around 100 m) [7]. With guided waves, lengths of pipelines may be buried, coated, or in other ways practically inaccessible, none of which necessarily limits the applicability of guided waves as they can propagate in the pipe material itself with minimal attenuation. The possible cost reduction by applying guided waves for inspection of pipelines is therefore significant. Rose gives an introduction to the theory and application of guided waves [8], and has also outlined the history of their use, and the future potential of this type of inspection [9].

Figure 1.2: Practical guided wave testing.

The Imperial College NDT group, and latterly the spin-out company Guided Ultrasonics Ltd. [10], has developed a practical guided wave screening technique designed for the inspection of long lengths of pipes for corrosion, which also will be employed in all experimental work in this thesis. It seeks to detect corrosion defects removing of the order of 5–10% of the cross sectional area of the pipe at a given axial location, and was developed for use on pipes in the 2–24 in. diameter range, though this range can be extended [7]. Demma et al. [11] did a parametric study of the reflection of the fundamental torsional guided wave from notches in pipes, finding removal of cross-sectional area of about 2% is what can be expected to be detected in a relatively clean pipe, though this can be improved by focusing [12, 13]. Figure 1.2 shows a practical testing situation, where a transducer ring from Guided Ultrasonics Ltd. [10] is mounted onto a pipeline, scanning roughly 25 m in each direction in this case.

Applying guided waves not only for defect screening, but also for defect sizing is highly desirable, but requires detailed knowledge about the interaction of the incident wave with different possible defect types in order to interpret

the reflections from them correctly, into which much research has been devoted [7, 9, 11–21]. Understanding the scattering from various relatively simple defect shapes, such as cracks [15, 22, 23], notches [11, 17], circular holes [24, 25], and ellipses [26], is a necessity in order to understand the reflection from more complex defect shapes and/or multiple defect attacks commonly encountered. Also, real corrosion patches can often be well represented by simpler defect shape approximations.

The work in this thesis is concentrated on localised corrosion, and in particular

- pitting corrosion, which may be of different shape, but frequently develops within a narrow and covered area, but with a sharp boundary onset,
- mesa corrosion, which is a variation of pitting occurring in CO_2 environments, and
- pit clusters, which is a group of pits developing in the immediate vicinity of each other [2, 6].

Many authors have contributed to the discussion on pit initiation and growth in carbon steels, but no generally applicable rule for its prediction has been found [1]; pit growth remains difficult to predict [6]. Localised corrosion in general show a large scatter in measurable parameters (corrosion rate, maximum pit depth, etc.), leading some authors to suggest that pitting corrosion is a random process over time [4]. A discussion of certain detail on practical geometrical parameters of the defects to be studied is provided in the relevant subsequent chapters, which is intended as a validation of the practical usefulness of the analyses done. Short literature reviews on guided wave research are also given in the various chapters.

1.1 Thesis outline

This chapter outlines the framework and background of the work in this thesis. The motivation for the study is to add to the understanding of the reflection and scattering of guided waves, and their possibilities and limitations in detecting localised corrosion in various structures.

Chapter 2 reviews the theoretical background and basic principles of guided wave propagation. Following an initial discussion of bulk waves, properties of guided waves in hollow cylinders and plates are addressed. Then relationships between guided waves in plates and pipes are given, following the work by Velichko et al. [27], before fundamentals of finite element (FE) modelling of guided wave propagation are outlined in the last section of the chapter.

Chapter 3 concerns the reflection and scattering of guided waves in plates. After a short initial discussion on previous work, the reflection from an infinitely long rectangular notch is investigated, following earlier work by Lowe et al.

[28, 29] and Demma et al. [30]. The motivation behind this work is to provide an understanding of the influence of modal properties on the reflection of guided waves, as well as it serves as an initial validation study for the FE modelling. The subsequent section of the chapter investigates the scattering of a plane S_0 mode wave from a through-thickness circular hole in a plate, following the work of Diligent et al. [31] in detail, and also comparing the FE results with the analytical results of Cegla et al. [32], in order to validate the FE model and post processing implementations. Finally, a similar study as with the plane S_0 wave is done with the fundamental shear horizontal mode, SH_0, incident.

In chapter 4, attention is given to the reflection from two- and three small, circular holes in a pipe with the fundamental torsional mode, T(0,1), incident. The reflection from both part- and through-thickness holes is investigated as a function of their relative positions. In doing so, the applicability limits of using a superposition approach to estimate the reflection coefficient from the holes are assessed. Analyses are done using FE, and the main results are validated experimentally. This chapter is an extended version of a paper published in NDT&E International [25].

Following the work in chapter 4, chapter 5 assesses the reflection of the T(0,1) mode from randomly developed pit clusters in a pipe. Both clusters developing in areas affected by general corrosion only and clusters being part of a larger attack are investigated. Clusters that prove to be problematic to detect from a practical NDT point of view are given special attention. The main results are validated experimentally. The chapter is an extended version of a paper published in NDT&E International [33].

Chapter 6 investigates the influence of sharp edges in corrosion profiles on the reflection of the fundamental torsional guided wave. This is done by employing a two-dimensional FFT technique to analyse the reflection from different spatial frequency components of given corrosion patches. A superposition approach that filters the defect geometries in the wavenumber domain is investigated in an attempt to assess the relationships between the observed reflection coefficients and the physical properties of the guided wave scattering. An investigation of the validity of representing pit clusters as single, complex defects is also carried out. Parts of the chapter are included in a paper submitted to NDT&E International [34].

Finally chapter 7 outlines the main conclusions and findings of the thesis, and provides suggestions for future work.

Chapter 2

Theoretical background

This chapter outlines the theoretical background and basic principles of guided wave propagation needed in order to understand the discussion and analyses in subsequent chapters. Firstly, properties of bulk wave propagation are discussed in Section 2.1. Guided wave propagation in hollow cylinders is then outlined in Section 2.2, before guided wave propagation in plates is discussed more briefly in Section 2.3. Section 2.4 discusses relationships between guided waves in plates and pipes, as analytical analyses of the scattering from defects in plates are used for initial verification of finite element (FE) simulations in later chapters. Section 2.5 provides a brief discussion of finite element (FE) meshing rules and explicit time stepping.

2.1 Bulk wave propagation in isotropic media

Bulk waves refer to wave propagation in infinite media, i.e. waves that travel inside the material, so that there is no need for boundary conditions in their descriptions. This is the main difference between bulk and guided waves, as guided waves require a boundary for their existence. However, bulk and guided waves are governed by the same set of partial differential equations. The difference in their mathematical solutions is due to the boundary conditions that necessarily must be applied for guided wave propagation.

Bulk waves are considerably easier to understand and use compared with guided waves, as only two types of bulk waves exist: shear and longitudinal. As the waves propagate in the bulk of the material, their propagation is uncoupled. The propagation and theory of elastic waves in infinite isotropic media is well-documented and available in many textbooks [8, 35, 36]. By neglecting any external body forces, Euler's equation of motion can be derived from Newton's second law and the conservation of mass within a linearly elastic solid as

$$\rho \frac{\partial^2 \mathbf{u}}{\partial t^2} = \nabla \cdot \sigma, \tag{2.1}$$

where $\mathbf{u}$ is the particle displacement in a material with constant density ρ, and σ is the stress tensor. Hooke's law relates the stress σ to the strain ε, and is in an isotropic material given as

$$\sigma_{ij} = \lambda\delta_{ij}\varepsilon_{ij} + 2\mu\varepsilon_{ij}, \tag{2.2}$$

where $i, j \in (x, y, z)$, λ and μ are the two Lamé constants [35], δ_{ij} is the Kronecker delta function defined as $\delta_{ij} = 1$ if $i = j$ and 0 if $i \neq j$, while the strain tensor is given by

$$\varepsilon_{ij} = \frac{1}{2}\left(\partial_i u_j + \partial_j u_i\right). \tag{2.3}$$

By expressing the strain tensor of equation 2.2 in terms of displacement, and combining it with equation 2.1, Navier's equation of motion for elastic, isotropic media is obtained in vector form as

$$(\lambda + \mu)\,\nabla\left(\nabla \cdot \mathbf{u}\right) + \mu\nabla^2\mathbf{u} = \rho\frac{\partial^2\mathbf{u}}{\partial t^2}, \tag{2.4}$$

where the first and second term on the left hand side corresponds to the compressional and rotational part of the solution, respectively.

By employing the Helmholtz decomposition, the displacement may be expressed as the sum of a scalar compressional gradient, φ, and the curl of a vector potential, $\mathbf{H}$, where $\mathbf{H}$ has zero divergence, that is

$$\mathbf{u} = \nabla\varphi + \nabla \times \mathbf{H}, \tag{2.5a}$$

$$\nabla \cdot \mathbf{H} = 0, \tag{2.5b}$$

where φ and $\mathbf{H}$ are the scalar and vector potentials, respectively. Substitution of equations 2.5 into equation 2.4 gives

$$\nabla\left[(\lambda + 2\mu)\,\nabla^2\varphi - \rho\frac{\partial^2\varphi}{\partial t^2}\right] + \nabla \times \left[\mu\nabla^2\mathbf{H} - \rho\frac{\partial^2\mathbf{H}}{\partial t^2}\right] = 0. \tag{2.6}$$

In order for equation 2.6 to be fulfilled, both terms in the square brackets on the left hand side must equal zero. The resulting equations are commonly referred to as the Helmholtz differential equations, and are given as

$$\nabla^2\varphi - \frac{1}{c_\mathrm{l}^2}\frac{\partial^2\varphi}{\partial t^2} = 0, \tag{2.7a}$$

$$\nabla^2\mathbf{H} - \frac{1}{c_\mathrm{s}^2}\frac{\partial^2\mathbf{H}}{\partial t^2} = 0, \tag{2.7b}$$

where c_l and c_s are the velocities for the longitudinal (compressional) and shear (rotational) waves, given by

$$c_\mathrm{l} = \sqrt{\frac{(\lambda + 2\mu)}{\rho}}, \tag{2.8a}$$

$$c_\mathrm{s} = \sqrt{\frac{\mu}{\rho}}. \tag{2.8b}$$

Equations 2.7 are independent of each other, from which it follows that longitudinal and shear (or torsional) waves propagate independently of each other.

Solutions to equations 2.7 are frequently given [37] in the form

$$\varphi = A_{\mathrm{l}} \mathrm{e}^{\mathrm{i}(\mathbf{k}_l \cdot \mathbf{r} - \omega t)}, \tag{2.9a}$$

$$\mathbf{H} = A_{\mathrm{s}} \mathrm{e}^{\mathrm{i}(\mathbf{k}_s \cdot \mathbf{r} - \omega t)}, \tag{2.9b}$$

where A_{l} and A_{s} are the longitudinal and shear wave amplitudes propagating in any direction $\mathbf{r}$, and $\mathbf{k}_{\mathrm{l}}$ and $\mathbf{k}_{\mathrm{s}}$ are the wavenumber vectors. The wavenumber in the direction of propagation is given by

$$k_{\mathrm{l,s}} = \frac{\omega}{c_{\mathrm{l,s}}}, \tag{2.10}$$

and ω is the angular frequency given by $\omega = 2\pi f$, while c_{l} and c_{s} are the longitudinal and shear wave velocities, as given by equations 2.8.

2.2 Guided waves in hollow cylinders

The main difference between bulk and guided waves is that guided waves require boundaries for their existence. Consequently, bulk waves have no boundary conditions that need to be satisfied, while guided waves must satisfy both the governing equations of motion as well as the boundary conditions of the specific problem. Boundary conditions lead to considerable complexity in the solution and calculation of guided waves, and make guided wave propagation significantly harder to solve analytically; in some cases exact solutions cannot even be obtained. Also, there are potentially an infinite number of modes present in a guided wave problem in contrast to a finite number present for bulk waves.

Guided waves in solid cylindrical structures were first investigated mathematically by Pochhammer [38] and Chree [39] in the late nineteenth century. In the middle of the twentieth century Gazis [40, 41] presented a general analytical solution for three-dimensional wave propagation and dispersion curves in hollow, circular cylinders of infinite extent, which was validated experimentally by Fitch [42] shortly after.

As the Helmholtz decomposition is separable in cylindrical coordinates, the solutions to Navier's equation of motion can be expressed as the product of the spatial dimensions in cylindrical coordinates. For a harmonically oscillating source, we get

$$\varphi, \mathbf{H} = \Gamma_{\varphi,\mathbf{H}}(r)\Gamma_{\varphi,\mathbf{H}}(\theta)\Gamma_{\varphi,\mathbf{H}}(z)\mathrm{e}^{\mathrm{i}(\mathbf{k}\mathbf{r} - \omega t)}, \tag{2.11}$$

where the spatial coordinates (r, θ, z) are indicated in figure 2.1, and $\Gamma_{\varphi,\mathbf{H}}(r, \theta, z)$ indicate the variation for each of the coordinates. $\mathbf{r}$ is the position vector. If we assume no wave propagation in the radial direction, so that the displacement

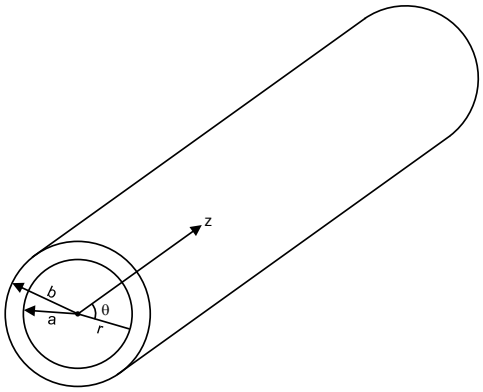

Figure 2.1: Cylindrical coordinate system, and pipe dimensions.

field varies in the axial (z) and circumferential (θ) directions only, equation 2.11 may be simplified to

$$\varphi, \mathbf{H} = \Gamma_{\varphi,\mathbf{H}}(r)\mathrm{e}^{\mathrm{i}k_\theta\theta}\mathrm{e}^{\mathrm{i}(\xi z-\omega t)}, \tag{2.12}$$

where k_θ and ξ are the wavenumber components in the circumferential and z directions, respectively.

Following the work of Gazis [40], the components of the Helmholtz decomposition, as given in equation 2.5a, becomes

$$\varphi = f(\mathbf{r})\cos(n\theta)\mathrm{e}^{\mathrm{i}(\xi z-\omega t)}, \tag{2.13a}$$
$$\mathbf{H}_r = g_r(\mathbf{r})\sin(n\theta)\mathrm{e}^{\mathrm{i}(\xi z-\omega t)}, \tag{2.13b}$$
$$\mathbf{H}_\theta = g_\theta(\mathbf{r})\cos(n\theta)\mathrm{e}^{\mathrm{i}(\xi z-\omega t)}, \tag{2.13c}$$
$$\mathbf{H}_z = g_3(\mathbf{r})\sin(n\theta)\mathrm{e}^{\mathrm{i}(\xi z-\omega t)}. \tag{2.13d}$$

The angular wavenumber, k_θ, must be an integer value in order for the solution of the equation set to be unique; i.e. the same solution is obtained at θ as at $\theta + 2\pi n$, where $n \in (1, 2, \dots)$. Inserting equations 2.13 into the Helmholtz differential equations (equations 2.7) yields three independent potential functions, $f(r)$, $g_1(r)$ and $g_3(r)$, which all satisfy the Bessel differential operator, as discussed in [40]. Pavlakovic et al. [43] provides a thorough discussion of the criteria governing the choice of arguments for the Bessel functions as a function of type of Bessel function and wave.

The displacement fields can be obtained from the Helmholtz decomposition

given in equation 2.5a after some mathematical manipulation as

$$u_r = \left[f' + \frac{n}{r}g_3 + \xi g_1\right]\cos(n\theta)\mathrm{e}^{\mathrm{i}(\xi z-\omega t)}, \tag{2.14a}$$

$$u_\theta = \left[-\frac{n}{r}f + \xi g_1 - g_3'\right]\sin(n\theta)\mathrm{e}^{\mathrm{i}(\xi z-\omega t)}, \tag{2.14b}$$

$$u_z = \left[-\xi f - g_1' + (n+1)\frac{g_1}{r}\right]\cos(n\theta)\mathrm{e}^{\mathrm{i}(\xi z-\omega t)}. \tag{2.14c}$$

In-plane stresses and strains are omitted in the following, as a pipe in vacuum is discussed, from which it follows that the displacements are no longer constrained at the pipe surfaces. Furthermore, since the cylindrical structure has no contact with any other media at the interfaces, the normal and tangential stresses must equal zero at the interfaces. The boundary conditions, where the inner and outer dimensions are indicated in figure 2.1, thus become

$$\sigma_{rr} = \sigma_{r\theta} = \sigma_{rz} = 0 \quad \text{at} \quad r = a, b. \tag{2.15}$$

Much work has likewise been done on cylinders embedded in liquid and multiple layered structures, a summary of which can be found in [43]. In practical situations pipes are likely to be coated, in addition to the presence of internal liquid or gas flow. The implications of this will be discussed in later chapters, but much can be solved by clever choice of mode and frequency range of the interrogating signal. The discussion here is limited to the case of a cylindrical pipe in vacuum, for which the appropriate boundary conditions are given in equation 2.15.

The relations between stress and strain are given by

$$\sigma_{rr} = \lambda\nabla^2\varphi + 2\mu\varepsilon_{rr}, \tag{2.16a}$$

$$\sigma_{r\theta} = 2\mu\varepsilon_{r\theta}, \tag{2.16b}$$

$$\sigma_{rz} = 2\mu\varepsilon_{rz}, \tag{2.16c}$$

while the relevant strain components are related to the displacement fields by

$$\varepsilon_{rr} = \frac{\partial u_r}{\partial r}, \tag{2.17a}$$

$$\varepsilon_{r\theta} = \frac{1}{2}\left[r\frac{\partial}{\partial r}\frac{u_\theta}{r} + \frac{1}{r}\frac{\partial u_r}{\partial \theta}\right], \tag{2.17b}$$

$$\varepsilon_{rz} = \frac{1}{2}\left[\frac{\partial u_r}{\partial z} + \frac{\partial u_z}{\partial r}\right]. \tag{2.17c}$$

By substituting the displacement fields given by equations 2.14 into 2.17, and combining the result with equations 2.16, the stresses can be found as functions

of the displacement fields as

$$\sigma_{rr} = \left[-\lambda\left(\alpha^2+\xi^2\right) f + 2\mu\left(f'' + \frac{n}{r}\left(g_3' - \frac{1}{r}g_3\right) + \xi g_1'\right)\right]\cos(n\theta), \quad (2.18a)$$

$$\sigma_{r\theta} = \mu\left[-2\frac{n}{r}\left(f' - \frac{f}{r}\right) - \left(2g_3'' - \beta^2 g_3\right) - \xi\left(\frac{n+1}{r}g_1 - g_1'\right)\right]\sin(n\theta), \quad (2.18b)$$

$$\sigma_{rz} = \left[-2\xi f' - \frac{n}{r}\left(g_1' + \frac{n+1}{r}g_1\right) + \left(\beta^2 - \xi^2\right) g_1 - \frac{n\xi}{r}g_3\right]\cos(n\theta), \quad (2.18c)$$

where $\alpha^2 = \frac{\omega^2}{c_l^2} - \xi^2$, $\beta^2 = \frac{\omega^2}{c_s^2} - \xi^2$, and ξ is the complex wavenumber in the z direction. The time-harmonic propagation factor $\mathrm{e}^{\mathrm{i}(\xi z - \omega t)}$ is omitted in equations 2.18 for brevity.

The characteristic equation of the problem that describes the entire system can then be obtained as a determinant of coefficients calculated from the insertion of the boundary conditions given in equations 2.15 into eqs. 2.18 as

$$|D|_{ij} = 0, \quad (i,j) = 1 \text{ to } 6, \quad (2.19)$$

where i and j corresponds to rows and columns, respectively. With multiple layer systems the matrix size will increase in size as a function the number of layers, as the number of boundary conditions that must be satisfied increases with increasing number of interfaces between layers present.

Some features of the different wave propagation types are readily apparent from equations 2.18; e.g. longitudinal modes ($n = 0$) have no displacement in the θ direction, while torsional modes, of which the fundamental mode is used in a major part of this thesis, have displacement of motion in the u_θ direction only. Gazis [40] found that the fundamental torsional mode is not adequately described by equations 2.14, but will with displacement fields $u_r = u_z = 0$ and $u_\theta = Ar\,\mathrm{e}^{\mathrm{i}(\xi z - \omega t)}$ satisfy the equations of motion, from which it already can be seen that this mode is completely non-dispersive.

Guided wave properties are in this thesis calculated using the commercially available software tool DISPERSE v2.0, developed at Imperial College, London, by Lowe and Pavlakovic [37, 44, 45]. DISPERSE is based on the *global matrix method*, as first proposed by Knopoff [46] and later refined by Schmidt and Jensen [47]. In the global matrix method a single matrix, $[G]$, represents the entire system, and is based on satisfying the boundary conditions at each interface. By multiplying $[G]$ by the partial wave amplitudes, $\{A\}$, all boundary conditions are applied simultaneously, thus

$$[G]\{A\} = 0. \quad (2.20)$$

If the determinant of $[G]$ is zero, equation 2.20 is satisfied. Advantages and disadvantages of the global matrix method compared with other methods are given in [37], and details on its implementation in DISPERSE explained in [43].

Modal properties

As mentioned in Section 2.2, there are potentially an infinite number of modes present in a pipe structure. In order to keep track of the various modes in a consistent way, the naming convention outlined by Silk and Bainton [48] is adopted in the discussion of guided waves in pipes throughout this thesis. They divide the modes into three types, which are categorised by their type, circumferential order (n = 0,1,2,...) and through a counter variable (m = 1,2,3,...) as

1. Longitudinal modes, L(0,m);
   axially symmetric modes with displacement fields $u_r, u_z \neq 0$ and $u_\theta = 0$.

2. Flexural modes, F(n,m);
   non-axially symmetric modes with displacement fields $u_r, u_z, u_\theta \neq 0$.

3. Torsional modes, T(0,m);
   axially symmetric modes with displacement fields $u_\theta \neq 0$ and $u_r, u_z = 0$.

Visualisation of mode shapes in a pipe is not straightforward, and requires some experience and thought. With respect to mode order, zero order modes exhibit no variation around the circumference of pipe and are the only ones that exist at zero frequency. Higher order modes exhibit increased complexity around the pipe circumference; i.e. the first order modes will be 180° out of phase on the top of the pipe compared with the bottom. Thus, the order of mode vibration can be said to address the flexing of the pipe as a whole.

On the other hand, the counter variable, m, reflects the vibration within the pipe wall thickness; higher values of m means increased complexity of the vibration through the thickness of the pipe. The variation of displacement, stress or energy through the thickness of the pipe wall is called the mode shape, and is frequency dependent. Mode shapes are essential in the understanding of guided wave propagation, reflection and refraction, and can be calculated using DISPERSE, and show the relative amplitudes of the displacement (or stress, energy etc.) components through the pipe wall thickness.

Figure 2.2 shows example displacement mode shapes at 60 kHz for a 3 in. schedule 40 pipe in vacuum, where (a) through (d) shows the mode shape of the T(0,1), F(1,2), F(1,3) and F(2,2) modes, respectively. As discussed above, each mode has three possible displacement directions: radial (r), tangential (θ) and longitudinal (z), which are indicated by relative displacement amplitudes through the pipe wall thickness in figure 2.2. The T(0,1) mode has nonzero displacement component in the tangential direction only, while the other modes shown exhibit longitudinal and radial displacement to a certain extent as well. At boundaries or discontinuities in a given pipe, reflection, transmission and refraction of the incident propagating modes may happen depending on the geometry of the discontinuity. Other modes than the incident mode may be excited at the boundary of the discontinuity through mode conversion [49].

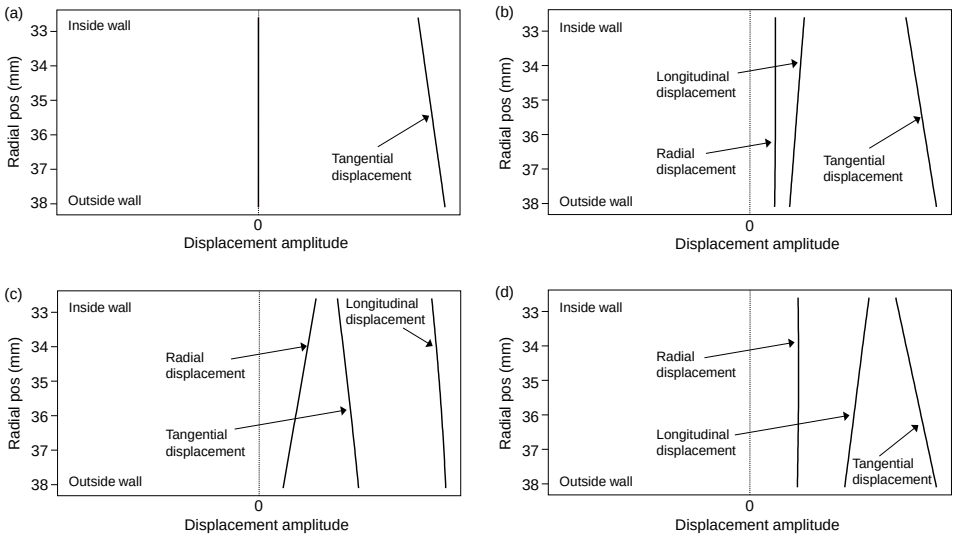

Figure 2.2: Displacement mode shapes for modes (a) T(0,1), (b) F(1,2), (c) F(1,3) and (d) F(2,2) at 60 kHz in a 3 in. schedule 40 pipe.

Practical non-destructive testing (NDT) and evaluation (NDE) is limited to lower order modes. There are several reasons for this, most importantly that the user in practice will be limited in resolution, so that higher order modes cannot be clearly separated. The solutions to the characteristic equations of the propagation in a given structure, as defined in equation 2.19, give the dispersion curves of the system, which are the properties of the guided wave propagation. Dispersion curves describe the phase (c_{ph}) or group velocity (c_{gr}), attenuation or mode shapes as a function of frequency or the frequency-thickness product of the structure, and are essential for the understanding and execution of guided wave testing. Wilcox et al. discusses the effects of mode and frequency optimisation for defect sizing in pipes in [50].

The phase velocity describes the velocity of the phase of the single frequency components within a given wave packet, that is

$$c_{\mathrm{ph}} = f\lambda = \frac{\omega}{k}, \tag{2.21}$$

where k is the wavenumber, while the group velocity is the velocity that the entire wave packet travel with at a given frequency, and can be calculated from the phase velocity by taking its derivative

$$c_{\mathrm{gr}} = c_{\mathrm{ph}} + k\frac{dc_{\mathrm{ph}}}{dk}. \tag{2.22}$$

The phase velocity approaches infinity as the group velocity approaches zero, which happens for all modes except the fundamental ones. Further dis-

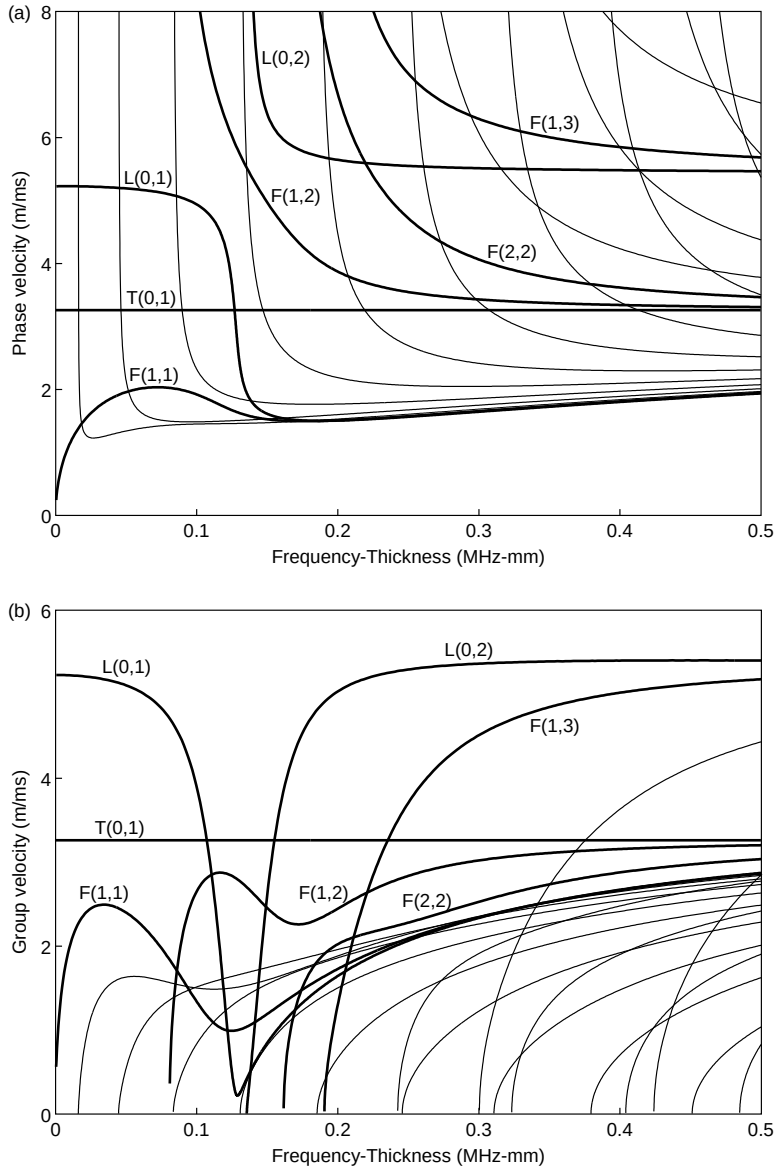

Figure 2.3: Phase (a) and group (b) velocity dispersion curves for a 3 in. schedule 40 (76.2 mm outer diameter, 5.5 mm wall thickness) pipe in vacuum.

cussion on properties and alternate forms to express the phase and group velocities can be found in e.g. [8]. Attenuation is not discussed here as a steel pipe in vacuum will be used throughout this thesis, which results in negligible attenuation for guided wave propagation.

Figure 2.3 (a) and (b) show the phase and group velocity dispersion curves for the same 3 in. schedule 40 pipe (outer diameter 76.2 mm, wall thickness 5.5 mm) as discussed above, where the most commonly used modes are indicated in bold. Recently, the fundamental torsional mode, T(0,1) is the most frequently used mode for guided wave testing in pipes [11, 12, 15, 17, 19, 20, 25, 33, 51], but both the L(0,1) and L(0,2) have also been investigated extensively [7, 14, 16, 18, 21, 49, 52, 53]. The T(0,1) mode can be seen to be nondispersive at all frequencies, while the L(0,1) and L(0,2) modes are essentially nondispersive within some frequency ranges and highly dispersive at other frequencies.

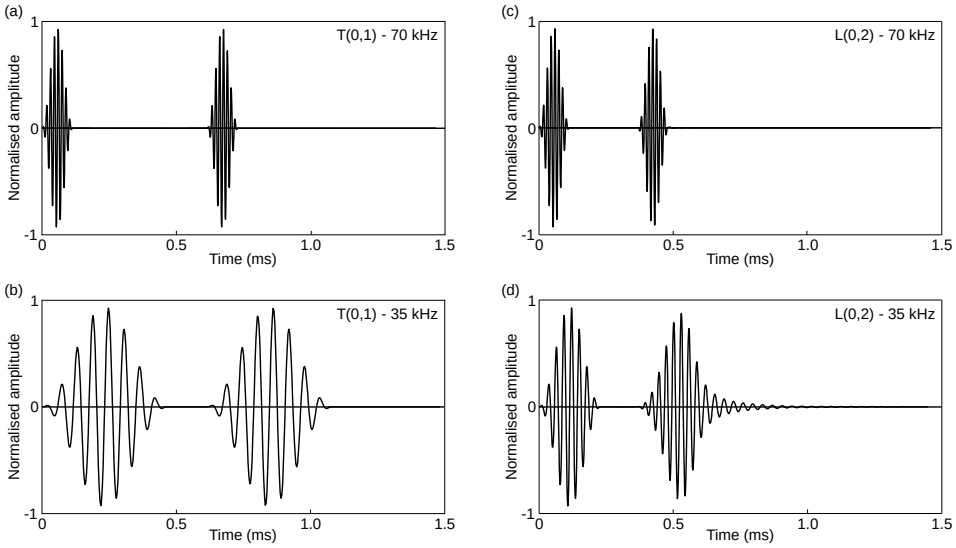

Figure 2.4: Examples of the effect of dispersion in a 3 in. schedule 40 pipe. An 8 cycle Hanning windowed toneburst is showed after 0 and 2 m propagation. (a) and (b) show the T(0,1) mode with centre frequency of 70 and 35 kHz, while (c) and (d) shows the L(0,2) mode at the same centre frequencies.

The practical consequences of dispersive behaviour of the propagating modes are that they spread in time and space as they propagate along the length of a pipeline. If an ultrasonic guided wave packet is dispersive, its duration increases linearly with propagation distance [50]. Figure 2.4 shows examples calculated using DISPERSE, where an 8 cycle Hanning windowed toneburst with centre frequencies of 35 and 70 kHz for the T(0,1) and L(0,2) modes are shown after 0 and 2 m of propagation, as indicated in the figure. With a wall thickness of 5.5

mm, these frequencies correspond to approximately 0.19 and 0.38 MHz-mm in figure 2.3 (b). As the T(0,1) mode is nondispersive at all frequencies, no change in the shape of the propagating shape can be seen in either cases shown in (a) and (b), as expected. With the given pipe dimensions, the L(0,2) mode is highly dispersive from around 40 kHz towards its cut-off at approximately 20 kHz, and essentially nondispersive at higher frequencies. At 70 kHz, the shape of L(0,2) wave packet is comparable with its shape upon excitation, which indicates nondispersive propagation. Comparing the propagation of T(0,1) and L(0,2) with a centre frequency of 70 kHz, as shown in figure 2.4 (a) and (c), it is evident that the L(0,2) propagates faster than the T(0,1) mode, as expected from the dispersion curves in figure 2.3. With a centre frequency for the L(0,2) mode of 35 kHz, as shown in figure 2.4 (d), it is in its dispersive region, and the wave packet will be increasingly distorted with propagation distance. Since dispersion is a physical phenomenon it cannot be avoided as such, but with wise choice of mode and frequency range in practical testing, its influence can be limited and controlled [50]. However, dispersion compensation techniques have also been developed, as reported in [54, 55].

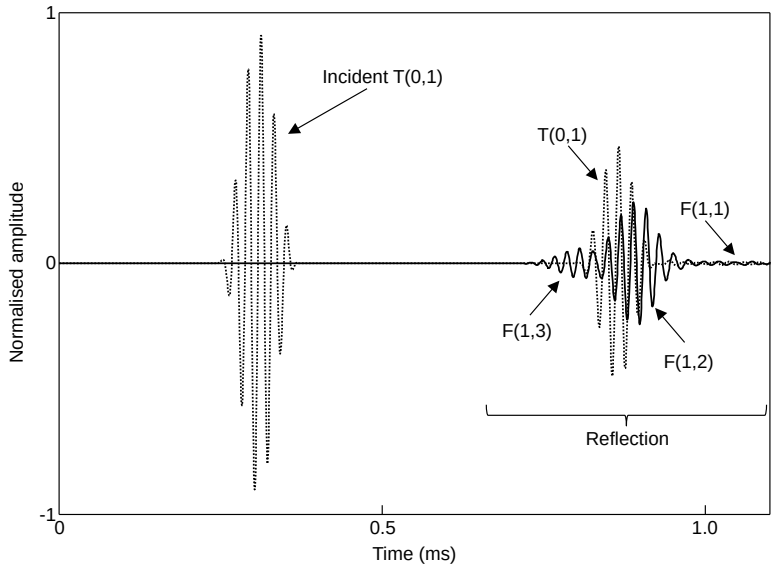

Figure 2.5: Example time trace and mode conversion, where the T(0,1) and F(1,m) modes are shown by the dotted and solid lines, respectively.

The main goal of NDT is to detect, and possibly size, weaknesses in a structure before they lead to leaks, ruptures or fatigue. When a guided wave signal propagates along a pipe, changes in the geometry will lead to reflections of different modes depending on the size, shape and location of the discontinuity,

and properties of the incident wave. Figure 2.5 shows a typical time trace from the same 3 in. schedule 40 pipe discussed above, where the T(0,1) mode is incident on a circumferential through-thickness crack of length 50% of the pipe circumference. The T(0,1) mode is shown by the dotted line, while the mode converted F(1,m) modes are shown by the solid line. For defects or other discontinuities that are non-axisymmetric, which is the case here, mode conversion into both axisymmetric and non-axisymmetric modes can occur, in addition to the reflection of the incident mode. The mode shapes of the each mode existing within the bandwidth of the interrogating signal govern the extent of mode conversion. The higher the similarities in particle motion between the modes, the stronger the mode conversion. Only the first order modes are extracted in figure 2.5, but also higher order modes could be investigated.

The method described by Lowe et al. [49] is adopted in order to extract higher order modes throughout this thesis. As the T(0,1) mode only has a tangential displacement for all frequencies, the extent to which other modes are generated through mode conversion from T(0,1) is governed by the extent of tangential motion in the other modes. The F(1,2) has a dominant tangential displacement within the frequency range used in this example, so the mode conversion to the F(1,2) mode can be seen to be relatively strong. F(1,3) on the other hand, has dominant longitudinal displacement, and consequently appear with lower reflected amplitude. Note also that no higher order modes can be extracted from the incident wave, as the excitation is symmetric. Similarly, symmetric features such as welds will not generate reflections of significant amplitude for nonaxisymmetric modes: reflections from welds or symmetric pipe joints can thus be distinguished from other defects by evaluating the amplitude of the reflected higher order modes relative to the corresponding T(0,1) reflection.

2.3 Guided waves in plates

The simplest case of guided wave propagation is the case of a plate of thickness t, infinite extent in the $x - z$ plane, and traction free boundaries on both sides, as shown in figure 2.6, where the particle velocity and traction force must be continuous on the boundaries. Guided wave propagation in plates are governed by the equations of motion given in equations 2.7. In general, two types of guided waves may propagate in a plate: compressional or shear waves. Lamb waves were first investigated by H. Lamb in 1917 [56], and are waves of plane strain, with particle displacements entirely in the $y - z$ plane. They include compressional (P) and vertically polarised shear (SV) waves, which can be either symmetric or anti-symmetric with respect to the mid-plane of the plate thickness.

The Rayleigh-Lamb frequency equations may be obtained from the governing equations of motion and boundary conditions through some mathematical manipulation, which is detailed in e.g. Rose [8] and Achenbach et al. [57].

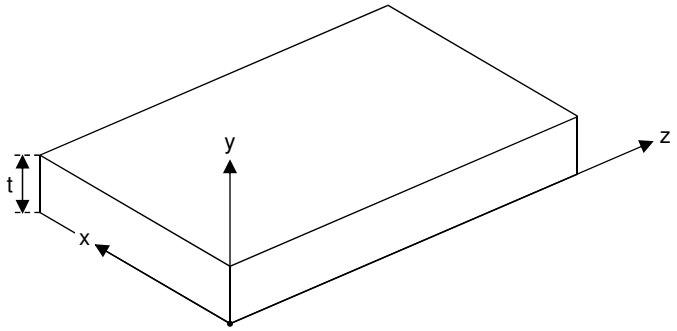

Figure 2.6: Schematic of free plate.

With reference to the coordinate system in figure 2.6, the symmetric and anti-symmetric wavenumbers, k_n, are given by the roots of

$$\frac{\tan\left(q\frac{t}{2}\right)}{\tan\left(p\frac{t}{2}\right)} = -\frac{4k_n^2pq}{\left(q^2-k_n^2\right)^2}, \tag{2.23a}$$

$$\frac{\tan\left(q\frac{t}{2}\right)}{\tan\left(p\frac{t}{2}\right)} = -\frac{\left(q^2-k_n^2\right)^2}{4k_n^2pq}, \tag{2.23b}$$

respectively, where

$$p = \sqrt{\left(\frac{\omega}{c_\mathrm{l}}\right)^2 - k_n^2}, \tag{2.24a}$$

$$q = \sqrt{\left(\frac{\omega}{c_\mathrm{s}}\right)^2 - k_n^2}, \tag{2.24b}$$

and c_l and c_s denote the longitudinal and shear wave velocity, respectively. These roots are obtained by choosing a real-valued frequency ω and then calculating the infinite number of corresponding values of k_n [58]. This can only be done numerically, and result in the dispersion curves of the waveguide. The resulting symmetric and anti-symmetric modes are commonly labelled S_n and A_n, where n is a counter variable.

Additionally, horizontally polarised shear (SH) waves may be present in the plate, which arise when the scalar potential of equation 2.9a vanishes, that is $u_y = u_z = 0$, with respect to figure 2.6. The wavenumbers of the SH waves can then be found by assuming a solution to equation 2.9b in the form

$$\mathbf{H} = \mathbf{H}_x \mathrm{e}^{\mathrm{i}(k_z z - \omega t)}, \tag{2.25}$$

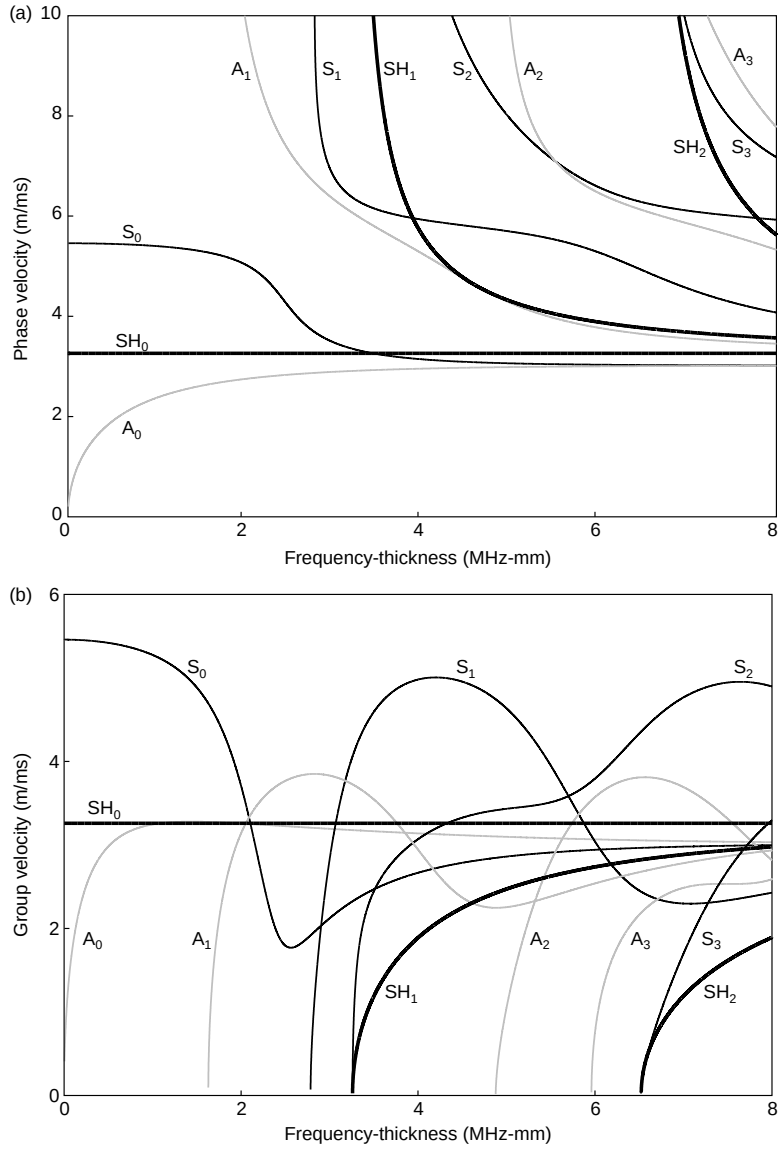

Figure 2.7: Dispersion curves for a 3 mm thick steel plate, where (a) shows the phase velocity and (b) the group velocity as a function of the frequency-thickness product.

which by following the derivation given in e.g. [35] leads the following expression for the wavenumber k_z

$$k_z = \sqrt{\left(\frac{\omega}{c_\mathrm{s}}\right)^2 - \left(\frac{n\pi}{t}\right)^2}, \tag{2.26}$$

where n is a counter variable. The dispersion curves for the SH waves can be derived from equation 2.26, which is considerably simpler mathematically than the corresponding solutions for the Lamb waves discussed above.

Figure 2.7 shows the phase and group velocities for a 3 mm thick steel plate as a function of the frequency-thickness product, where the S_n, A_n and SH_n modes are shown in black, grey and bold black lines, respectively. Only the 0^{th} order modes exist towards zero frequency, as all other modes have a cut-off frequency below which they do not propagate. The SH_0 mode can be seen to be the only mode that is nondispersive at all frequencies. The cut-off frequencies of the SH modes can be calculated by expressing equation 2.26 in terms of the phase velocity by substituting ω/c_ph for k_z which gives

$$c_\mathrm{ph} = \frac{\omega}{\sqrt{\left(\frac{\omega}{c_\mathrm{s}}\right)^2 - \left(\frac{n\pi}{t}\right)^2}}, \tag{2.27}$$

and by subsequently setting the denominator to zero, the relation

$$ft = \frac{nc_\mathrm{s}}{2}, \tag{2.28}$$

is obtained, from which the cut-off frequencies seen in figure 2.7 (a) can be calculated. The group velocity curves can be obtained by differentiation of equation 2.27 with respect to the wavenumber k_z, from which the same cut-off frequencies can be calculated, as seen from figure 2.7.

In the case of a stress-free infinite plate, SH waves will only produce reflected or refracted SH waves upon interaction with the plate boundaries, while P and SV waves are mutually coupled as they propagate along the plate, and may reflect partly into the other at the plate boundaries [35]. So in the latter case, longitudinal and shear motion interact as they have displacement components in the same plane.

2.4 Relationships between guided waves in plates and pipes

FE analysis of simple scattering problems in plates will be compared with their corresponding analytical solutions in order to validate the FE models in subsequent chapters. Similarly will the analytical solution of a single through-thickness circular hole in a plate be used to validate the corresponding guided

wave scattering problem in pipes. In order to do so, relationships and properties between guided waves in plates and pipes are employed, as outlined below following the analysis presented by Velichko et al. [27].

Longitudinal and flexural modes in pipes behave similarly to Lamb modes in plates, in that they consist of longitudinal (P) and shear vertical (SV) motion, while the torsional modes find their equivalents in the SH modes in a plate [35, 59]; i.e. the SH_0 mode corresponds to the T(0,1) mode, the L(0,2) mode corresponds to the S_0 mode from around 0.2 MHz-mm (for a 3 in. schedule 40 pipe) to the L(0,3) cut-on frequency-thickness value; while the L(0,1) mode corresponds to the S_0 mode at low frequency-thickness and to the A_0 mode from around 0.2 MHz-mm upwards. Modes in pipes become increasingly similar to the ones in plates with increasing pipe diameter. As the prediction of guided wave behaviour in pipes often is a complex three-dimensional problem, it can in general only be solved using numerical methods.

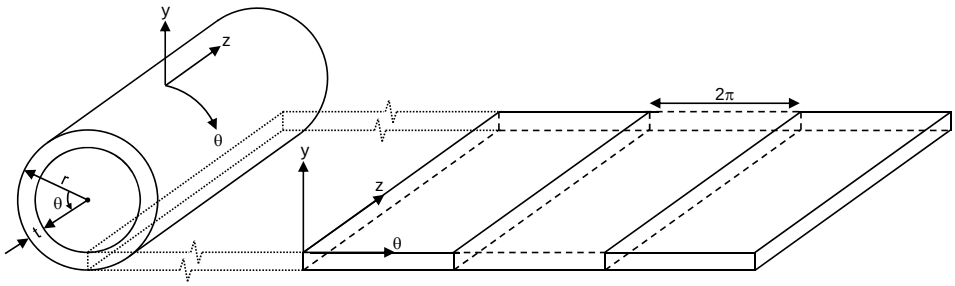

Figure 2.8: Relationship between the plate and pipe geometries.

Figure 2.8 shows a hollow cylinder and corresponding unrolled plate with their cylindrical coordinates (θ, y, z) indicated on both pipe and plate. The physical solution for the pipe must be periodic in the θ direction with a period of 2π so that the displacement fields in the pipe can be written as a superposition of displacements in the unbounded structure (as shown for the plate in figure 2.8) in the θ direction as

$$\mathbf{u}_{\text{tot}}(\theta, y, z) = \sum_{n=-\infty}^{+\infty} \mathbf{u}_{\text{unb}}(\theta + 2\pi n, y, z), \tag{2.29}$$

where $\mathbf{u}_{\text{unb}}$ is the solution to the guided wave excitation in an unbounded structure, and n is an integer.

In cases where the radius of the pipe is much larger than the pipe wall thickness and the wavelengths of the propagating modes are much shorter than

the pipe circumference, that is

$$r \gg t, \tag{2.30a}$$

$$2\pi r \gg \lambda, \tag{2.30b}$$

the pipe can be approximated as an unrolled plate [27, 60], as the influence of the curvature of the pipe becomes negligibly small as a consequence of satisfying equations 2.30. Velichko et al. [27] gives a detailed mathematical derivation of the relationships between guided wave modes in plates and pipes, as well as quantitative estimates of the approximation errors accepted. The latter shows that the error increases with larger circumferential mode orders, as these modes to a larger extent are affected by the pipe curvature, and that the error becomes roughly ten times smaller when the radius of the pipe is set to the middle of the pipe wall thickness compared with the outer radius. Furthermore, provided that equations 2.30 are satisfied, guided wave scattering from defects in plates are related to scattered circumferential modal amplitudes from the corresponding defects in pipes by

$$S_{\text{pipe}} = \frac{\sqrt{\lambda}\mathrm{e}^{\mathrm{i}\frac{\pi}{4}}}{2\pi r} S_{\text{plate}}, \tag{2.31}$$

where the scattering matrix of the defect in a plate, S_{plate}, is a function of the incident and scattering angles of the guided wave.

2.5 Finite element (FE) modelling of guided wave propagation

The scattering of both bulk and guided waves from defects is often divided into three regimes using the parameter ka, where k is the wavenumber and a is the characteristic dimension of the defect [61]. At low frequencies, where the wavelengths of the interrogating signal are long compared with defect dimensions, both the Born [62–65] and the quasistatic [66, 67] approximations are analytic methods that have been employed with success. A rule of thumb of their validity is that $ka < 0.1$. High frequency approximations include the Kirchhoff approximation [68, 69] and geometrical diffraction theory [70], and are commonly considered when $ka > 1$. For an excellent review of different approximations and analytical approaches, see Rajagopal [71], while Schmerr et al. [72] give a good review and comparison of model based methods in defect sizing.

In the intermediate regime, when the dimensions of the scatterers are comparable to the incident wavelength and/or the scatterers are of complex shape, numerical methods such as finite elements (FE), boundary elements (BE) or finite difference (FD) are appealing. The work in this thesis relies heavily on FE modelling, which is mainly done in ABAQUS/Explicit v6.7 [73] and 6.9 [74], although some early work was done using COMSOL Multiphysics v3.5a [75]. Both these programs are commercially available.

The basic approach of any numerical method is to discretise the governing equations, which in this case are equations 2.7, and solve them in discrete, incremental steps. The equations of motion for a given structure may be written in matrix form as

$$\mathbf{M}\ddot{\mathbf{u}} + \mathbf{C}\dot{\mathbf{u}} + \mathbf{K}\mathbf{u} = \mathbf{F}_{\text{ext}}, \tag{2.32}$$

where $\mathbf{M}$, $\mathbf{C}$ and $\mathbf{K}$ are the mass, damping and stiffness matrices, and $\ddot{\mathbf{u}}$, $\dot{\mathbf{u}}$ and $\mathbf{u}$ are acceleration, velocity and displacement vectors, respectively. $\mathbf{F}_{\text{ext}}$ are the external forces. Damping will not be studied in this work, as wave propagation in steel plates and pipes in vacuum is considered, where the damping is negligible. However, absorbing layers with increasing damping (ALID) will be used as absorbing boundaries around the steel plates investigated in Chapter 3. ALIDs consist of several sublayers all with the same material parameters as the main plate, only with with gradually increasing damping. In FE packages such as ABAQUS, stiffness of mass proportional damping is generally termed Rayleigh damping, and may be defined as [76]

$$\mathbf{C} = c_{\text{M}}\mathbf{M} + c_{\text{K}}\mathbf{K}, \tag{2.33}$$

where c_{M} and c_{K} are the mass and stiffness proportional damping coefficients, respectively. It is preferable to avoid using c_{K} in ALIDs when employing explicit time stepping, as it leads to low computational efficiency, so following Drozdz [76], ALIDs are calculated as

$$c_{\text{M}}\left(l_{\text{abs}}\right) = c_{\text{M}_{\text{max}}}\left(\frac{l_{\text{abs}}}{L_{\text{abs}}}\right)^{p} \quad \text{and} \quad c_{\text{K}}(l_{\text{abs}}) = 0, \tag{2.34}$$

where the sublayers $l_{\text{abs}} \in (1, 2, 3, ..., L_{\text{abs}})$ and L_{abs} is the total number of sublayers. As space is discretised in the FE models, ALIDs consist of a series of sublayers with increasing c_{M}. To minimize the change in impedance between each sublayer, it is recommended to limit them to one element in thickness each [76].

Wave propagation is commonly introduced in the system by applying forces or prescribed displacement constraints to a selection of nodes, bringing it out of its initial equilibrium state. With explicit dynamics in ABAQUS, a large number of small time increments are calculated in an inexpensive manner, as an explicit central-difference time integration rule is employed. In employing the explicit central-difference integration rule, the equations of motion for the structure are given by

$$\dot{u}^{N}_{i+\frac{1}{2}} = \dot{u}^{N}_{i-\frac{1}{2}} + \frac{\Delta t_{i+1} + \Delta t_i}{2}\ddot{u}^{N}_{i}, \tag{2.35a}$$

$$u^{N}_{i+1} = u^{N}_{i} + \Delta t_{i+1}\dot{u}^{N}_{i+\frac{1}{2}}, \tag{2.35b}$$

where u^{N}_{i} is a degree of freedom of displacement or rotation, Δt is the time increment, and i refers to the increment number in the calculation [74]. The

wave propagation in the structure is thus advanced by using values for the acceleration, velocity and displacement from the previous increment. The computational efficiency in employing the central-difference time integration rule has its basis in employing diagonal mass matrices, as the accelerations for each increment are calculated as product of the mass matrix $\mathbf{M}^{NJ}$ and difference between the applied load vector, $\mathbf{F}^J$, and the internal force vector, $\mathbf{I}^J$; that is

$$\ddot{u}_i^N = \left(\mathbf{M}^{N,J}\right)^{-1} \left(\mathbf{F}_i^J - \mathbf{I}_i^J\right). \tag{2.36}$$

Additionally, no global mass or stiffness matrices need to be formed (and thus not inverted), which further contributes to make the method less computationally expensive.

As the explicit procedure integrates through time by using many small time increments, the spatial and temporal resolutions must be adequately fine for the FE models to converge properly. The time increment approximated by ABAQUS to ensure convergence is given in [74] as

$$\Delta t \approx \frac{L_{\min}}{c_d\sqrt{D}}, \tag{2.37}$$

where $L_{\min}$ is the smallest nodal distance in the mesh, c_d is the dilatational wave speed and D is the dimensional order of the model. Other requirements are reported in the literature, e.g. Moser et al. [77] reported

$$\Delta t = \frac{1}{20 f_{\max}}, \tag{2.38}$$

which in some cases needed to be refined 6 times depending on the type of input signal employed.

When it comes to the spatial resolution, the mesh size must be chosen so that the propagating waves are properly resolved, and that all geometrical properties of the models are modelled sufficiently accurate. Alleyne et al. [78] recommended a shortest nodal separation ensuring more than 10 nodes per wavelength for the uniform square mesh they employed, while Moser et al. [77] gave a requirement of 20 nodes per shortest wavelength, that is

$$l_e = \frac{\lambda_{\min}}{20}, \tag{2.39}$$

where l_e is the element length and $\lambda_{\min}$ is the shortest wavelength of interest.

The most extensive work known to the author on this matter is the work by Drozdz [76], which evaluated the influence of mesh parameters on elastic bulk wave velocities, assessing both the temporal and spatial requirements for FE models to converge properly for a variety of element types. Depending on the angle of propagation and mesh type, the mesh refinement varied greatly, in some situations requiring up to 30 elements per shortest wavelength. The

work of Drozdz [76] is the basis of choice of mesh size and time increments throughout this thesis. He also assessed the mesh refinement needed to model small defects sufficiently accurate, which also is of great relevance for the work presented here.

Despite the results and recommendations available in the literature, convergence tests are run for each model type used throughout this thesis, with the results of Drozdz as a starting point of evaluation.

Chapter 3

The reflection and scattering from defects in plates

This chapter opens with a short introduction to previous work on defect detection and characterisation in plates in Section 3.1. Section 3.2 discusses the reflection of the S_0, A_0 and SH_0 modes from axisymmetric notches, similarly as in earlier work reported by Lowe et al. [28, 29] and Demma et al. [30], especially assessing the influence of the different modal properties of the three modes. Then the reflection and scattering from a through-thickness circular hole is presented in Section 3.3. Initially, the work of Diligent et al. [31] with plane S_0 wave incidence is followed in detail, in order to validate the FE model and post processing methods, while the scattering as a function of angle is evaluated against an analytical implementation done by Cegla et al. [32]. The following subsection similarly investigates the reflection and scattering of a through-thickness circular hole in a plate with plane SH_0 wave incidence, both as a function of distance from the hole, and angular scattering direction. An extensive evaluation and validation of the scattering patterns against the same analytical implementation [32] is presented. Hole diameters ranging from 3.75 mm to 144 mm are investigated, where the smaller range include defects sizes seen in pitting corrosion, as will be thoroughly assessed in later chapters, while the larger holes are included for comparison and validation with results available in the literature. Lastly, conclusions are drawn in Section 3.4.

3.1 Introduction

The motivation behind the work presented in this chapter is to introduce and understand the reflection and scattering from simple defects in plates, which is considerably simpler than the corresponding solutions in pipes. There are many structures that are entirely flat or have significant plane sections, such as storage tanks in ships, pressure vessels, and instalments in nuclear power plants, so work on plates has significant practical use and value on its own.

Conventional inspection of such large areas is done by testing at very limited areas in the vicinity of the transducers, commonly in combination with visual inspection. This process is very time consuming if the structure to be tested is of a certain size. The introduction of ultrasonic guided wave testing enables the user to scan larger areas rapidly on the expense of resolution, compared with ultrasonic thickness gauging at specific locations. However, guided wave testing imposes several complications in their use, which result in difficulties in their interpretation. These include the presence of multiple modes propagating simultaneously in the wave guide if care is not taken in their excitation (in some situations this cannot be avoided), possible mode conversion as the incident wave interacts with either plate boundaries or defects, in addition to modes potentially being dispersive.

The basic properties of guided waves in plates are outlined in Section 2.3. Many authors have contributed to the understanding of the reflection and scattering from guided waves from single defects in plates [22, 24, 26, 28–32, 79–87]. As the most important parameter in practical test situations usually is the maximum defect depth, much focus has been given to the estimation of this parameter. However, as defects occur in a large variety of shapes and sizes, the effects of other parameters describing them on the reflection and scattering of the incident wave are of paramount importance in the understanding of the relationship between maximum defect depth and reflection coefficient (RC). Parametric studies assessing the variation in RC as a function of the width, length, orientation and shape of a defect are essential in order to understand the scattering behaviour of defects seen in practice.

In cases with through-thickness or infinite length defects, a plane strain assumption can be made in order to simplify the geometry to be simulated and make the model less computationally expensive, as done in [28–31, 79–83]. This assumption is valid when the size of the defect (and plate) in the given direction is large compared with the width of the incident wave. With plane strain, the full plate model is simplified to a cross section of the plate, which represents infinite extension in the direction normal to the plate. In cases where the size of the defect(s) is finite in all dimensions, plane stress must be employed [22, 24, 26, 32, 84–87]. Recently, as the computational power of computers become increasingly powerful, complex geometries have been investigated using full 3D models, which also will be employed in the larger part of this thesis.

3.2 The reflection from an infinitely long rectangular notch in a plate

The physical understanding of the reflection from defects of simple shape is of fundamental importance for interpretation of more complex three-dimensional defects in structures. This section discusses the reflection from a rectangular notch in a plate employing two-dimensional FE models in a plane strain domain;

analyses are carried out in turn for the S_0, A_0 and SH_0 modes. Such an approach approximates the extent of the notch to be infinite in the omitted dimension. Especially the influence of the mode shapes on the reflection from defects, in this case a rectangular notch, will be illustrated, which is important in order to understand the reflection and mode conversion behaviour of guided wave propagation and testing.

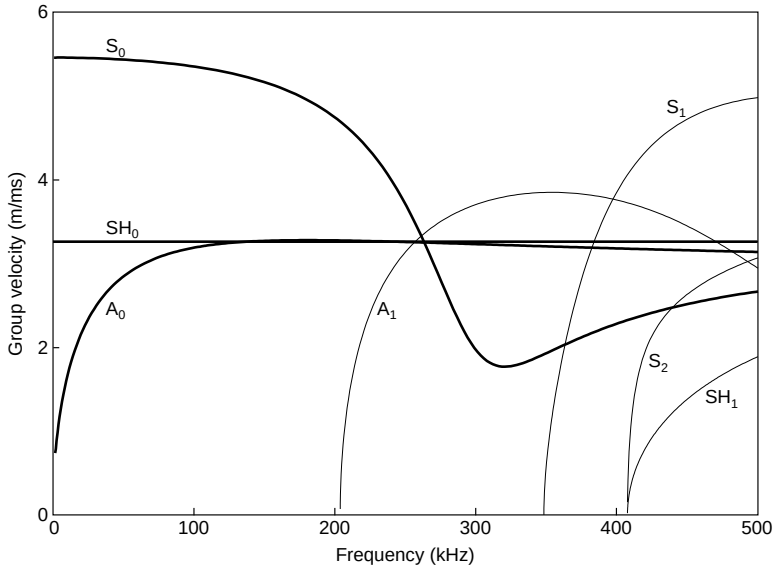

Figure 3.1: Group velocity dispersion curves for a steel plate of 10 mm thickness.

A steel plate of 10 mm thickness and length 1.5 m was modelled using plane strain in ABAQUS/Explicit v6.7 [73]. The steel plate investigated throughout Section 3.2 have a mass density, ρ, of 7932 kg/m^3, a Young's modulus, E, of 216 GPa, and a Poisson's ratio, ν, of 0.2865. The discussion in this section will be limited to the reflection from a notch of width 5 mm (half of the plate thickness) at the single frequency of 50 kHz (0.5 MHz-mm). As is evident from the group velocity dispersion curves shown in figure 3.1, only the S_0, A_0 and SH_0 modes exist at this frequency (shown in bold).

Figure 3.2 shows the FE model used to model the steel plate. In the Cartesian coordinate system used, the x, y and z directions denote the normal to the plane strain, the normal to the surface of the plate, and the direction of propagation of the excited wave, respectively. The 1.5 m long steel plate was modelled with 0,25 m absorbing regions at both ends to ensure no unwanted reflections from the plate ends. The absorbing regions consist of a number of absorbing layers with increasing damping (ALID), and are included in the

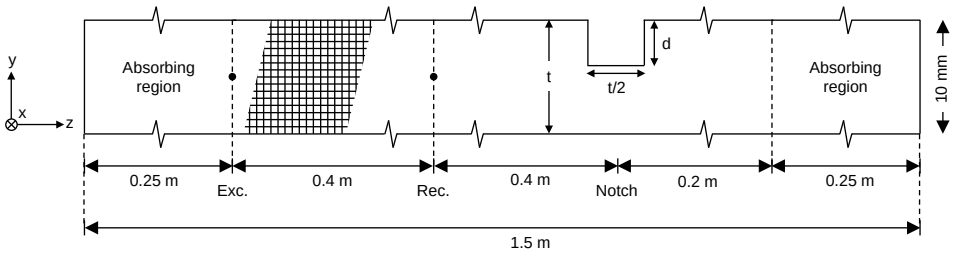

Figure 3.2: Schematic of two-dimensional plane strain FE model.

model based on the findings of Drozdz [76, 88, 89]. The absorbing regions need to be around 3-5 times the longest wavelength of the excitation signal to achieve 60 dB damping. Drozdz discusses modelling of absorbing layers by employing both perfectly matched layers (PML) and ALIDs; the author investigated an implementation of PML in the time domain [90] in Comsol Multiphysics v. 3.5a [75], achieving roughly 40 dB damping. However, the work of Drozdz [76, 88, 89] is employed throughout this thesis. With reference to equation 2.34, $c_{\mathrm{M}_{\max}}$ is set to $1e6$, and p to 3 resulting ALIDs with cubically increasing damping, which is employed throughout this chapter.

All models in this section are excited with a 5 cycle Hanning windowed toneburst with a 50 kHz centre frequency, giving a $\pm$ 15 dB bandwidth of 35–65 kHz. Within this bandwidth the S_0 mode is the fastest propagating mode, consequently having the longest wavelength, which makes it the most critical mode with respect to the required size of the absorbing regions. With absorbing boundary layers of 0.25 m, they are around 2.3 times the wavelength of the S_0 mode at 50 kHz, which was considered acceptable in this case. For the A_0 and SH_0 modes, which both have shorter wavelengths than the S_0 at all frequencies within the excitation bandwidth, the length of the absorbing layers were roughly 4 times their wavelength at 50 kHz.

Square elements of size 0.5 mm were used, resulting in 20 elements through the thickness of the plate. This complies with the requirements for number of elements per shortest wavelength [76, 78], as discussed in Section 2.5, with significantly more than 20 elements per shortest wavelength for all the three modes present. A time step of 50 ns was used in the S_0 and A_0 calculations, while 100 ns was used in the SH_0 calculations.

The excitation was applied 0.25 m from the left hand end of the plate, just outside the left hand absorbing region, as indicated in figure 3.2. Details of the excitation of the different modes will be explained in the respective subsections below. The centre of the notch was placed at 0.8 m from the excitation point, while the receiver point was centred between the excitation and the centre of the notch, at 0.4 m from both. These distances were selected so that sufficient separation between the incident and reflection signals was achieved.

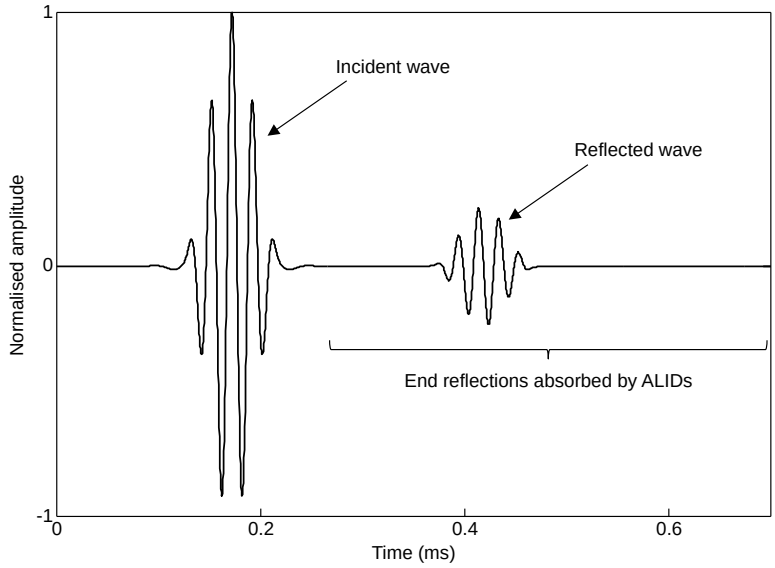

Figure 3.3: Typical time record obtained at the monitoring point 0.4 m from the excitation.

Figure 3.3 shows a typical time record obtained at the receiver node indicated in figure 3.2. The efficiency of the ALIDs is clear, as no unwanted reflections from the pipe ends are visible in the signal. RCs were calculated in the frequency domain as the ratio between the relevant displacement components of the reflected wave to that of the incident wave.

The reflection of the S_0 mode

The S_0 mode is easiest to use at low frequencies, where it is essentially non-dispersive, as can be seen from figure 3.1. Figure 3.4 shows the displacement (u) and stress (σ) mode shapes of the S_0 mode at 0.5 MHz-mm in (a) and (b), respectively. The secondary axis indicates the through-wall position, where t is the thickness of the plate.

The dominant displacement component can be seen to be u_z, which is relatively constant through the plate thickness. There is also a minor component in the direction normal to the plate surface (u_y). Towards lower frequencies the u_z component becomes completely uniform through the plate thickness, while its amplitude gets lower towards the plate boundaries for higher frequencies. The opposite happens with u_y, as it approaches zero towards zero frequency, while the displacement amplitude increases towards the plate boundaries for higher frequency, but is always zero at the middle of the plate. The stress components behave in a similar way, except that σ_{yy} has a parabolic shape, always being

zero at the plate boundaries and with increasing amplitude towards the middle of the plate with increasing frequency. That σ_{zz} is uniform throughout the plate thickness means that it has equal sensitivity to detect defects or discontinuities regardless of their position through the wall, which is a highly desirable property from a practical testing point of view. Also, as stated by Diligent et al. [31], the relatively modest amplitude of the u_y component towards the plate boundaries results in minimal leakage from the plate if it was to be immersed in an inviscid or low viscosity fluid.

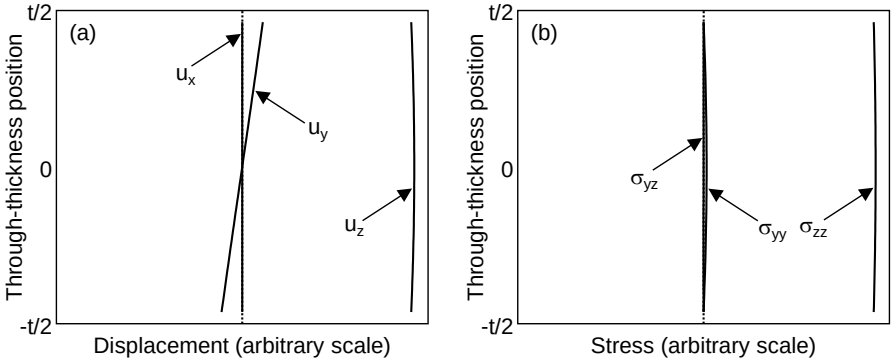

Figure 3.4: Displacement (a) and stress (b) mode shapes for the S_0 mode at 0.5 MHz-mm.

The S_0 mode was excited by applying the excitation toneburst a force in the z direction at the node at the centre of the plate thickness. Figure 3.5 shows the reflection coefficient of the S_0 mode at 50 kHz calculated at the monitoring node 0.4 m from the excitation, at the centre of the plate, as indicated in figure 3.2. The RCs were calculated as the ratio between the u_z component of the reflected wave to the one of the incident wave. At this frequency the wavelength is significantly longer than the dimensions of the notch. The depth of the notch is incremented in steps of 10% of the plate thickness. As expected from the S_0 mode shape, the reflection is roughly a linear function of notch depth at this frequency. A slightly lower increase in RC at the shallow (0-20%) and towards through-thickness (80-100%), which agrees well with the slightly lower stress amplitude of σ_{zz} at these thickness intervals.

The results in figure 3.5 are in accordance with results obtained using S_0 mode for cracks and notches by other authors [31, 83]. However, only two values from [31] are included in figure 3.5 for direct comparison, as most of the work was done on cracks at somewhat higher frequency-thickness products. The results shown are calculated from results obtained with cracks, then scaled to account for the notch width using the frequency-thickness product closest to 0.5 MHz-mm, as is employed in the FE analyses here. Still, excellent agreement

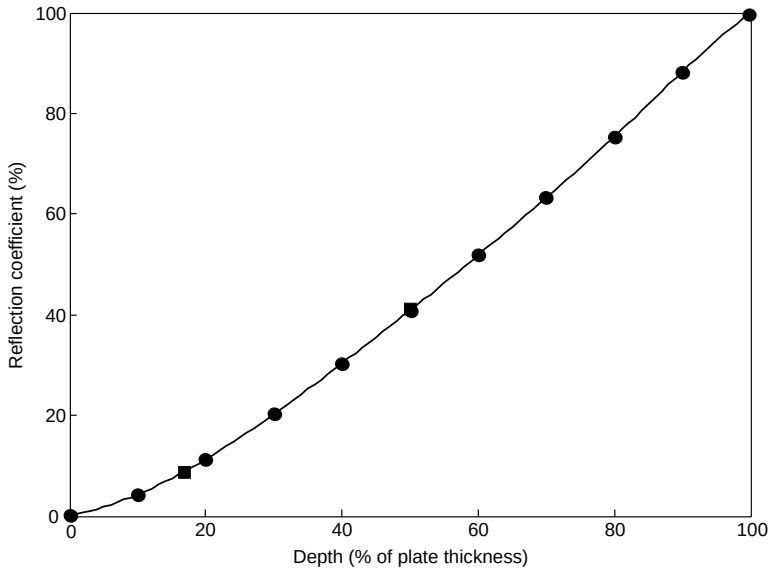

Figure 3.5: Reflection coefficient of the S_0 mode at 50 kHz from a 5 mm wide notch as a function of notch depth (•). Comparison values (at 17 and 50% depth) are obtained from [31], and are shown by square markers (■).

was found. Le Clezio et al. [83] used aluminium plates in their work, so their results could thus not be compared directly.

The reflection of the A_0 mode

At frequencies below 1 MHz-mm (below 100 kHz with the 10 mm thick plate of figure 3.2), the A_0 mode is not very attractive for practical guided wave testing, as it is highly dispersive, which leads to a spread of the excited wave packet in space and time, and consequently reduced resolution. The effects and optimisation possibilities of guided wave testing are discussed in detail by Wilcox et al. [50].

Despite this increased complexity compared with the S_0 mode, the evaluation as presented for the S_0 mode is repeated here for the A_0 mode. However, the discussion is similarly limited to the single frequency of 50 kHz. A detailed analysis of the reflection from the A_0 mode from cracks and notches is given in Lowe et al. [29].

Figure 3.6 shows the displacement (u) and stress (σ) mode shapes of the A_0 mode at 0.5 MHz-mm in (a) and (b), respectively. With the x, y and z directions denoting the normal to the plane strain, the normal to the surface of the plate, and the direction of propagation of the excited wave, respectively, the

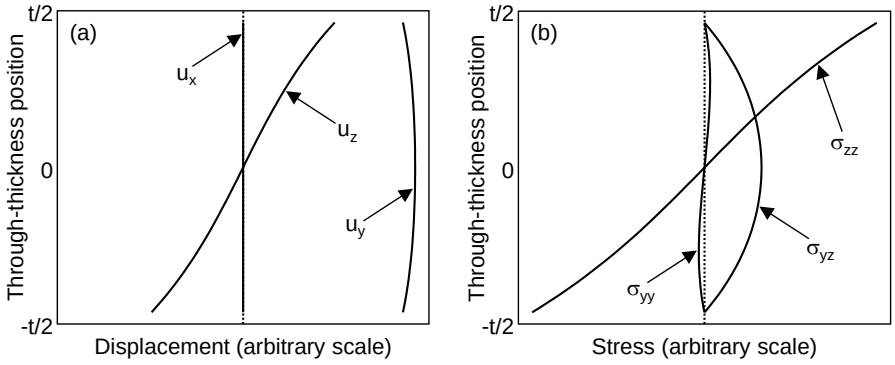

Figure 3.6: Displacement (a) and stress (b) mode shapes for the A_0 mode at 0.5 MHz-mm.

A_0 mode can be seen to have significant displacement and stress components in both the u_y and u_z directions. At this frequency the mode shapes in the direction of propagation varies roughly linearly through the thickness of the plate, which indicates simple bending movement of the plate [29]. The out of plane displacement component is significant. Also, the increasing stress component in the direction of propagation (σ_{zz}) towards the plate boundaries indicates that there will be some mode conversion into the S_0 mode as it exhibits a large σ_{zz} component of constant amplitude through the plate thickness, as shown in figure 3.4 (b).

The mode is excited by applying a force at the centre node in the direction normal to the surface of the plate (y), achieving single mode excitation. Figure 3.7 shows the RC for the A_0 mode as a function of notch depth at 50 kHz, which was calculated as the ratio between the u_y component of the reflected wave to that of the incident wave at the monitoring node 0.4 m from the excitation, as indicated in figure 3.2. The RC can be seen to be considerably more difficult to interpret than that of the S_0 mode at the same frequency due to the complexity of the A_0 mode shapes. For notch depths in the range from 0-20% of the plate thickness, the RC increases linearly, but then stays roughly constant up to around 50%, and is even slightly reduced towards 40%, before it rises sharply from 50% to the through-thickness depth. Lowe et al. similarly reported considerable complexity in the variation of the RC as a function notch or crack depth and width in their paper [29]. They mainly did their investigations at higher frequencies, so only a single value was available for direct comparison in figure 3.7, of the same reasons as explained in Section 3.2.

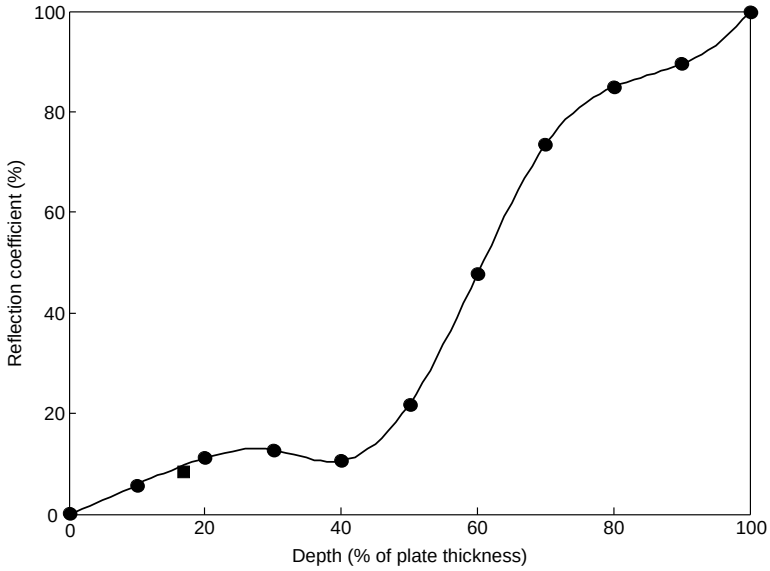

Figure 3.7: Reflection coefficient of the A_0 mode at 50 kHz from a 5 mm wide notch as a function of notch depth. A single comparison value (at 17% depth) from Lowe et al. [29] is shown by the square marker (■).

The reflection of the SH_0 mode

As discussed in Section 2.3, guided waves can exist in a plate either as Lamb waves, which have particle displacement entirely in the $y-z$ plane, or as shear horizontal waves, for which the particle displacement is perpendicular to the plane of propagation. Modelling SH_0 excitation and propagation is not possible by employing the 2D plane stain model used in the previous sections, as 2D plane strain elements have no out of plane degree of freedom. To avoid full 3D models, a quasi-3D model was constructed, as shown in figure 3.8.

By using a single layer of 3D elements, where all nodes in the $y-z$ plane are rigidly linked together with their corresponding nodes in the x direction so that the displacement in the x direction is the same at both nodes present at each specific location in the $y-z$ plane, SH_0 waves could be excited [91]. These rigid connections are indicated by thicker black lines in the figure.

The enlarged section of the figure shows the excitation of the SH_0 mode, which was done by applying forces in the x direction at nodes at the chosen excitation location, as indicated in figure 3.2. Figure 3.8 indicates that forces were applied at all nodes through the plate thickness at the given position in the $y-z$ plane; calculations have also been done with forces being applied at the centre node only, the results of which will be discussed below.

An important property of the fundamental shear horizontal mode is that

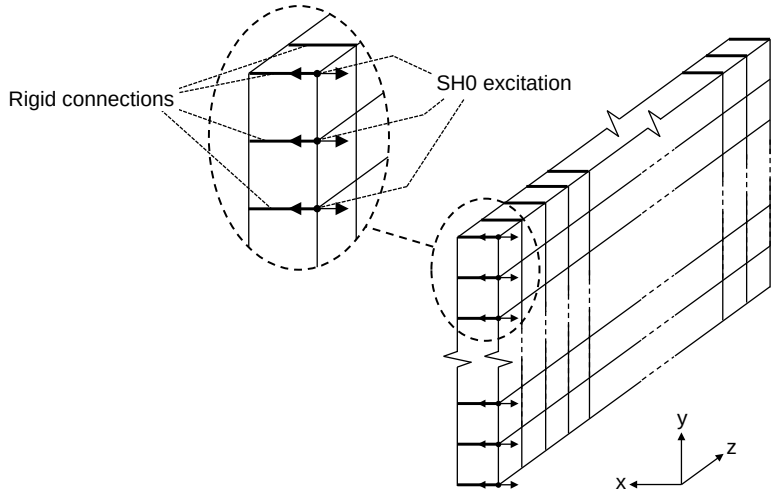

Figure 3.8: Schematic of 2D FE model of SH_0 mode propagation.

its displacement and stress mode shapes are constant through the thickness of the plate as seen from figure 3.9, which shows the displacement (u) and stress (σ) mode shapes for the SH_0 mode at 50 kHz in the 10 mm thick steel plate.

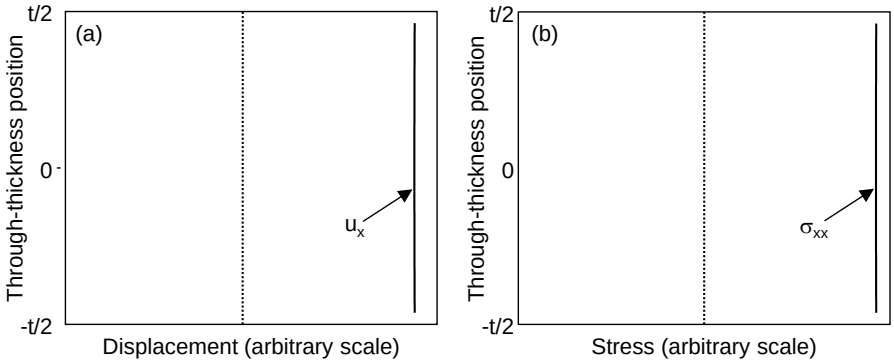

Figure 3.9: Displacement (a) and stress (b) mode shapes for the SH_0 mode at 0.5 MHz-mm.

Figure 3.10 shows RCs as a function of notch depth, calculated for the same 5 mm wide notch as discussed in the previous sections with the S_0 and A_0 modes incident. The RC can be seen to be an approximately linear function of notch depth. RCs were calculated at monitoring position 0.4 meters along the plate as the ratio between the u_x component of the reflected wave to that of the

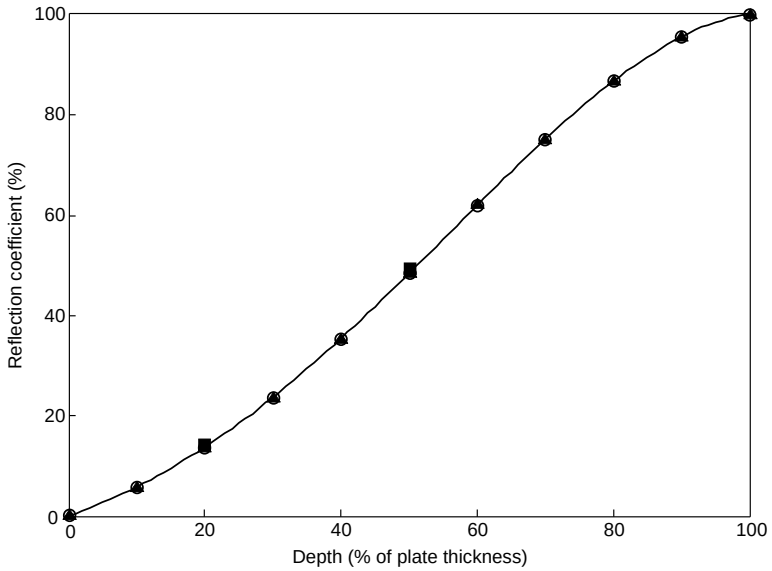

Figure 3.10: Reflection coefficient of the SH_0 mode at 50 kHz from a 5 mm wide notch as a function of notch depth. Results with excitation at all nodes (○), single node (▼), and results from Demma et al. [30] (■) are included.

incident wave; the excitation force was applied in the x direction at all nodes through the wall thickness at the specific location in the $y-z$ plane giving the same results as excitation at a single node. Also, excellent agreement was found with the results of Demma et al. [30] at 20 and 50% depth, albeit obtained at a slightly higher frequency-thickness product (0.55 MHz-mm).

The main shape of the RC as a function of depth is also in good agreement with the analyses reported by Demma et al. [11] on the reflection of the fundamental torsional mode from axisymmetric notches with varying depth in a pipe, when we know from Section 2.4 that the SH_0 mode in a plate corresponds to the T(0,1) mode in a pipe. They also reported that the same trend was generally seen at all frequencies and axial extents investigated.

3.3 The reflection and scattering from a circular through-thickness hole in a plate

The work reported in this section is done using full 3D finite element models, modelling through-thickness circular holes in a steel plate. The same material parameters as in Section 3.2 are used in this section, except for the cases with plane S_0 mode incidence, when they are adjusted slightly (to $\rho = 7850$ kg/m^3, $E = 210$ GPa and $\nu = 0.3$) to use the same values as Diligent et al. [31]. As

mentioned in Section 3.1, a 2D plane strain model could be used to describe this problem. Still, as the work on through-thickness holes was thought of as an initial and validative study before moving on to part-thickness holes, a full 3D model was chosen so that the same model could be used in both cases. However, as work progressed it was found more appropriate to continue the part-thickness studies in a pipe structure, which will be discussed in subsequent chapters.

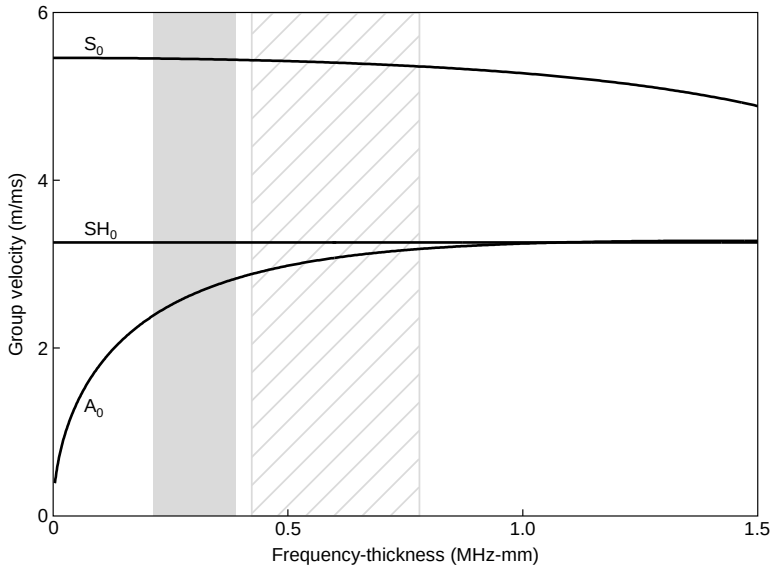

Figure 3.11: Group velocity dispersion curves for a steel plate. The grey and the diagonally lined areas indicate the ±15 dB bandwidth obtained for a 3 and 6 mm thick plate with a 5 cycle Hanning windowed excitation with centre frequency of 100 kHz, respectively.

Figure 3.11 shows the group velocity dispersion curves as a function of the frequency-thickness product for a steel plate. The grey area indicates the ±15 dB bandwidth of the 5 cycle Hanning windowed toneburst with centre frequency of 100 kHz employed in the case of a 3 mm thick plate, as used in with plane SH_0 wave incidence, while the area indicated by diagonal lines shows the same for the 6 mm thick plate used with plane S_0 wave incidence. As can be seen, both the S_0 and SH_0 modes are essentially non-dispersive in these frequency regions, and well below the cut-on of the higher order S_n and SH_n modes.

A 3D plate model of dimensions 1.8 x 1.8 m and thickness 3 mm is shown in figure 3.12. The steel plate itself is 1.2 x 1.2 m, extended in all directions by absorbing regions of length 0.3 m, which are indicated by dashed diagonal lines in the figure. All absorbing regions throughout this section are ALIDS with the same parameters as in Section 3.2. As the S_0 mode is the fastest propagating

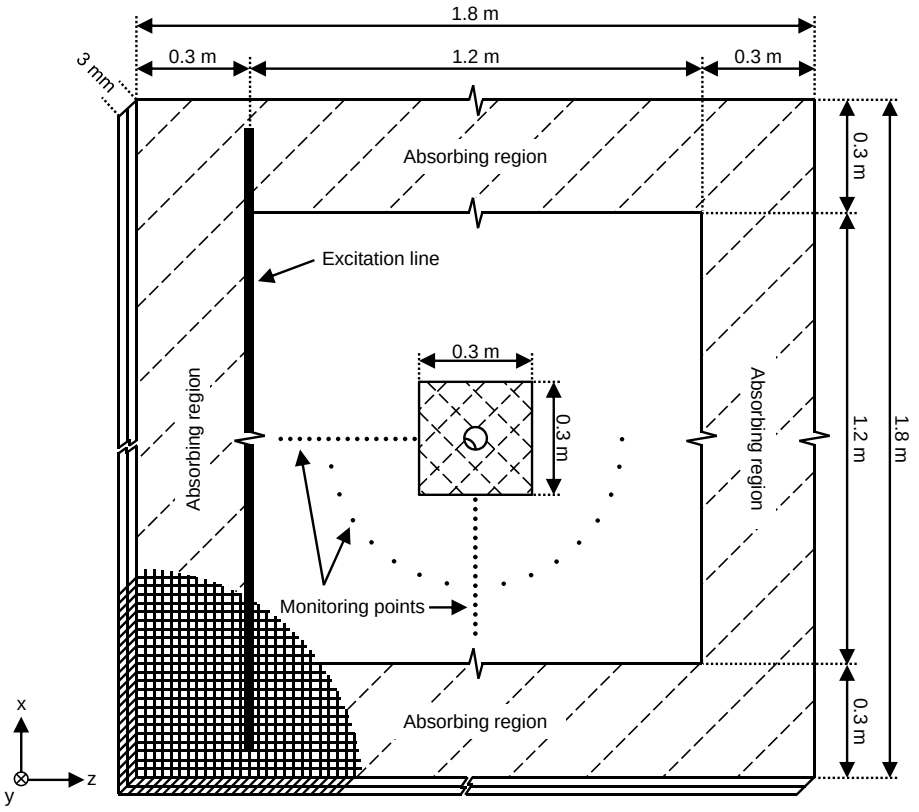

Figure 3.12: Schematic of 3D plate model.

mode within the bandwidth of the excitation signal, it governs the extent of the absorbing regions. The absorbing regions are almost 4 times the length of the wavelength of S_0 mode at the lower end of the bandwidth (70 kHz), and more than 5 times its wavelength at the centre frequency of 100 kHz. These geometrical parameters were kept throughout this section, as the S_0 mode also is excited by mode conversion at the defect when a plane SH_0 wave is incident on the hole, as will be discussed throughout this section.

A structured mesh consisting of 8 noded square elements is used throughout the plate model, except in the hatched area of size 0.3 x 0.3 m around the circular defect as indicated in figure 3.12, where 8 noded hexahedral elements are used. The hexahedral elements are chosen because they represent circular shapes better than square elements. Figure 3.13 (a) and (b) shows an example of how a hole with diameter 60 mm is modelled by the square and hexahedral elements (with an element size of 3 mm), respectively. Convergence studies have shown that 15 elements around the circumference of the hole are necessary in

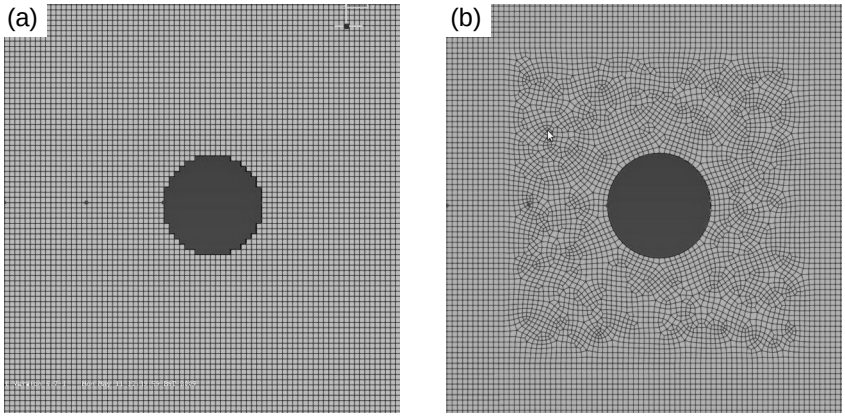

Figure 3.13: Element types; (a) square, (b) hexahedral.

order to model it properly with tetrahedral elements, a number which must be increased to 30 if square elements are used [76]. However, a transition between square and tetrahedral elements generates unwanted reflections as the nodes of these two element types cannot be joined together sufficiently well at the boundary between them. Hexahedral and tetrahedral elements were here considered to be comparably adaptive to circular shapes, so the same requirement of >15 elements around the hole circumference was set also for hexahedral elements.

The element size is governed by the shortest wavelength present, as there should be at least 10 nodes per wavelength when employing square meshes [78], and even more with other element types [76]. In this case, the shortest wavelength originates from the wavelength corresponding to the highest frequency component of the SH_0 mode within the bandwidth. An element size of 1.5 mm is used throughout with plane SH_0 wave incidence in this section, resulting in around 35 elements per wavelength at 100 kHz. With plane S_0 wave incidence, the work of Diligent et al. [31] is followed in detail, so the same mesh size of 3 mm as they used is applied, resulting in approximately 10 elements per wavelength of the SH_0 mode at 100 kHz.

ABAQUS gives a time increment requirement for explicit solving as given in equation 2.37 [74]. The parameter D is the shortest distance between two nodes in an element, which is equal to the mesh size for square elements, but is smaller for hexahedral and most other element types. The requirement used here is

$$\Delta t \leq 0.4 \frac{D}{c_{\max}}, \tag{3.1}$$

where $c_{\max}$ is the velocity of the fastest propagating mode present. The factor 0.4 is determined empirically with use of hexahedral and tetrahedral elements,

a requirement also found to be somewhat influenced by the presence of absorbing regions. Hence, a time step of 200 ns was employed with plane S_0 wave incidence, which was refined to 100 ns with plane SH_0 wave incidence.

The excitation of the plane wave is done by applying the excitation toneburst as prescribed forces at all the nodes at the centre position of the plate thickness along $z = 0.3$ m, as indicated by the thick line in figure 3.12. The model is partitioned along the excitation line, so that all the excitation nodes are at exactly $z = 0.3$ m. If the displacements are applied in the z direction, the S_0 mode will be excited, while the SH_0 mode requires excitation in the x direction. The excitation is extended $^3/_4$ into the absorbing regions to obtain a plane wave excitation that extends entirely in the x direction between the absorbing regions. The end nodes of the excitation excite cylindrically spreading waves, which are partially damped out when the excitation is extended into the absorbing region. This leads to certain reflections from the edges of plate, which are removed by baseline subtraction. In performing baseline subtraction, a simulation without any defect present is subtracted from the simulations with a defect present. Furthermore, baseline subtraction also enables the use of a wider monitoring range, as the incident signal otherwise mask reflections at monitoring points close to the defect. The incident wave amplitude must be obtained from the simulations with a defect present, but is much larger than the unwanted reflections removed by the baseline subtraction, so the error in the incident wave amplitude is negligible.

Monitoring points are indicated by dots in figure 3.12. All monitoring points were at the centre position through the plate thickness. Series of monitoring points were placed along x and z directions centered with respect to the hole, from the beginning of the structured mesh area outwards in steps of 1 cm, to assess the variation of the reflections as a function of distance from the hole. Additionally, in order to assess the angular scattering pattern from the hole, 17 monitoring points were placed at angles from 0 to 180 degrees relative to the incident wave in steps of 11.25 degrees, at a distance of 0.39 m from the centre of the hole. This distance was chosen to ensure that the reflected S_0 and SH_0 waves arrived separated in time.

RCs are calculated as in Section 3.2 as the ratio between the relevant displacement component of the reflected wave to that of the incident wave in frequency domain. Additionally, RCs are calculated using the Hilbert transform for comparison, which is a time domain approach where the envelope of the time traces is used as basis for the RC calculation. The RC is calculated by dividing the maximum value of the envelope of the reflection by that of the incident signal, thus neglecting undulations due to higher order reflections such as creeping waves, the effect of which will be assessed. Furthermore, the frequency at which the maximum RC is obtained from the Hilbert envelope is unknown; comparisons with frequency domain results are therefore only likely to be useful when reasonably narrow frequency bandwidth signals are used.

Plane S_0 wave incidence

Following the excitation procedure explained in the previous section, a plane S_0 wave was excited in a 6 mm thick steel plate. Figure 3.14 shows a snapshot of the wave propagation and scattering from a 60 mm diameter through-thickness hole, where the magnitude of all three displacement components (u_x, u_y and u_z) combined is shown.

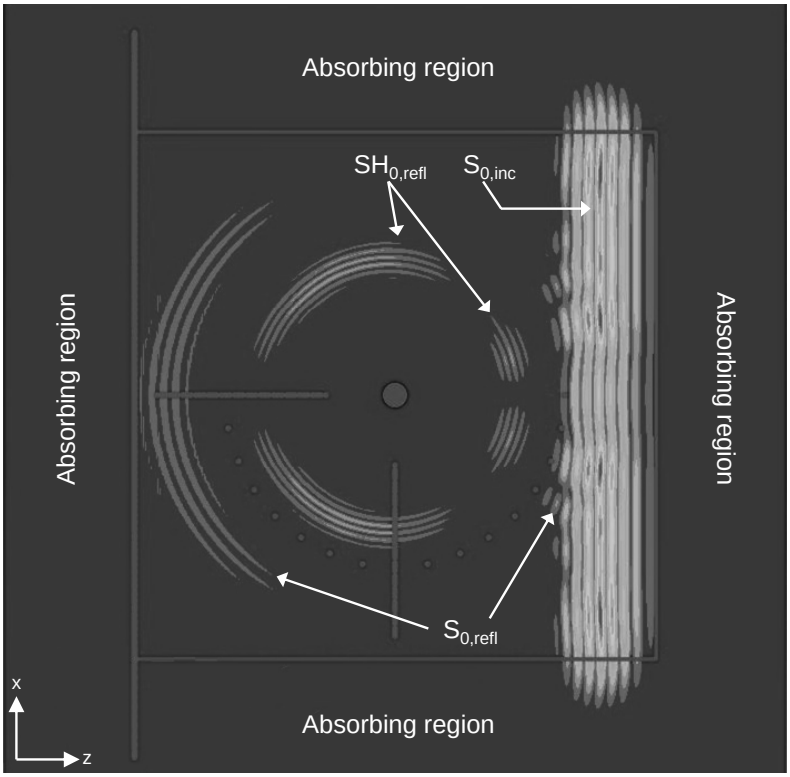

Figure 3.14: Wave propagation and scattering with plane S_0 wave incidence.

In the snapshot, the incident plane S_0 wave has propagated in the z direction past the defect, and is about to enter the absorbing region in the right hand end of the plate. The plane wave can be seen to be constant over the plate length as it is damped out within the absorbing layers, except for the influence caused by propagation through the hole. S_0 and mode converted SH_0 waves are scattered in all directions with varying amplitude due to the interaction with the hole. As the S_0 mode propagates faster than the SH_0 within the bandwidth of the incident wave, its reflection separates itself from the scattered SH_0 at a certain distance from the hole. Their different scattering patterns can clearly be seen

from figure 3.14. Note also that the scattered S_0 wave amplitude cannot be separated from the incident plane wave within a large angular section in the transmitted direction, thus illustrating the necessity of baseline subtraction.

Direct reflection of the S_0 mode with plane S_0 mode incidence

The incident plane S_0 wave propagates in the positive z direction; this subsection concerns the direct reflection (reflection directly back in the negative z direction) of the S_0 mode from the hole. Figure 3.15 (a) shows the RC, calculated as the ratio between u_z of the reflected wave to that of the incident wave, as a function of distance from the edge of the hole for circular holes of diameter 60, 120 and 144 mm, where the solid lines show results calculated from the Hilbert envelope of the signals, while the dashed line RCs are calculated using the frequency domain technique. The circular markers show results obtained by Diligent et al. [31] for the same cases, for comparison and validation.

As expected, the RCs decrease with increasing distance to the hole, and with decreasing hole size. The undulations in the RCs in the frequency domain calculations arise due to secondary reflections, which include reflections of the SH_0 mode that decay quickly with distance [31], and also circumferential creeping waves that propagate around the circumference of the hole and are then re-radiated back towards the receiver points. The issue of creeping waves is discussed in detail by Nagy et al. [92, 93], and will become more apparent when the reflection from an incident plane SH_0 wave is addressed below. It is evident from the nature of the Hilbert transform and figure 3.15 that such a time domain approach neglects the effect of secondary reflections.

The values obtained from Diligent et al. [31] show excellent agreement for 60 and 120 mm hole diameters, but not for 144 mm. However, if the distance from the hole that the RCs are plotted against is normalised to the hole diameters, as figure 3.15 (b) shows for the Hilbert envelope results shown in (a), the reflections at the given frequency are the same. This was also found by Diligent, which suggests that the error in the 144 mm hole diameter case is simply due to mislabelling. The RCs decay follows the ideal spreading function of cylindrical waves, as the amplitude is inversely proportional to the square root of the distance from the hole.

Scattering of the S_0 and SH_0 modes as a function of angle with plane S_0 mode incidence

Scattering of the S_0 and SH_0 modes from a through-thickness hole with an incident plane S_0 wave is reported in this subsection. The scattering amplitudes of the two modes were calculated as the ratio of the in-plane displacement amplitude of the given mode to the displacement in the z direction of the

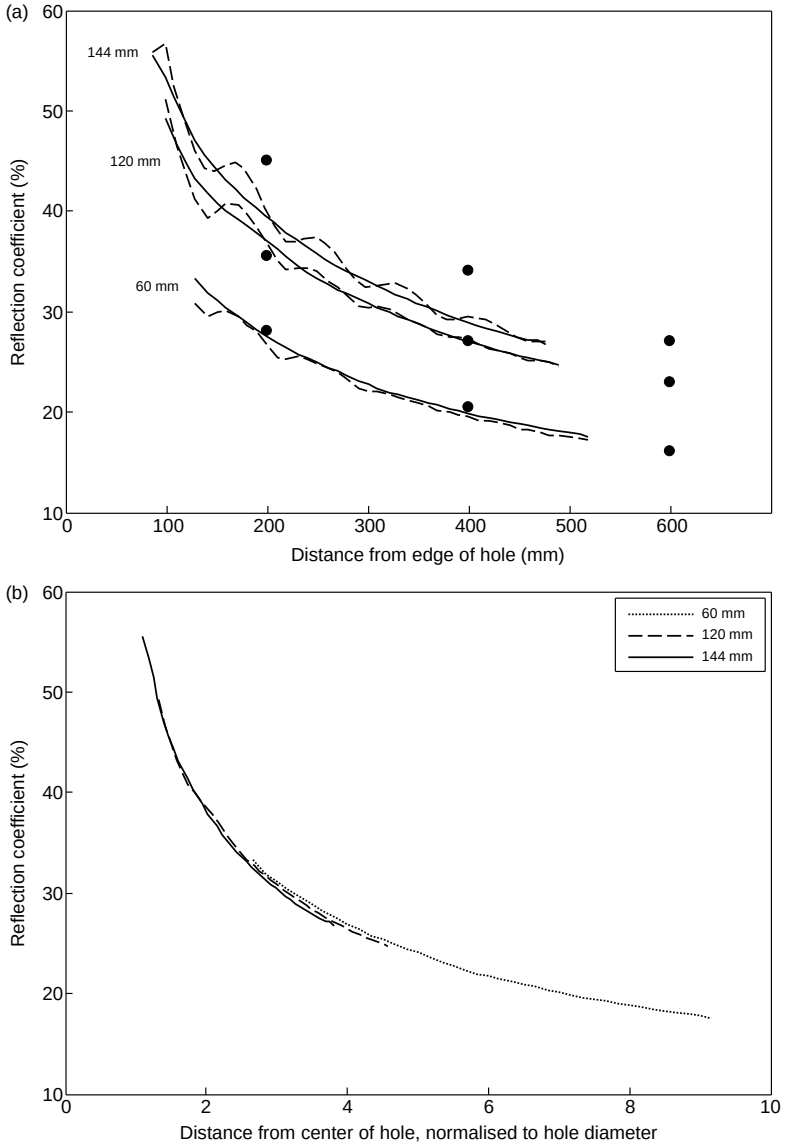

Figure 3.15: Variation in RC of the backscattered S_0 wave from a circular through-thickness hole at 100 kHz as a function of distance from the hole in (a), where the solid and dashed lines show results calculated using the Hilbert transform and frequency domain technique, respectively. The markers indicate the corresponding results in Diligent et al. [31]. (b) shows the RC as a function of distance from the centre of the holes, normalised to hole diameter, calculated using the Hilbert transform.

incident plane S_0 wave, where the former is calculated as

$$u_{S_0} = u_x \sin\theta + u_z \cos\theta, \tag{3.2a}$$

$$u_{SH_0} = u_x \cos\theta - u_z \sin\theta, \tag{3.2b}$$

for the scattered S_0 and SH_0 modes, respectively, and θ is the angle between the propagation directions of scattered wave and the incident plane wave.

In order to validate the FE model further, results were compared with an analytical implementation of the scattering from circular holes using approximate Poisson theory done by Cegla et al. [32]. In their implementation Cegla and co-workers also normalised the scattering amplitude to correct for both the cylindrical decay of the wave propagation and the thickness of the plate as their model also allows part-through thickness of the hole, calculating the relative amplitude of the scattered modes as

$$U^{\infty}_{r,\theta,z}(\theta) = \frac{|u_{r,\theta,z}(r,\theta)|}{\max(|u^{\text{inc}}_r(a,\theta)|)}\sqrt{\frac{2r}{t}} \quad \text{as} \quad r \to \infty, \tag{3.3}$$

where a is the radius of the hole, t is the thickness of the plate and r is the distance at which the scattered waves are evaluated. FE results were obtained at a distance of 0.39 m from the centre of the hole, while the analytical implementation returned values at 0.5 m distance. The normalisation imposed by the square root in equation 3.3 was accounted for in the post-processing of the FE simulations.

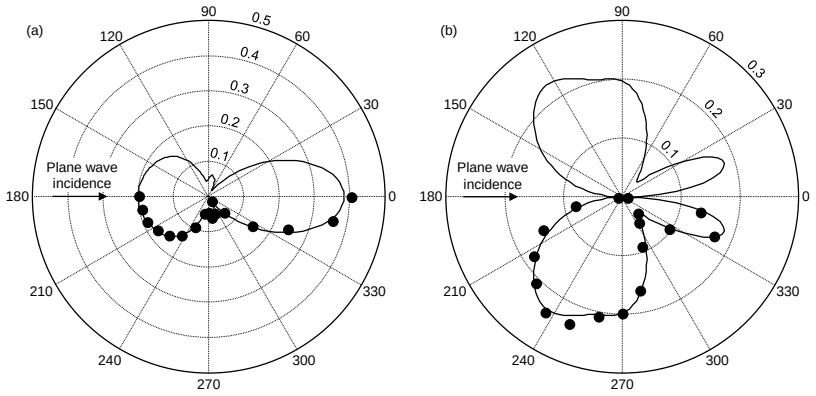

Figure 3.16: Reflction ratio of the (a) S_0 and (b) SH_0 modes with a plane S_0 wave incident at a 60 mm diameter through-thickness hole at 100 kHz as a function of scattering angle. The radial axis corresponds to the magnitude of the displacement, and is indicated in steps of 0.1. The solid lines are calculated using the analytical implementation of Cegla et al. [32] and the markers show the FE results.

Figure 3.16 shows the reflection ratio from a 60 mm diameter through-thickness hole at 100 kHz as a function of scattering angle, where 180° corresponds to the direction of the incident plane S_0 wave, as indicated in the figure. The circular markers indicate values calculated from the FE analyses, while the lines are calculated using the analytical implementation. Excellent agreement can be seen in both cases. The S_0 mode can be seen to be strongest scattered in the specular (≈ 0.2 at 180°) and transmitted (≈ 0.4 at 0°) directions, and only marginally scattered in the 90 and 270° directions. The mode converted SH_0 wave on the other hand has an amplitude approaching zero in the specular and transmitted directions, while exhibiting the largest reflection ratio of roughly 0.2 from 90-140° and 220 to 270°. Thus, the reflection of both modes are strongly dependent on the scattering angle.

Plane SH_0 wave incidence

A similar study as discussed with plane S_0 incidence in the previous section is presented with plane SH_0 wave incidence in this section. The excitation procedure used to excite the plane SH_0 wave in the 3 mm thick steel plate is explained in the introductory part of Section 3.3, applying the excitation toneburst in the x direction at all nodes at the centre of the plate thickness along the excitation line indicated in figure 3.12, to achieve plane SH_0 wave excitation.

Figure 3.17 (a) and (b) shows snapshots of the wave propagation with a hole of diameter 60 and 3.75 mm, respectively, showing the magnitude of all three displacement components (u_x, u_y and u_z) combined. The hole is not centred on the plate in these cases, which is done in order to save computation time. The incident plane SH_0 wave is labelled $SH_{0,\mathrm{inc}}$, and can be seen to propagate as a plane wave over the x extent of the plate in the z direction. The efficiency of the absorbing regions is clearly visible, as the waves entering them are damped out with negligible reflections. The noise due to the finite length approximation of the plane wave excitation is indicated in (b), and is a magnitude or so less than that scattered from the 3.75 mm hole. However, both the noise due to the finite plane wave excitation and the noise due the reflection of the incident plane wave from the model edges were removed by baseline subtraction.

The mode converted S_0 wave, $S_{0,\mathrm{refl}}$ propagates fastest, and arrives at the receivers first. However, a certain propagation distance is necessary before it is separated from the scattered SH_0 wave, labelled as $SH_{0,\mathrm{refl}}$, as is evident from figure 3.17. With the 60 mm diameter hole shown in (a), the first order creeping wave, $SH_{0,\mathrm{refl,cr}}$, can be seen to arrive separately from the directly reflected $SH_{0,\mathrm{refl}}$ wave. This is also evident from figure 3.18, which shows example time records of the backscattered reflection from the hole at 0.39 m from the centre of the hole, where the records in (a), (b) and (c) correspond to hole diameters of 3.75, 30 and 60 mm, respectively. The amplitudes of the reflections are normalised to the same reference. A small component of the S_0 wave can be

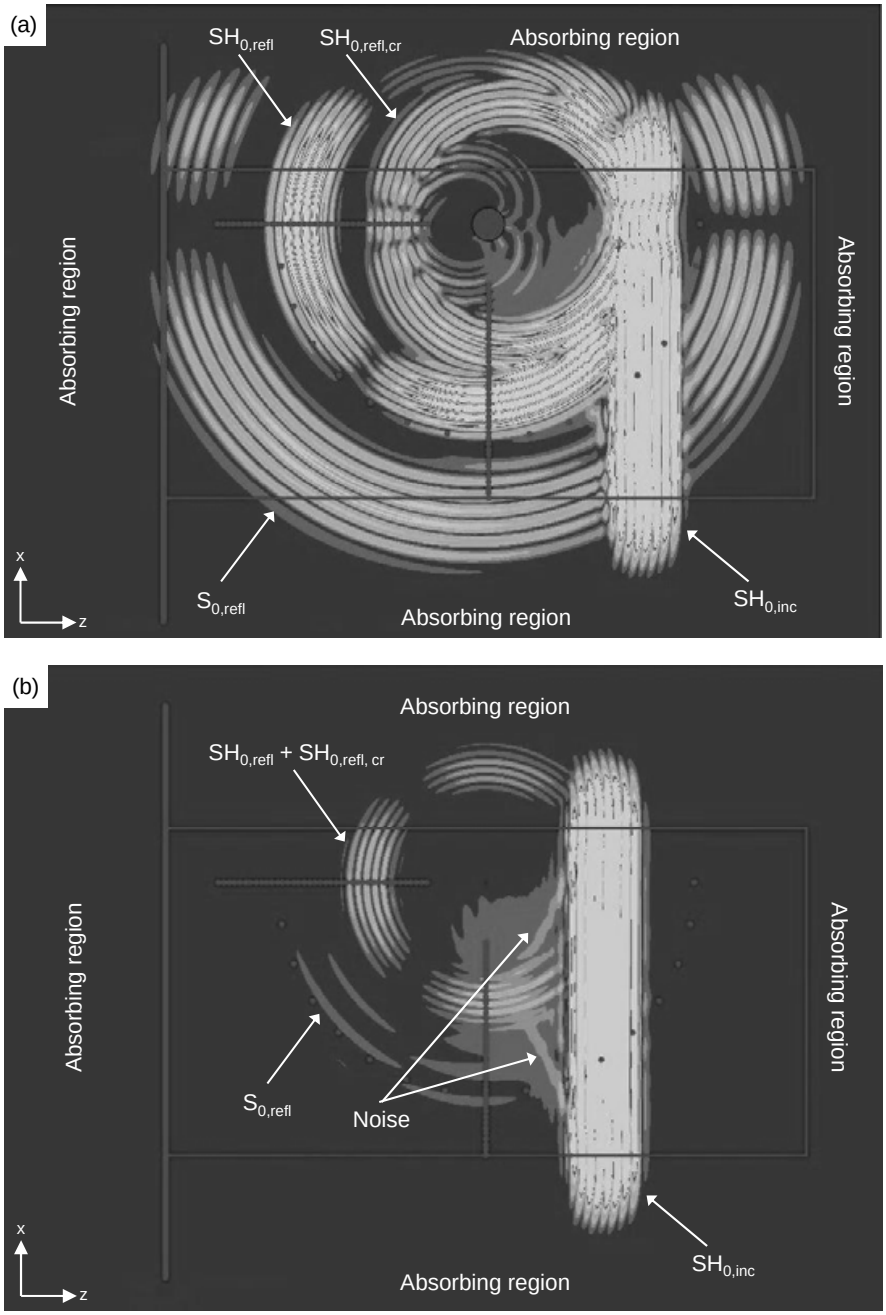

Figure 3.17: Wave propagation and scattering with a plane SH_0 wave incident on a through thickness circular hole of diameter (a) 60 mm and (b) 3.75 mm.

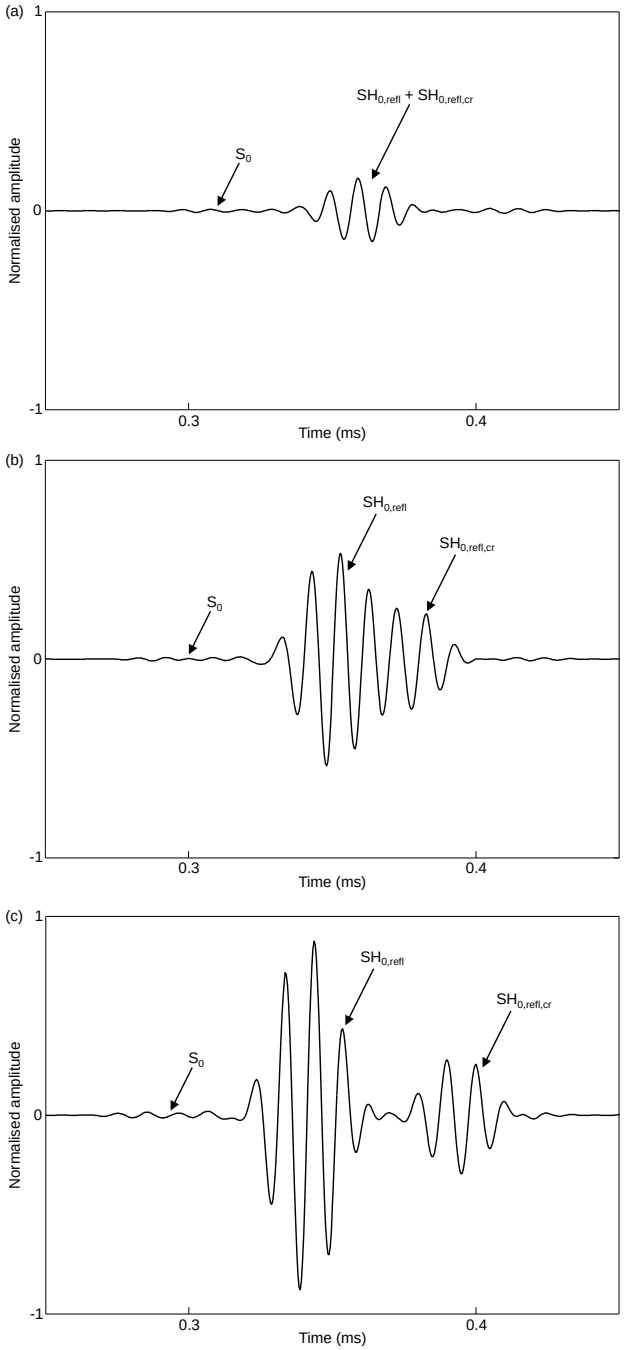

Figure 3.18: Time record of the direct reflection of the plane SH_0 wave from through-thickness holes of diameter (a) 3.75 mm, (b) 30 mm, and (c) 60 mm, obtained at 0.39 m from the centre of the hole.

seen to arrive first in all cases, which will be increasingly separated in time from the shear horizontal reflected waves with monitoring distance. In figure 3.18 (c) the directly reflected SH_0 mode is separated from the creeping wave reflection by 0.056 ms, which corresponds to the time it takes for an SH_0 wave to propagate around the circumference of a 60 mm hole. Additionally, as both the $SH_{0,\mathrm{refl}}$ and $SH_{0,\mathrm{refl,cr}}$ propagate with the same velocity, their separation is constant regardless of propagation distance. Thus, for smaller hole sizes the scattered and creeping wave reflections cannot be fully separated in time, as is evident from figure 3.18 (a) and (b). With the 30 mm diameter hole in (b), the reflections from the scattered and creeping wave reflections partly interfere with each other, while they cannot be distinguished from each other with a 3.75 mm diameter hole, as shown in (a).

Direct reflection of the SH_0 mode with plane SH_0 mode incidence

As the incident plane SH_0 wave propagates in the positive z direction, the direct reflection from a defect propagates back in the negative z direction; this subsection concerns the direct reflection of the SH_0 mode from a circular hole.

Figure 3.19 (a) shows the RC from a circular through-thickness hole as a function of distance from the hole for holes of size 3.75, 15, 30 and 60 mm in diameter, as indicated on the figure. RCs were calculated as the ratio between displacement component in the x direction (see figure 3.12) of the reflected wave to that of the incident wave. Dashed lines show results calculated using the Hilbert transform, while the solid lines show the corresponding frequency domain calculations. Good agreement can be seen between for the two calculation methods with a 60 mm diameter hole, as the creeping wave reflection can be gated out in time. The undulations seen in the 60 mm case are mainly be due to the reflected S_0 waves, as their amplitudes are reduced with distance from the hole. For the three other hole sizes, the direct and creeping wave cannot be evaluated separately. The interference between the direct and creeping wave reflections depends on the size of the hole, as the delay of the creeping wave with respect to the direct reflection is governed by it. As both the direct and creeping wave reflections travel with the same velocity, the amplitude offset of the Hilbert transform calculations compared with the frequency domain calculations is constant, except for the undulations in the frequency domain results.

In figure 3.19 (b) the RCs are shown as a function of the distance from the centre of the hole in question, normalised to the hole size, and calculated using the Hilbert transform. As found with plane S_0 mode incidence above, the RCs decay proportionally to the inverse of the square root of the propagation distance from the source. The discrepancies between the results for different hole sizes are thought to be caused by the variable influence of the creeping wave reflections.

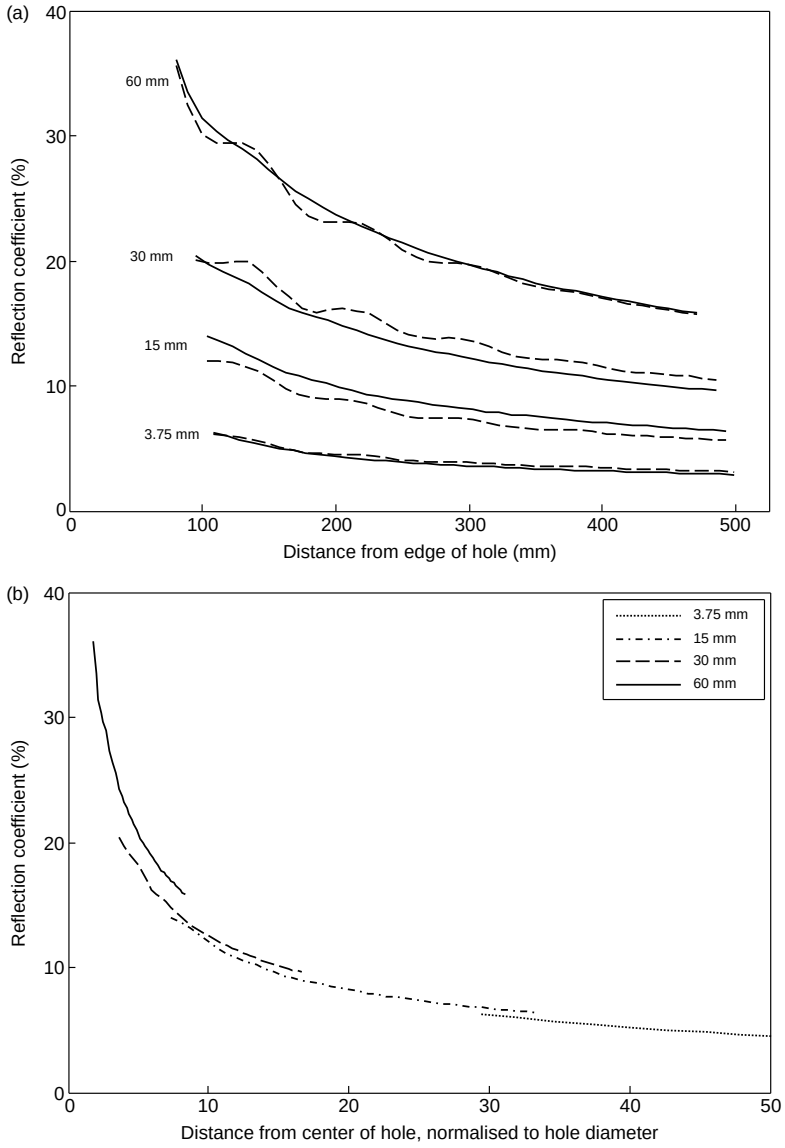

Figure 3.19: Variation in RC of the backscattered SH_0 wave at 100 kHz as a function of (a) the distance from the hole, where the solid and dashed lines indicate results calculated using the Hilbert transform and frequency domain technique, respectively, and (b) the distance from the centre of the holes, normalised to hole diameter, calculated using the Hilbert transform. Hole sizes are indicated in the figure in (a) and in the figure legend in (b).

Reflections at 90 degrees from the hole with plane SH_0 wave incidence

This subsection discusses the scattering of the S_0 and SH_0 waves at 90° relative to the plane of incidence of the plane SH_0 wave. Figure 3.20 shows the RC of the scattered SH_0 mode as a function of distance from the edge of the hole for various hole sizes, as indicated in the figure legend. Thus, RCs were calculated as the ratio between the u_z component of the wave scattered 90° relative to the plane of incidence to the u_x component of the incident (SH_0) wave. Calculations were done both using the Hilbert transform and the frequency domain approach, and are indicated by solid and dashed lines, respectively. Note that the labels in the figure here refer to the solid line Hilbert transform results, while the frequency domain calculations are indicated specifically in the figure legend as the RCs do not increase monotonically with hole diameter, the reasons for which are explained below.

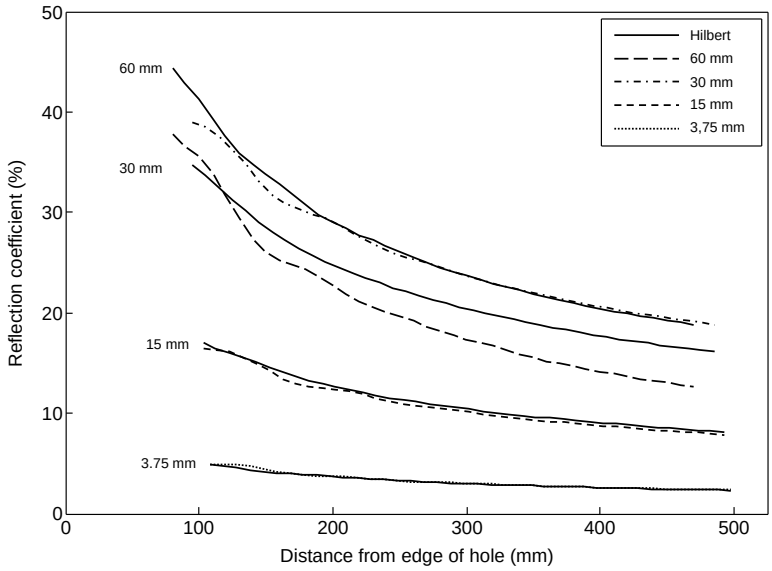

Figure 3.20: Variation in RC as a function of distance from a circular through-thickness hole of diameter 3.75, 15, 30 and 60 mm for the SH_0 wave reflected at 90° relative to the plane of incidence at 100 kHz. The solid and dashed lines indicate results calculated using the Hilbert transform and frequency domain technique, respectively.

All the RCs calculated with the frequency domain approach exhibit undulations that decay in amplitude as the scattered SH_0 waves propagate away from the hole, which suggests that this is due to the scattered S_0 wave. As seen in the previous subsection for the directly reflected waves, the creeping SH_0 wave

has strong influence on the RCs. However, as the creeping waves here only need to propagate partly around the circumference of the hole, their delay in time compared with the directly scattered wave is shorter. Indeed this is also seen from the time records, where the creeping wave cannot be distinguished from the direct reflection for either 3.75, 15 or 30 mm diameter holes, and only partly with the 60 mm diameter hole.

In the cases of the 3.75 and 15 mm holes, the RCs calculated using the two methods can be seen to be comparable, which suggests that the creeping waves are reasonably in phase with the directly scattered waves. The same cannot be said for the 30 and 60 mm diameter holes, as the RC for the 30 mm hole approaches the same amplitude as with the 60 mm diameter hole in the Hilbert transform calculations, and is larger for the 30 mm diameter hole than for the 60 mm hole when the frequency domain approach is applied. As a consequence of the strong influence of the creeping waves on the RCs, they cannot be well normalised with hole diameter as done in e.g. figure 3.15 (b).

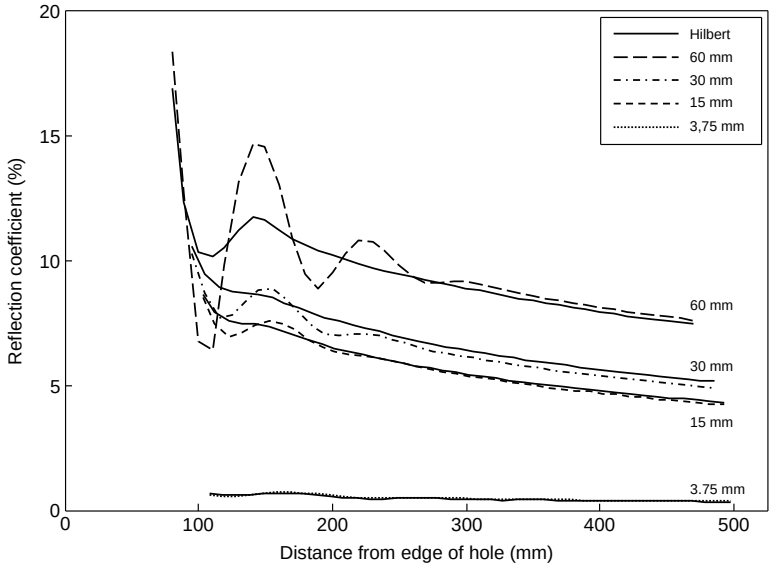

Figure 3.21: Variation in RC as a function of distance for a circular through-thickness hole of size 3.75, 15, 30 and 60 mm at 100 kHz for the S_0 wave reflected at 90° relative to the plane of incidence. Calculations are done using the Hilbert transform (solid lines) and the frequency domain technique (dashed lines).

Figure 3.21 shows the RC of the scattered S_0 wave at 90° relative to the plane of incidence for the same hole sizes as a function of distance from the edge of the hole at 100 kHz. The S_0 wave scattered 90° relative to the plane

of incidence is given by the u_x component along this direction, so RCs were calculated as the ratio between this displacement component, to u_x of the incident SH_0 wave. A strong influence of SH_0 waves on the RCs can be seen at distances close to the edge of the hole due to radial components that decay quickly with distance, as in the case with specularly reflected S_0 waves [31]. The amplitude of the undulations is large as the amplitude of the scattered SH0 wave is almost 4 times that of the S_0 in the direction 90° relative to the plane of incidence. At larger distances the agreement between the Hilbert transform and frequency domain approaches is good; the slight difference seen being due to the creeping S_0 wave scattered in this direction.

Scattering of the S_0 and SH_0 modes as a function of angle with plane SH_0 wave incidence

This subsection concerns the scattered field around a through-thickness hole of various size with plane SH_0 wave incidence, comparing results obtained from FE analyses with the analytical implementation of Cegla et al. [32]. The analyses are limited to the centre frequency of 100 kHz of the incident toneburst. Figure 3.22 shows the calculated reflection ratios as a function of scattering angle, where 180° corresponds to the direction of the incident plane SH_0 wave, as indicated in the figure, for both the mode converted S_0 mode ((a), (c), and (e)) and the scattered SH_0 mode ((b), (d), and (f)), for holes of diameter 60 ((a)-(b)), 30 ((c)-(d)) and 15 ((e)-(f)) mm. Markers indicate values obtained from the FE analyses, and lines show the results from the analytical implementation. The reflection ratios are calulated similarly as described above in assessing the scattering as a function of angle with plane S_0 wave incidence, employing to ratio between the displacement amplitudes of the scattered modes as given by equations 3.2 to that of the incident SH_0 mode, which is given by u_x. Note that the radial scale showing the magnitude of displacement varies between the different plots.

Excellent agreement between the analytical and FE calculations can be seen throughout. Regardless of hole size, the mode converted S_0 mode can be seen to be scattered symmetrically about the axis of propagation of the incident plane wave, with almost zero amplitude in the axis of propagation. The reflection ratio changes significantly with hole size both in amplitude and pattern, in general becoming larger and more complex as a function of scattering angle with increasing hole size. Note also that the shape of the scattered RC for the 60 mm diameter hole in (a) is similar as in figure 3.16 (b), which shows the reflection ratio for the SH_0 with a plane S_0 wave incident on the same hole (albeit in a 6 mm thick plate).

The amplitude of the scattered SH_0 mode is generally larger than that of the scattered S_0 mode, partly due to its wavelength being shorter than for the S_0 mode for the frequencies investigated, and also varies more rapidly with angular direction of the scattered wave. As with the mode converted S_0 waves,

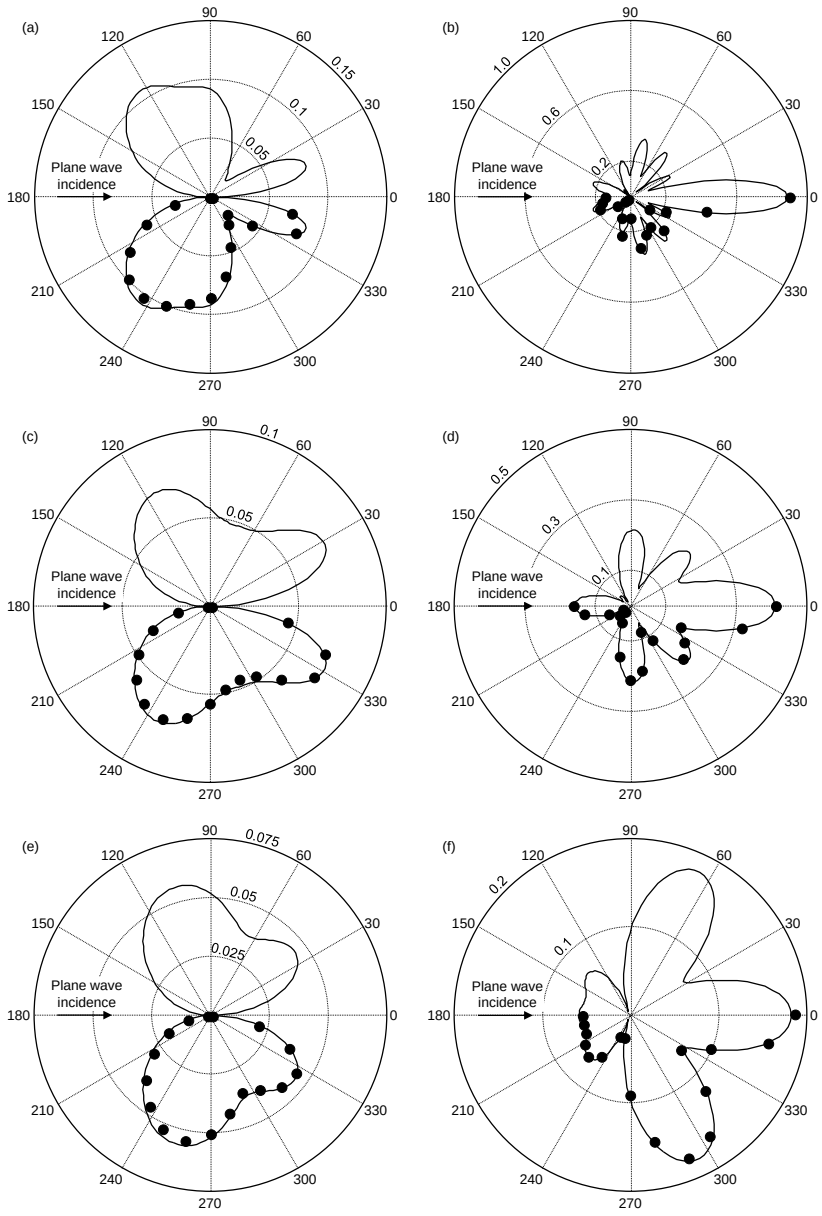

Figure 3.22: Reflection ratio as a function of angle for through-thickness holes at 100 kHz with plane SH_0 wave incidence. Calculated modes and hole diameters are (a) S_0, 60 mm, (b) SH_0, 60 mm, (c) S_0, 30 mm, (b) SH_0, 30 mm, (e) S_0, 15 mm, and (f) SH_0, 15 mm. The radial axis corresponds to the magnitude of the displacement. Solid lines indicate results from the analytical implementation of Cegla et al. [32], markers show FE results.

the scattered SH_0 waves are symmetric about the direction of propagation of the incident plane wave. Increasing the hole size results in larger reflections, which also gets more focused in the direction of transmission with respect to the propagation direction of the incident plane SH_0 wave.

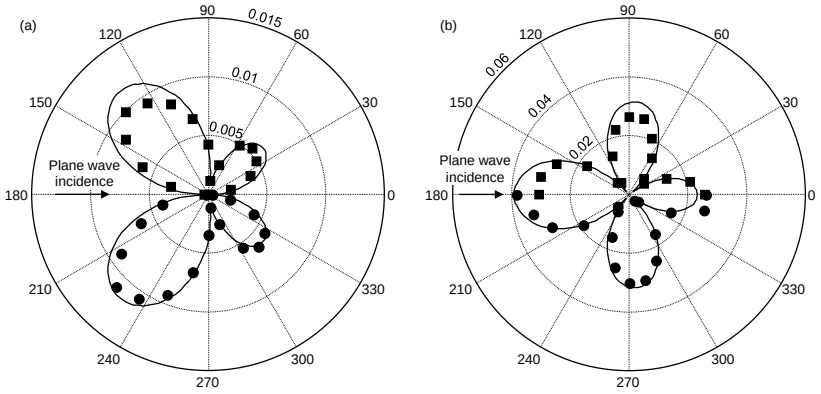

Figure 3.23: Reflection ratio for the scattered S_0 (a) and SH_0 (b) modes as a function of angle for through-thickness holes of diameter 3.75 mm at 100 kHz with plane SH_0 wave incidence. The radial axis corresponds to the magnitude of the displacement. The square and circular markers show FE results with 8 and 16 elements around the hole circumference, respectively, which are compared with the analytical implementation of Cegla et al. [32] (solid lines).

As mentioned in introductory part of this section, 15 elements around the circumference of the hole are necessary in order to model it properly with tetrahedral elements [76], a requirement that was adopted here for the hexahedral elements used in the vicinity of the holes. Figure 3.23 shows the results of similar calculations as presented in figure 3.22, only for a hole of 3.75 mm in diameter. The square and circular markers on the upper and lower half of the figures, respectively, are calculated with 8 and 16 elements around the circumference of the hole, while the solid lines show results calculated using the analytical solution from Cegla et al. [32]. The mesh size is refined locally in the case with 16 elements around the hole circumference, while the mesh size of the plate model in general is kept at 1.5 mm. Thus, a ratio between number of elements around the hole circumference to hole diameter larger than around 4 was required for the hole to be modelled with acceptable accuracy using hexahedral elements. However, note that care must be taken in the use of local mesh refinement, as it can result in severely distorted elements if exaggerated.

A strong angular dependence can be seen in the scattering of both modes, with larger amplitude for the SH0 reflection overall. The efficiency of applying baseline subtraction is evident, especially for the S0 mode, as reflections of very low magnitude can be reliably simulated in ABAQUS. The agreement between

the FE and analytical calculations is significantly improved by applying the local mesh refinement. The approximation made by Cegla et al. [32] in their scattering model by limiting the number of circumferential orders included in the Bessel and Hankel series expansions is more critical with larger defect sizes, as the number of terms needed are dependent on the size of the hole relative to the wavelength. Thus, the analytical solutions can be trusted as correct in this case, and the agreement with the FE results is thought to be limited by the accuracy of the FE calculations.

3.4 Conclusions

The reflection and scattering from infinitely long rectangular notches and circular through-thickness holes in plates are discussed in this chapter. 2D FE models in plain strain were used to predict the reflection of the S_0, A_0 and SH_0 modes from rectangular notches in a 10 mm thick steel plate. The influence of the mode shapes of the modes on the reflection coefficient was illustrated; for the more simplistic mode shapes of the S_0 and SH_0 modes at the evaluation frequency of 50 kHz RCs varied relatively linearly as a function of notch depth, while the more complex mode shape of the A_0 mode gave rise to a more complex reflection behaviour as a function of notch depth. Results were in agreement with similar earlier work published other researchers [11, 28–30].

In validating the 3D FE model of the steel plate, the work of Diligent et al. [31] on the reflection of the S_0 Lamb mode from a through-thickness hole with plane wave incidence was used to evaluate the RC as a function of distance from a circular hole, while an analytical implementation by Cegla et al. [32] was used for the scattering as a function of angle for various hole sizes. Excellent agreement was obtained throughout. The RCs decay with increasing distance to the hole in a manner inversely proportional to the square root of distance, and with decreasing hole size. The RC can be normalised to the hole diameter at a given frequency. Some influence of secondary effects such as creeping waves and influence of SH_0 waves were seen. The scattered S_0 and mode converted SH_0 modes were found to be a strong function of scattering angle.

Similar results were found with a plane SH_0 wave incident on a through-thickness hole; the RC decreased with increasing distance from the hole, and with decreasing hole size in general. However, the influence of creeping waves was found to be stronger with plane SH_0 incidence, and the creeping waves could not be separated in time from the directly scattered reflection for holes smaller than a certain size, which is dependent on the scattering direction. Since the creeping waves propagate at the same velocity as the directly scattered reflection, their separation in time is constant, thus not dependent on distance from the hole at which the RC is obtained.

The scattering pattern of both the S_0 and the SH_0 modes with plane SH_0 incidence was highly dependent on the scattering angle, symmetric about the plane of propagation of the incident plane wave, and with larger amplitude of

the scattered SH_0 wave compared with the mode converted S_0 waves in general. For small diameter holes, local mesh refinement can be applied to improve the accuracy of the FE model with limited expense in calculation time. With hexahedral elements, the ratio between the number of elements around the hole circumference to the hole diameter should be larger than approximately 4 in order to achieve acceptable model accuracy.

Chapter 4

The reflection of the fundamental torsional guided wave from multiple circular holes in pipes

A study of the reflection from two and three small circular holes in pipes with the fundamental torsional guided wave incident is presented in this chapter. FE analyses with both part- and through thickness holes at different relative positions are discussed, and the applicability limits of employing a superposition technique in doing so are assessed.

An introduction to guided waves in pipes and the geometrical properties of typical localised corrosion attacks are given in Section 4.1. The characteristics and properties of the modes investigated are discussed in Section 4.2, while FE analyses of the reflection from two and three circular holes separated circumferentially, axially, and at intermediate angles are presented in Section 4.3. The main results from the FE modelling are validated experimentally in Section 4.4, before conclusions are drawn in Section 4.5.

4.1 Introduction

Ultrasonic guided wave testing and screening for corrosion or other defects in plates, pipelines, railways and other structures is used increasingly, especially for pipelines in the petrochemical industry. One of the main advantages of guided wave techniques is that they enable long-range screening of pipelines, in contrast to traditional ultrasonic testing where the coverage is limited to a small area in the vicinity of each transducer. Also, lengths of pipelines may be buried, coated, or in other ways practically inaccessible, none of which necessarily limits the applicability of guided waves as they can propagate in the pipe material itself with minimal attenuation. The possible cost reduction by applying guided waves for inspection of pipelines is therefore significant.

Certain boundary conditions (e.g. types of coatings) give higher attenuation of guided waves, but with appropriate choice of guided wave parameters the test range and accuracy can be optimised [52, 79, 94].

The current trend in the offshore petroleum industry is to move operational activities to harsher environments with higher pressure, temperatures and depth. In addition, economic moves towards multi-phase transportation through subsea completions and use of long infield pipelines all increase the risk of corrosion [1]. The majority of oilfield corrosion failure results from CO_2 (sweet) corrosion of carbon and low alloy steels [95]. However, as oilfields are being depleted, the number of sour (H_2S) oil and gas fields increase. Production and transport in sour environments always implies a risk of shutdown due to CO_2/H_2S corrosion, and especially localised corrosion. Localised attacks involve corrosion at discrete sites, such as pitting, pit clusters, mesa corrosion, crevice corrosion and stress corrosion cracking [2]. Most of the internal corrosion of oil and gas pipelines is in the form of localised attack, with surrounding areas essentially unaffected or subject to general corrosion only [96]. Figure 4.1 shows an example of a corroded pipe segment, where several deep pits have grown in areas otherwise affected by general corrosion only.

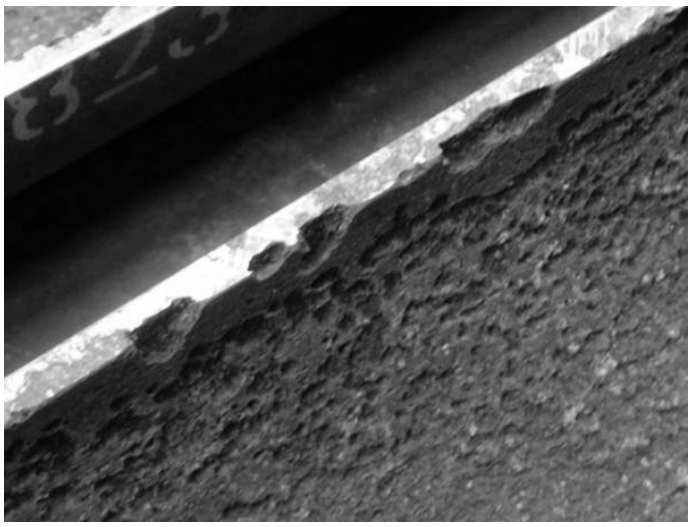

Figure 4.1: Severely corroded pipe, where pits are growing out of areas of essentially affected by general corrosion only.

Though ultrasonic guided wave testing has a higher chance of detecting localised corrosion compared to traditional ultrasonic testing due to its increased coverage, the sizing of the defects will be less accurate as the transducers will be at a distance. The detection limit using guided waves will to some extent depend on the geometry of the attack. Pits can take various geometrical shapes,

usually with tapered and smooth sides, which often can be approximated by a circular or elliptical shape, with a large range of possible width and depth. Pit clusters are groups of pits, either grown together or adjacent to each other. Mesa corrosion is typical of sweet environments, and forms deep and often flat-bottomed defects with very sharp vertical sides [2, 96, 97]. Pitting caused by internal sour corrosion in pipelines usually results in large, wide pits and pit clusters. The attack can develop around one or two initiation sites and then merge to larger and wider defect regions [2]. Codaro et al. [98] reported single pit depth growth to be equal to, or somewhat larger than its surface diameter growth, depending on the shape of the pit at the surface. Nyborg [97] reported a growth rate in depth of localised corrosion in the form of mesa attacks to be in the same range or shallower than the lateral growth rate. This means that we can expect corrosion geometries ranging from wide and shallow attack due to uniform corrosion, to pits with diameter and depth of the same order.

Localised corrosion defects are difficult to detect using traditional ultrasonic testing, requiring the use of an internal probe running through the pipe, detailed c-scan, or the use of guided waves. Applying guided waves not only for defect screening, but also for defect sizing is very desirable, but requires detailed knowledge about the interaction of the incident wave with different possible defect types in order to interpret the reflections from them correctly. Practical long range screening of pipes using cylindrical guided waves typically aims to detect corrosion defects of the order of 5-10% of the cross-sectional area at a given axial distance, and is designed to operate on pipes in the 2-24 in. diameter range [7], though this range can be extended. Demma et al. [11] did a parametric study of the reflection of the fundamental torsional guided wave from notches in pipes, finding removal of cross-sectional area of about 2% is what can be expected to be detected in a relatively clean pipe, though this can be improved by focusing [12, 13].

The purpose of this study is to investigate the reflection from two and three small circular holes in a pipe, and assess the applicability limits of employing a superposition technique in doing so. As localised corrosion often occurs in clusters, the reflection from two and three circular holes will be a step towards understanding the scattering behaviour of multiple and randomly spaced defects. As a large percentage of corrosion failures in the oil and gas industry originate from localised defects in carbon and low-alloy steels due to their poor general and CO_2 corrosion performance [1], an increased understanding of the scattering behaviour of localised corrosion will help reduce this failure rate.

With a lower typical diameter to depth ratio of 1:1 for defects due to localised corrosion established, circular holes of diameter $1t$ are used throughout this chapter, where t is the pipe wall thickness. Using pipes with 3 in. outer diameter (76.2 mm) and 5.5 mm wall thickness, this corresponds to a diameter of the hole of 5.5 mm, which is roughly a cross-sectional extent of 2.5%. For a 24 in. pipe, the same hole corresponds to a cross-sectional extent of only 0.3%, and is thus much harder to detect, unless focusing is employed.

Many researchers have investigated the scattering and reflection from a variety of defects using guided waves, both in plates [22, 24, 26, 28, 30–32, 79, 84–87] and pipes [7, 11, 15, 17, 18, 23, 49, 53]. Types of defects include cracks [22, 23, 30], notches [11, 15, 17, 49, 53, 79], circular holes [24, 31, 84] and elliptical defects [26]. The scattering of antiplane shear waves from an infinite circular cylinder in an infinite plate have been investigated analytically by Wang et al. [99] in 2D. Grahn [24] presented a model for guided wave scattering of the S_0, A_0 and SH_0 modes from part-thickness circular holes with S_0 incidence, thus including mode conversion. Diligent and Lowe studied low-frequency scattering of the S_0 Lamb mode from both a through [31]- and part [84]-thickness hole in a plate using an analytical modal superposition method, comparing analytical, finite element (FE) and experimental results; the results reported for a through-thickness hole [31] were used to validate the plate FE model in Section 3.3. As was the recent study by Cegla et al. [32], which extended the model by Grahn using approximate plate wave theories to lower the computation time.

Modes discussed in this study are labelled according to the convention of Silk and Bainton [48] as longitudinal (L(0,n)), flexural (F(m,n)) and torsional (T(0,n)), where m gives the harmonic order of circumferential variation and n is a counter variable, as explained in more detail in Section 2.2. In pipes the fundamental torsional mode T(0,1) and longitudinal modes L(0,1) and L(0,2) are commonly used modes for practical inspection, T(0,1) being most often used. Demma et al. [11, 15] studied the reflection from cracks and notches in pipes, while Carandente et al. [17] assessed the effect of tapered notches, both using the fundamental torsional mode. Hayashi and Murase [51] used a defect imaging technique to identify one and two circular holes in pipes using the T(0,1) mode. Davies and Cawley [12] presented work on defect imaging using synthetically focused imaging techniques for high resolution guided wave pipe inspection. They specifically investigated small cracks, but the method is also applicable for other defect shapes.

Much work has been done to solve the problem of the scattering of bulk waves from multiple inhomogeneities involving spherical and elliptical voids or cracks. Gubernatis et al. [63] used the Born approximation to look at the scattering from spherical voids with both longitudinal and transverse waves, finding that it is applicable at low frequencies, $ka \ll 1$, where k is the wavenumber and a the characteristic dimension of the voids. Following the work of Gubernatis, Domany et al. [100] presented a method based on an expansion of the T-matrix approach to calculate the scattering from two spherical cavities. They studied longitudinal to longitudinal scattering from two spherical voids of radius a at separation distance $3a$ for $ka = 1$ and 2 for different incidence and scattering angles, and concluded that even for strong scatterers this closely spaced, the coherent sum of the two independent scattered reflections when interaction terms are neglected gives a good approximation. Schafbuch et al. [64] did a similar study assessing scattering from spherical and oblate spheroidal voids using

both generalised Born series and far-field approximations, and found similar validity of approximations as a function of separation distance. Grøvlen et al. [101] found using notch theory and fracture mechanics that stress interaction between corrosion pits was negligible if the edge to edge distance between them was larger than their average diameters. If the separation is less than this, they should be regarded as one elongated pit with depth equal to the deepest pit. A parametric study of the validity of employing the superposition technique in calculating reflection coefficients (RCs) as a function of defect separation and orientation is presented in this chapter, assessing the error inferred by neglecting defect interaction by comparing with the full solution.

4.2 Mode characteristics and frequency range

Selection of excitation mode and frequency range is essential for successful use of guided waves in ultrasonic inspection and defect sizing. Properties governing propagation and interaction with defects are very complicated, so excitation and monitoring parameters must be chosen with care. Dispersion curves are an essential tool to optimise mode and frequency for defect sizing, the effects of which are discussed by Wilcox et al. [50]. Figure 4.2 shows the group velocity dispersion curves of pipes with 3 in. (76.2 mm) outer diameter and 5.5 mm wall thickness that are used throughout the simulations in Section 4.3.

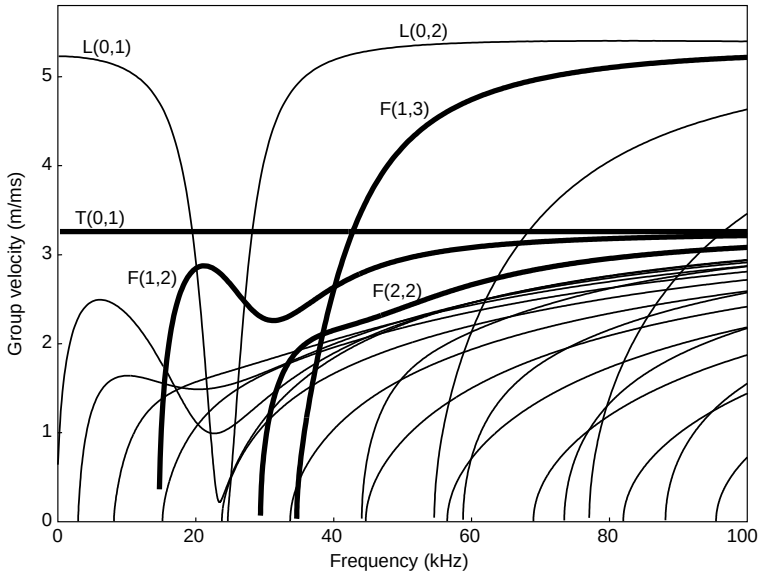

Figure 4.2: Group velocity dispersion curves for 3 in. schedule 40 pipe. Modes of interest are shown in bold.

The dispersion curves are calculated using DISPERSE v2.0 [44], developed at Imperial College, London, and show the group velocity of propagation as a function of frequency for all modes present within the given frequency range. Modes discussed in this study are shown in bold.

Recently, most practical testing has been done with the fundamental torsional mode, T(0,1), as it is completely non-dispersive at all frequencies, in addition to being axisymmetric, which makes it easier to excite and receive. Another appealing property of the T(0,1) mode is that it is not affected by liquid present in- or outside the pipe. Keeping the bandwidth of the excitation signal below cut-off of the T(0,2) mode makes it relatively easy to obtain a pure single mode excitation.

As mentioned in Section 4.1, the diameter of the individual defects investigated throughout this chapter is equal to the wall thickness, $a = t$. The scattering from individual defects is often divided into three regimes using the parameter ka, where k is the wave number given by $k = 2\pi/\lambda$ and a is the characteristic dimension of the defect [61]. Thus, for the T(0,1) mode, k is simply a linear function of frequency, as the phase velocity is constant. For low frequencies, where $ka < 0.1$, a quasistatic approach or the Born approximation may be employed, while high frequency approximations such as the Kirchhoff approximation or geometrical diffraction theory can be considered for $ka > 1$. For an excellent review of different approximations and analytical approaches, see Rajagopal [71], while Schmerr et al. [72] give a good review and comparison of model based methods in defect sizing. However, in the intermediate regime $0.1 < ka < 1$, when the dimensions of the scatterers are comparable to the incident wavelength, numerical methods such as finite elements (FE), boundary elements (BE) or finite difference (FD) are appealing. These limits of scattering regimes correspond to 9 kHz $< f <$ 94 kHz with the given defect dimension of $a = t = 5.5$ mm, which includes practical inspection frequencies, as shown in figure 4.2.

When multiple defects are present, the total reflection and scattering patterns are given not only by the individual scatterers, but also by the interference and interaction between them. In this chapter, the validity of a superposition approach will be investigated to assess the degree to which interaction between multiple scatterers influences the total reflection as a function of separation distance and position around the pipe circumference. Both the separation between defects and the characteristic dimension a of the defects will affect the reflection coefficient (RC) and must be accounted for. Accordingly, the parameter used will be the ratio L/λ, where L denotes the axial distance from centre to centre between defects and λ the wavelength of the propagating guided wave mode investigated. For circumferentially spaced defects, results will be displayed as a function of separation angle around the circumference. a is kept constant at $a = t$, as mentioned earlier.

Demma et al. [15] were the first to report on the mode conversion from defects (cracks and notches) with T(0,1) incidence, following the method de-

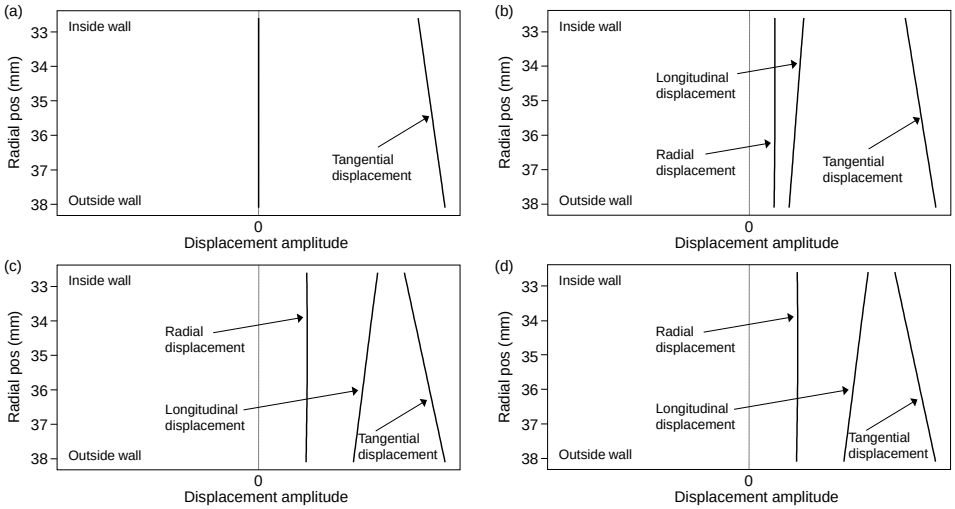

Figure 4.3: Displacement mode shapes in a 3 in. schedule 40 pipe at 60 kHz for (a) T(0,1), (b) F(1,2), (c) F(1,3) and (d) F(2,2) modes.

scribed in Lowe et al. [49] for L(0,2) incidence. Figure 4.3 (a)–(d) show the mode shapes at 60 kHz of T(0,1), F(1,2), F(1,3) and F(2,2), respectively, which is the chosen centre frequency for the simulations in the present study. As the defects in this study are non-axisymmetric, mode conversion into both axisymmetric and non-axisymmetric modes can occur. The extent of mode conversion, in this case from the incident T(0,1) mode, can be explained via the mode shapes, which give the amplitudes of radial, axial and tangential particle motion through the pipe wall thickness, and are frequency dependent. The higher the similarities in particle motion between the modes, the stronger the mode conversion. The T(0,1) mode has only tangential displacement at all frequencies, as can be seen in figure 4.3 (a) at 60 kHz, so the extent to which other modes are generated through mode conversion from T(0,1) is governed by the extent of tangential motion in the other modes. Both F(1,2) and F(2,2) have dominant tangential displacement, so the mode conversion will be strong, especially for F(1,2). F(1,3) has dominant longitudinal displacement, and will thus appear with lower amplitude in the mode converted reflections.

4.3 Finite element predictions

Modelling using the finite element method has been extensively and successfully used to model guided ultrasonic waves and their interaction with various defects in plates [26, 28, 30, 31, 84, 86], pipes [7, 11, 17, 18, 20, 23, 49, 53] and other structures [102, 103]. Full 3D models in the commercially available

software ABAQUS version 6.9 [74] are employed throughout the simulations in this section; all FE modelling in this section is done on a 3 meter long pipe with 3 in. outer diameter and 5.5 mm wall thickness. A 4 cycle Hanning windowed toneburst with centre frequency of 60 kHz was used, giving a ±10 dB bandwidth of roughly 40–80 kHz. Quadratic tetrahedral elements with element length of 4 mm were chosen, giving an approximate nodal separation of 2 mm. With a diameter of the individual circular holes of only 5.5 mm, the nodal separations at the defect edges were refined and set to 1.5 mm around the defect circumference, to avoid possible problems with convergence due to the automatically generated mesh. A time step of 50 ns was used. Convergence tests were run to ensure that the mesh size and time steps were appropriate. Figure 4.4 shows the RC as a function of frequency for a single through-thickness hole calculated using FE (solid lines) at varying positions in the pipe (40 positions included); the position of holes and monitoring positions where chosen such that the incident and reflected signals were well separated. The relative variation in the RCs from the single holes was less than ±3% at all frequencies within the ±10 dB bandwidth from 40–80 kHz, and less than ±2% around the centre frequency.

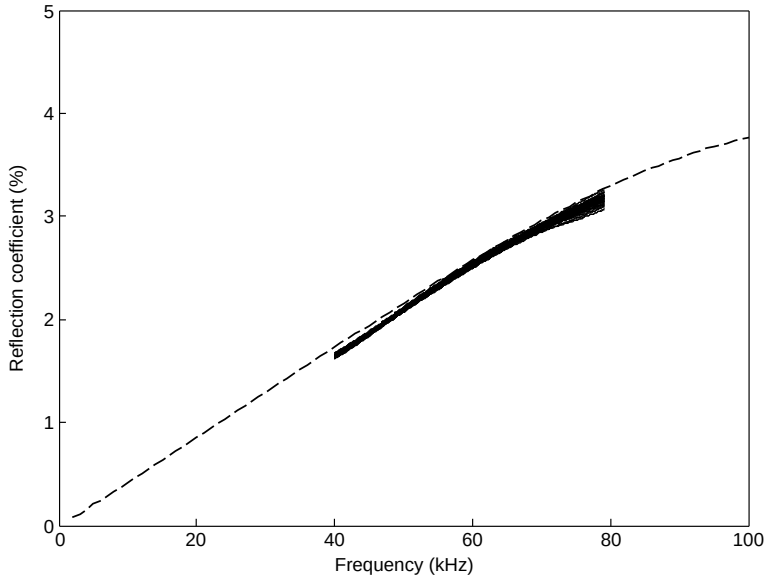

Figure 4.4: Validation of FE model (solid lines) against analytical solution (dashed line).

Additionally, the model was validated against the analytical solution, which is indicated by the dashed line in figure 4.4. The reflection coefficient in the specular direction from a 5.5 mm diameter through-thickness hole in a plate

with plane shear horizontal wave incidence was calculated using Poisson theory, as explained in Cegla et al. [32], and discussed in Chapter 3. As explained in Section 2.4, if the radius of a pipe is much larger than its wall thickness, the pipe can be considered as an unwrapped isotropic plate [60]. The fundamental shear horizontal mode in a plate, SH_0, is then equivalent to the fundamental torsional mode in a pipe, T(0,1). Velichko et al. [27] provides a detailed discussion on the theoretical background and limitations of the approximations done in order to convert reflection coefficients in a plate to the corresponding RCs in a pipe, and vice versa, the results of which are summarised in Section 2.4. Their method requires the pipe wall thickness to be much less than the pipe radius, i.e. $t \ll r$. In the 3 in. 40 schedule pipe, $r \approx 8t$. The RC from the finite element analysis was found to be 2.5% at 60 kHz and within 5% relative to the analytical calculation over the ± 10 dB bandwidth, thus validating the model within acceptable accuracy.

Defect layouts modelled are shown schematically in figure 4.5 for the case of two through-thickness circular holes separated (a) circumferentially, (b) axially, and (c) at other relative positions. The arrows indicate the way in which defect separation was varied, i.e. with φ in (a), and with L in (b) and (c), where the angle θ is fixed in (c). Most of the simulations will be compared with results obtained using the superposition principle, where separate simulations were performed with one defect at a time at the appropriate location, the reflected signals being subsequently added together directly, thus also evaluating the uncertainty in the numerical predictions. In subsequent chapters superposition will be calculated by modelling single defects, and adding the reflections from the given number of defects together simply by adding the appropriate phase delay depending on the position of each defect. Using the superposition approach implicitly neglects interaction between the defects, the validity of which will be assessed throughout this chapter.

The T(0,1) mode was excited by applying the excitation toneburst as tangential displacements at 90 evenly spaced nodes around the outer circumference at one end of the pipe, as indicated in figure 4.5. Similarly, 90 monitoring points were chosen at a distance of 0.95 meters from the excitation end. Throughout the remaining part of this thesis, signals were calculated in the time domain by adding the tangential components, $u_{\tan}$, given by

$$u_{\tan} = u_x \cos\varphi - u_y \sin\varphi, \tag{4.1}$$

in each of the 90 monitoring points together, where u_x and u_y are displacement components in a right hand coordinate system where z is the direction of propagation, with reference to figure 4.5. The different defect layouts were introduced at a further distance of 1.0 m from the receiver points, at a distance of 1.05 m from the right hand end. These distances were chosen so that the F(1,2) and F(1,3) modes could be separated in time for circumferentially spaced defects, and similarly F(2,2) will be separated from F(2,1) and F(2,3), for the larger part of the frequency range used.

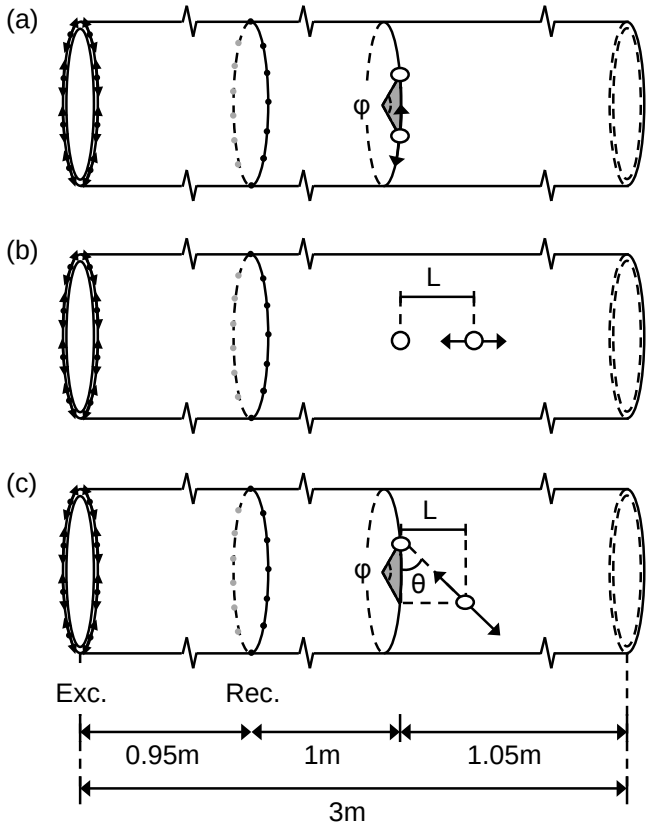

Figure 4.5: Schematic of (a) circumferentially separated defects, (b) axially separated defects, and (c) defects separated by angles φ and θ. Excitation applied in circumferential direction at each node at the left hand end of the pipe; reception in circumferential direction at each node around the receiver location.

By prescribing tangential displacements, the L(0,1) and L(0,2) modes were not excited, and pure T(0,1) excitation was achieved. Figure 4.6 shows a typical time record from two circumferentially spaced defects after summation of the received signals at all monitoring nodes, where (a) and (b) show T(0,1) and F(1,n), respectively. m^{th} order modes were extracted by adding $m\varphi/2\eta$ to each monitoring point around the pipe circumference, where φ is the angular distance from a defined principal axis at $\varphi = 0$, and subsequently summing them, as described in Lowe et al. [49, 53]. This processing was performed in the frequency domain, and then converted to the time domain. With a bandwidth from 40–80 kHz, the highly dispersive part of F(1,3) down to its cut-off is included, as can be seen from figure 4.2. Thus the low frequency content of

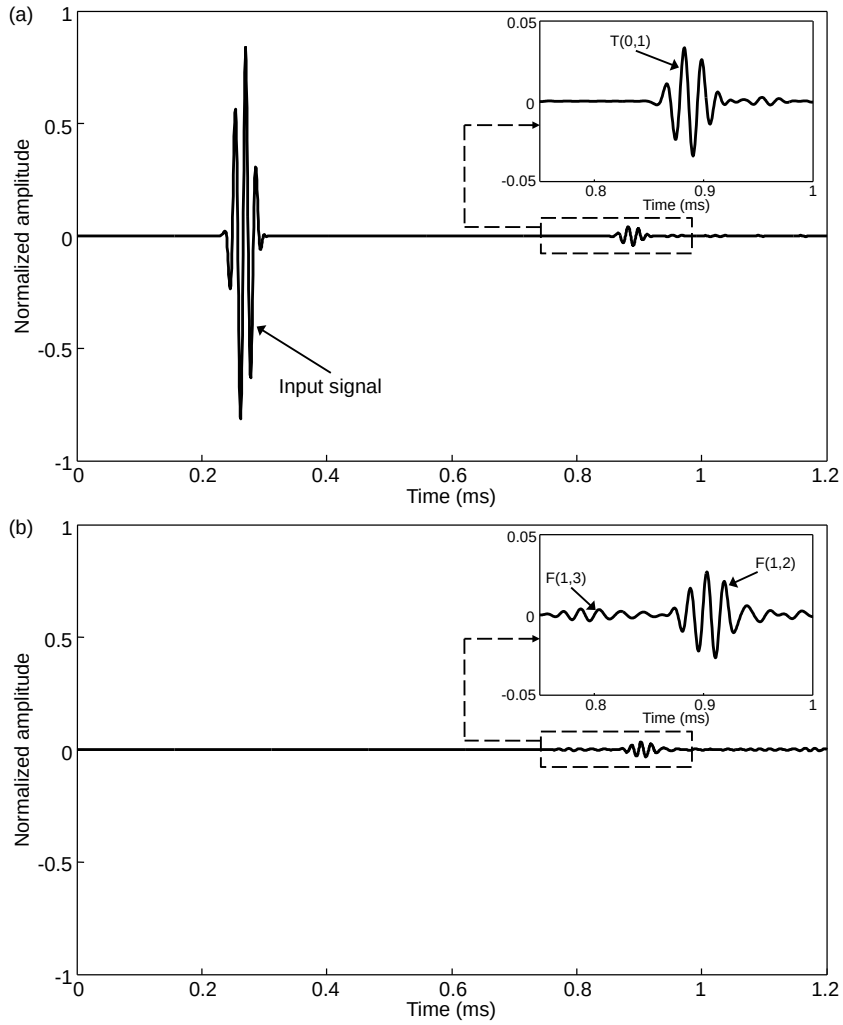

Figure 4.6: Typical time record from finite element calculations, with processing to extract (a) order 0 modes, and (b) order 1 modes.

F(1,3) does not separate from F(1,2). However, first order modes will only be investigated at 60 kHz, where mode separation is achieved. Similar considerations apply for F(2,2), with respect to F(2,1) and F(2,3). The amplitudes of the different modes also give an indication of the mode conversion of the signals. The F(1,n) mode signal of figure 4.6 (b) shows no input signal, indicating that the excitation signal is pure T(0,1), as expected.

Reflection coefficients were calculated in the frequency domain throughout this chapter, and are defined as the ratio of the surface circumferential displace-

ment amplitude of the reflection in the particular mode to that of the incident T(0,1) mode.

Through-thickness circular holes

Cases with defects separated circumferentially, axially, and at angles of $\theta =$ 20, 45 and 60° were modelled, as shown in figure 4.5 (a), (b) and (c), respectively. Circumferentially and axially spaced defects are commonly encountered in practical cases, due to inhomogeneities or specifically vulnerable areas of a structure such as welds [104, 105] or at the bottom (6 o'clock position) [96] of pipes.

Circumferentially spaced holes

Figure 4.7 shows reflection coefficients for the T(0,1), F(1,2), F(1,3) and F(2,2) modes at 60 kHz as a function of the angular distance φ between them for two circumferentially spaced holes. The figure insets shows the cross-section at the axial position of the holes for through- (•) and part-thickness (▼) holes. Full solution results are shown in solid lines, where results with through-thickness holes are marked with solid circles, while the 50% depth cases, which will be discussed in a later subsection, are indicated by solid triangles. All results obtained using superposition are shown in dashed lines.

The angular distance between the centres of two holes just contacting each other is given by

$$\varphi_{\text{cont}} = \frac{a}{r_{\text{inner}}} \frac{180}{\pi}, \tag{4.2}$$

where a is the hole diameter and r_{inner} is the inner radius of the pipe. In this case $\varphi_{\text{cont}} = 9.7°$, while the minimum angle modelled is $\varphi = 11°$, corresponding to a minimum separation distance of $1.15a$; smaller separation between them would lead to highly distorted meshes, and result in numerical problems.

The reflection coefficient for the T(0,1) mode is approximately 5% for all angular separations, except for angles lower than around $\varphi = 20°$, corresponding to an angular separation of two diameters centre to centre. The small oscillation of the results relative to the superposition results at angles above 20° is due to constructive and destructive interference between the main reflected signal and the scattering from one defect interacting with the second defect and then scattering back to the receivers. The RC with three circumferentially spaced holes is omitted in figure 4.7, but is approximately 7.5%, and relatively independent of circumferential position of the holes unless they are situated at angular distances below 20° in between them. A RC of 2.5, 5 and 7.5% for the one, two and three hole case, respectively, confirms the validity of superposition, and that the RC is a linear function of the total circumferential extent of the defects.

A small oscillation in the superposition results for the T(0,1) mode can be seen; this is due to a variation of up to ±2% in the amplitude of the reflection

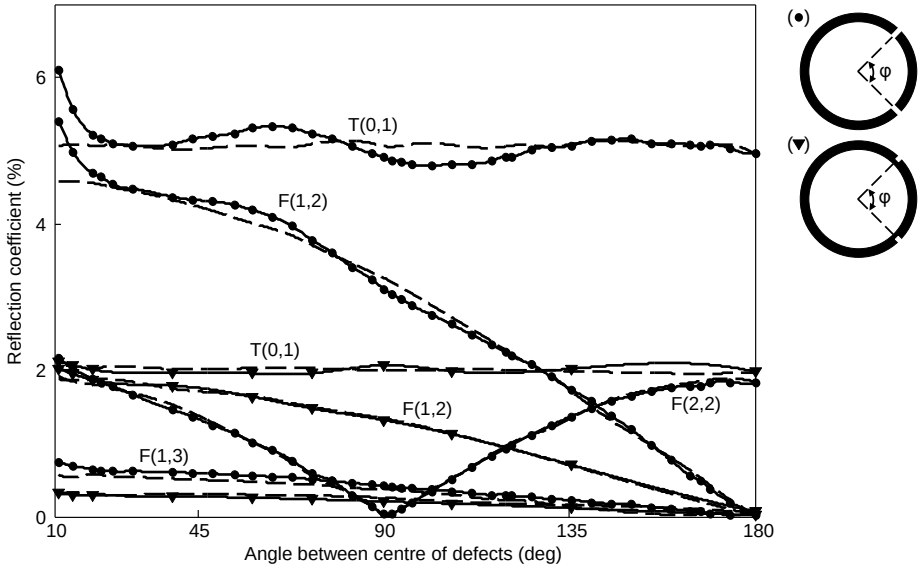

Figure 4.7: Variation of RC with angle between two circumferentially spaced circular holes of diameter $a = t$ at 60 kHz with the T(0,1) mode incident. Results with holes of 50 and 100% depth are indicated with solid triangles and circles, respectively, while superposition results are shown in dashed lines. The insets show the cross-section at the axial position of the holes for through- (•) and part-thickness (▼) holes, respectively.

from holes at different circumferential locations, as seen in figure 4.4. This numerical error indicates the likely magnitude of the error that will be present in future superposition calculations in which the reflection from multiple defects is predicted simply by adding the results from a single hole with appropriate phase shifts. The reflections of the F(1,n) and F(2,n) modes show maxima approaching zero angular separation and minima at 180° and 90°, respectively. This behaviour is similar to that observed with circumferential notches [15, 49].

Figure 4.8 shows the RC for the T(0,1) mode as a function of frequency over the ±10 dB bandwidth for a single circular hole (a), two (b) and three (c) circumferentially spaced through-thickness circular holes (as well as for two circumferentially spaced holes of 50% depth (d)), all of diameter $a = t$; the figure insets show a cross-section of the hole layout and variation for illustrating cases (a)–(d). Results shown in (b) include angular separations in the range from $\varphi = 11 - 180°$. RCs for 38 different angular separations in the interval $\varphi = 19 - 180°$ are contained within the hatched area between the dashed lines. The two solid lines within (b) above the upper dashed line are RCs from defects at angular distances of 11° and 14°, which correspond to centre

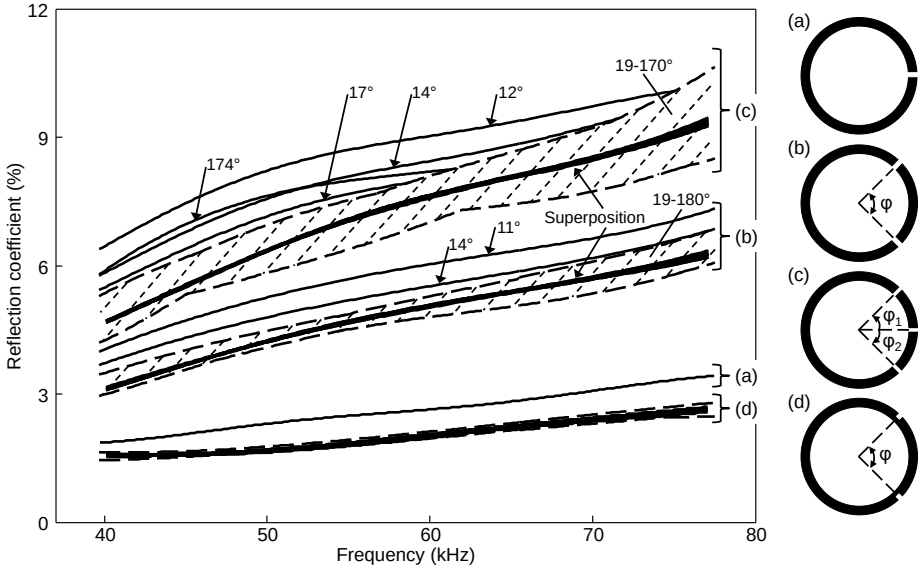

Figure 4.8: Variation of RC for the T(0,1) mode with frequency for circular holes of diameter $a = t$, (a) a single through-thickness hole, (b) two through-thickness circumferentially spaced holes, (c) three through-thickness circumferentially spaced holes, and (d) two circumferentially spaced holes at 50% depth with the T(0,1) mode incident.

to centre distances of $1.15a$ and $1.5a$, respectively. A similar trend can be seen from curves (c) showing T(0,1) RCs as a function of frequency for three circumferentially spaced holes, where RCs for angular separations in the interval $\varphi_1 = \varphi_2 = 19 - 170°$ (see inset (c)) are contained within the hatched area. The solid lines within (c) above the upper dashed line show RCs from defects at angular distances of $\varphi = 12, 14, 17$ and $174°$, i.e. where the defects were situated close together.

Results from superposition calculations for the same angular separations from $\varphi = 11 - 180°$ are shown as solid lines within the hatched area in (b), and equally from $\varphi_1 = \varphi_2 = 11 - 170°$ in (c). The RCs obtained using superposition should be independent of angle; this is seen in figure 4.8 apart from some deviation at higher frequencies due to numerical errors arising from the relatively coarse mesh. For angular separations above 19° between defects (corresponding to centre to centre separations greater than $2a$), the error in the superposition calculations is less than ±8% (two holes) and ±11% (three holes) at all frequencies, with the largest variation at the extremes of the frequency bandwidth. In general, the RCs can be seen to be an almost linear function of frequency within the frequency range.

Axially spaced holes

With circumferentially spaced defects, reflections from the defects will arrive at the same time because they travel the same distance with respect to the receiver positions. Axially spaced defects on the other hand will arrive at different times, giving rise to interference effects. Figure 4.9 shows the RC for the T(0,1) and F(1,2) modes at 60 kHz with T(0,1) incidence as a function of the ratio L/λ, where L is the separation distance from centre to centre of the two circular holes, as shown in the figure inset. T(0,1) and F(1,2) are indicated by solid triangles and circles, respectively, while the corresponding superposition results are shown in dashed and dash-dotted lines. The RC of both modes can be seen to be strongly dependent on the separation distance, maxima occurring at $L/\lambda = \eta/2$ and minima at $L/\lambda = (2\eta - 1)/4$, where η is an integer. This differs from single defect cases, as multiple defects represent successive decreases in impedance whereas single defects give a decrease in impedance at the start of the defect followed by an increase at the end. Therefore maxima occur at multiples of $L/\lambda = (2\eta - 1)/4$ with single defects, as is found for steps and notches in plates with SH_0 mode incidence [30] as well as with L(0,2) [7] and T(0,1) [15, 17] mode incidence in pipes.

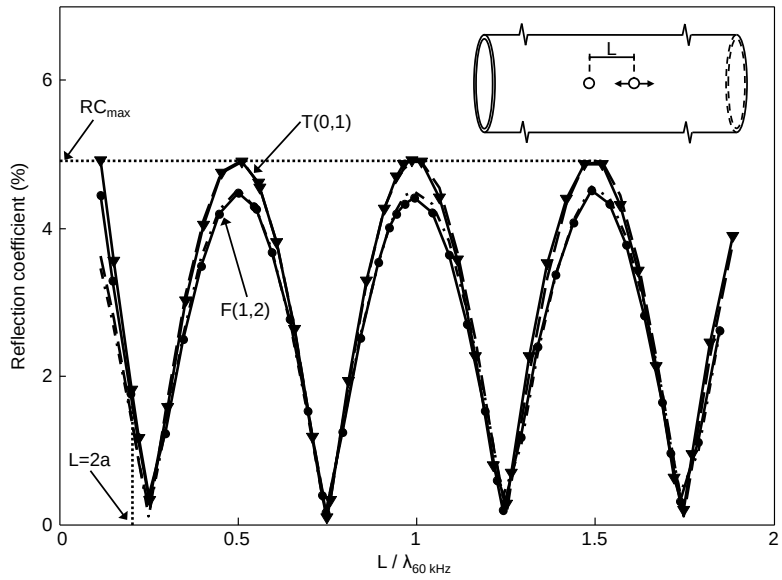

Figure 4.9: Variation of RC at 60 kHz with axial separation for two through-thickness circular holes of diameter $a = t$ with the T(0,1) mode incident. The T(0,1) and F(1,2) reflected modes are indicated by (▾) and (•), while the corresponding superposition results are shown in dashed and dash-dotted lines, respectively.

Excellent agreement is found between simulations with the full solution and superposition. As in the circumferential case, the RC deviates noticeably from the superposition RCs when $L < 2a$. The maximum reflection coefficient, $\mathrm{RC}_{\max}$, for the T(0,1) mode is approximately 5%, which is comparable to that for circumferentially spaced defects. Simulation series with three axially spaced defects are omitted in the figure, but show that $\mathrm{RC}_{\max}$ at 60 kHz is 7.5% and occurs when all defects are separated individually by $\eta\lambda/2$ axially. Accordingly, provided that the excited frequency range is sufficient to ensure that at least one maximum is seen, the highest measured RC will be the same as in the circumferential case. The mode converted RC of the F(1,2) mode can be seen to be similar to the T(0,1) mode RC, which is due to the small circumferential extent of the axially aligned defects, in addition to the T(0,1) and F(1,2) mode shapes both being dominated by tangential motion, as can be seen from figure 4.3 (a) and (b).

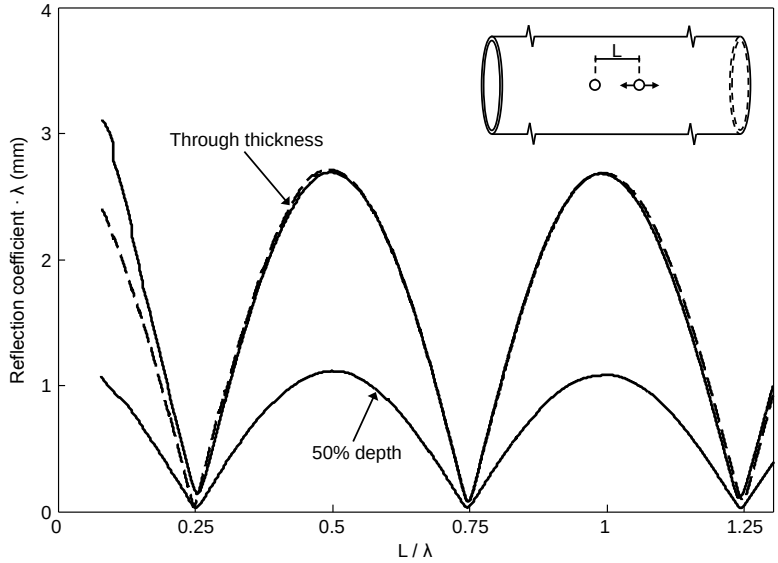

Figure 4.10: Variation of the T(0,1) mode RC multiplied by wavelength product with axial separation for two through-thickness circular holes of diameter $a = t$ with the T(0,1) mode incident. The solid and dashed lines for through-thickness holes show results with full analysis and using superposition, respectively. Only results with full analysis are included for 50% defect depth.

As is evident from figure 4.8, the RC is a roughly linear function of absolute frequency. Therefore, multiplying the RC by the wavelength removes its dependence on absolute frequency. RCs for axially spaced circular holes with L from $1.15a$ (lower limit to avoid excessive mesh distortion) upwards in steps

of $0.25a$ were calculated. Figure 4.10 shows the average of these RCs multiplied by wavelength within the ± 10 dB range in excitation amplitude, with the full solution (solid lines) and with superposition (dashed lines) for through-thickness defects. Calculated RCs varied up to $\pm 3\%$ about these averages due to numerical error and the time gating window employed in post processing the data. Results with the full solution are also shown for defects of 50% depth, which will be discussed in the subsection concerning part-thickness defects below. Results with the full solution and using the superposition approach can be seen to be comparable except when $L < 2a$ (corresponding to the region below $L/\lambda < 0.25$ in the figure), below which multiple scattering between the defects affects the RC. The minor deviations seen above $L/\lambda = 0.25$ are due to numerical errors in the simulations. This validity range of the superposition approach is similar to the results found for circumferentially spaced through-thickness holes. Maxima of the product of RCs and wavelength can be seen to occur at $L/\lambda = \eta/2$, and minima occur at $L/\lambda = (2\eta - 1)/4$. The successive RC maxima are comparable, and are governed by the hole sizes.

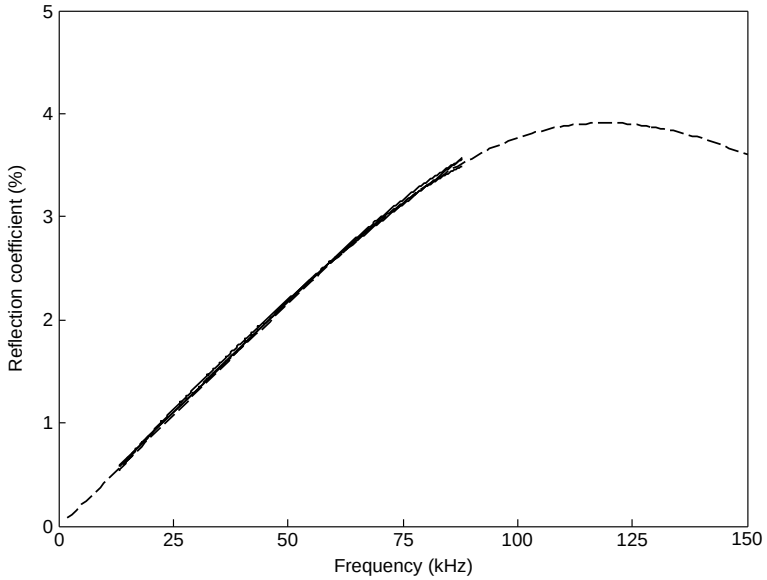

Figure 4.11: Validation of FE model (solid lines) of a single through-thickness hole of diameter 5.5 mm against analytical solution (dashed line). FE model refined to 2 mm quadratic tetrahedral elements.

In practical measurements with more complex defects of unknown shape, the first or the maximum peak RC for the T(0,1) mode are commonly used parameters. Defects of a certain size and/or separation are required for peaks to be within the practical testing frequency range. Figure 4.11 shows the RC

as a function of frequency for a single through-thickness hole of diameter 5.5 mm as employed throughout this chapter. The first peak RC can be calculated analytically [27, 32] to occur at around 120 kHz, as shown by the dashed line in the figure, thus well above commonly used testing frequencies. However, with axial separation of the defects, interaction between the defects gives rise to peaks in the RC at lower frequencies than the peaks related to a single hole. To ensure that these peaks would be within the interrogating signal, the ±10 dB bandwidth was extended to roughly 10–90 kHz by exciting a 2 cycle Hanning windowed toneburst with a centre frequency of 60 kHz in all FE simulations in the remainer of this subsection. The quadratic tetrahedral elements were refined to 2 mm to obtain convergence in the FE analyses. The solid lines in figure 4.11 show the RCs calculated for three different positions of the single 5.5 mm diameter hole using FE. The agreement with the analytical solution can be seen to be excellent throughout the ±10 dB bandwidth of the excitation signal.

Figure 4.12 (a) shows the RC as a function of frequency with three axially separated holes, where holes 1 and 3 are fixed at a separation distance of 81.5 mm, which is equal to the wavelength at 40 kHz, while the position of the centre hole (hole 2 in the inset) is moved in steps from hole 1 towards hole 3; a total of 28 positions are included. RCs up to 70 kHz are shown for all simulated positions of the centre hole for the T(0,1) mode. The frequency of the first peak is when the defect separation between holes 1 and 3 is around half a wavelength, which in this case is around 20 kHz. Multiple defects represent successive decreases in impedance, so successive peaks occur at $L/\lambda = \eta/2$, and minima occur at separation distances of around $L/\lambda = (2\eta - 1)/4$, which is indicated on the scale at the top of the figure. The exact frequency is altered by the position of hole 2, as can be seen from the small shifts in peak frequencies in figure 4.12 (a). The amplitude of the peaks varies as the reflections from the holes go in and out of phase with each other. Depending on the relative position of hole 2, the maximum peak in the operating frequency range may correspond to the first, second or third peak. So even with pit clusters consisting of just three axially spaced holes, there is considerable complexity and variability in the RCs as the reflections from the holes go in and out of phase with each other. The intent of the figure is not to illustrate the detailed variability in RC for each position, but the bigger picture illustrating the complexity and variability in the RCs due to the above mentioned reasons.

A small peak can also be seen below $L/\lambda = 1/4$; this is an artefact that occurs because the RC approaches zero when the frequency corresponds to $L/\lambda = 1/4$, and again as the frequency tends to zero as the total axial extent of the defects becomes very small compared with the wavelength, so there must be a maximum between these frequencies. The first peak referred to in the following refers to the first peak produced by interference between the defects, not to this artefact.

Figure 4.12 (b) shows the amplitudes of the first, second and third peak

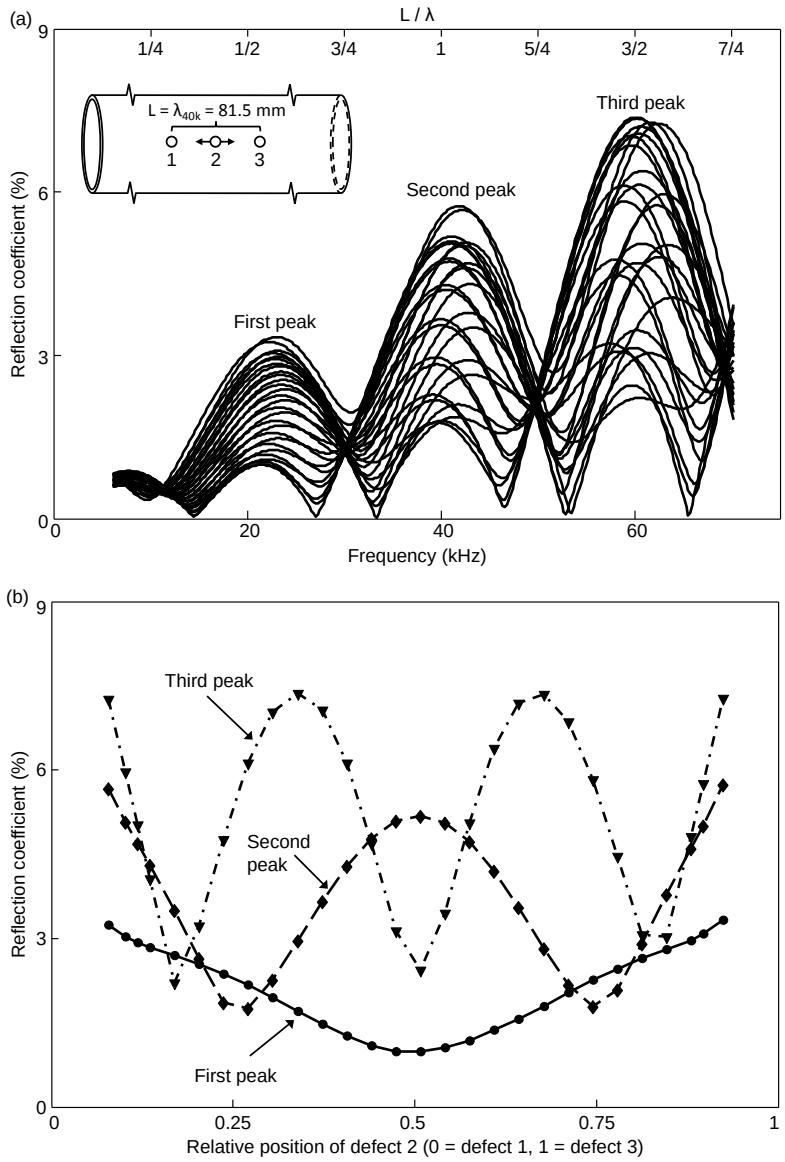

Figure 4.12: RCs as a function of frequency with three axially separated through-thickness circular holes of diameter $a = t$ for the T(0,1) mode. (a) RCs for different positions of hole 2 as a function of frequency. (b) Variation of RC for the first (solid line, •), second (dashed line, ♦) and third (dash-dotted line, ▼) peak as a function of relative axial separation distance.

RCs as a function of the relative axial position of hole 2, indicated by solid line/circles, dashed line/triangles and dash-dotted line/diamonds, respectively. As discussed above, the first peak occurs at the frequency corresponding to $L/\lambda = 1/2$. The second and third peaks occur at higher frequencies, where the defects are at $L/\lambda = 1$ and $3/2$, respectively. The amplitude of the peaks varies as the reflections from the holes go in and out of phase with each other. The maximum peak RC values at around 20 kHz (first peak), 40 kHz (second peak) and 60 kHz (third peak) in figure 4.12 (a), are roughly 2.5, 5 and 7.5%, respectively, which scales linearly with frequency since, as discussed above for the circumferentially spaced holes, the RC from each hole is a linear function of frequency. Depending on the relative position of hole 2, the maximum peak in the operating frequency range may correspond to the first, second or third peak.

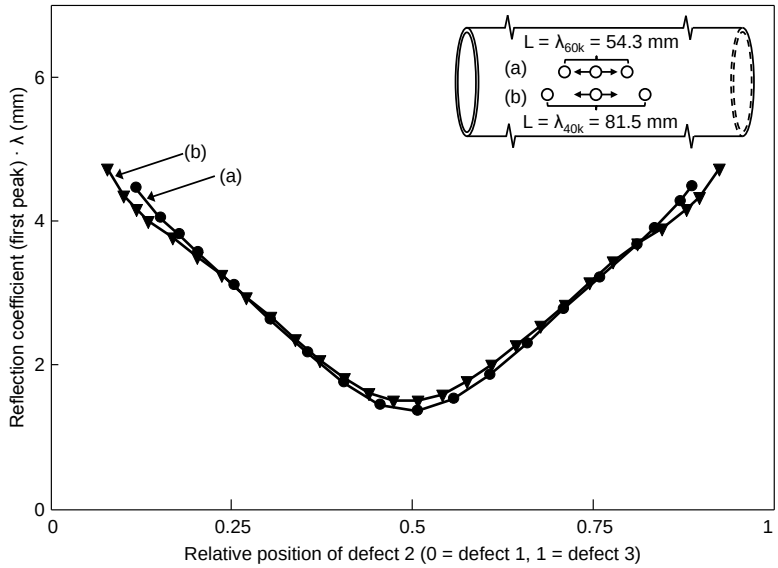

Figure 4.13: First peak RC multiplied with the wavelength at the first peak as a function of relative axial separation distance with three axially separated through-thickness circular holes of diameter $a = t$ for the T(0,1) mode. Two different defect separations are shown (see inset), where (a) is indicated by (•), and (b) by (▾).

Figure 4.13 shows the first peak RC multiplied by wavelength as a function of relative position of the defects. Two different defect layouts are investigated, shown in the figure inset as (a) and (b), with total axial extent equal to the wavelength at 60 kHz and 40 kHz, respectively. Results from (a) are shown in solid circles, while (b) are indicated by solid triangles. The two curves

superpose, showing that the first peak reflection coefficient for holes of size $a = t$ within the frequency range considered is a function of absolute frequency and relative axial separation.

Superposition results are omitted in figures 4.12 and 4.13, but showed excellent agreement with the full solution except at separation distances shorter than $2a$.

Thus, with equally spaced defects successive peaks have the same amplitude; when the defects are not equally spaced, the peaks have different magnitudes and the amplitude and frequency of the highest peak is a function of the relative defect separations which will not be known in practice.

Holes at intermediate angles

Figure 4.14 shows the T(0,1) and F(1,2) mode RCs at 60 kHz from two circular through-thickness holes as a function of the ratio of the axial separation distance to the wavelength at an angle of $\theta = 45°$, as shown in the figure inset, with the T(0,1) mode incident.

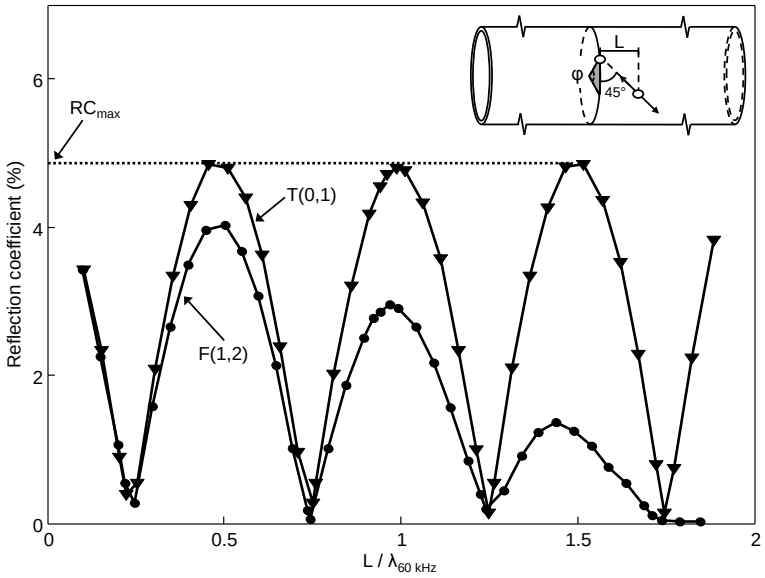

Figure 4.14: Variation of RC with axial separation for two through-thickness circular holes of diameter $a = t$ at $\theta = 45°$ for the T(0,1) (▾) and F(1,2) (•) modes at 60 kHz with T(0,1) mode incidence.

The T(0,1) reflection coefficient displays the same interference behaviour as seen in the purely axial case, while the RC for F(1,2) goes to zero as the circumferential separation between the defects approaches $\varphi = 180°$ regardless

of their axial separation, in accordance with figure 4.7. More importantly, the maximum RC for the T(0,1) mode (approximately 5%) is the same as that for axially and circumferentially separated defects (figures 4.7 and 4.9).

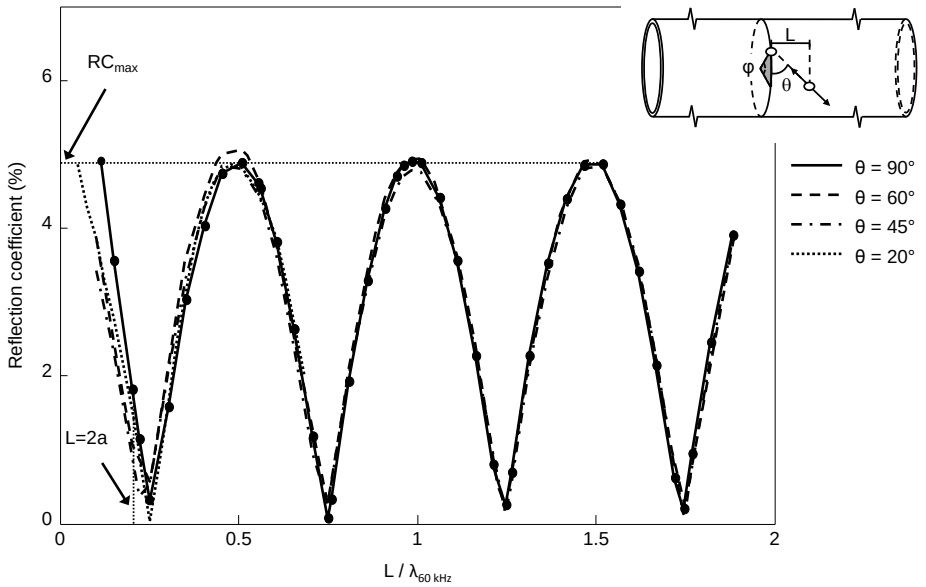

Figure 4.15: Variation of the T(0,1) reflection coefficient with axial separation for two through-thickness circular holes of diameter $a = t$ at $\theta = 20$, 45, 60 and 90° at 60 kHz.

The same analysis was carried out with angles $\theta = 20$ and 60° as well, as shown in figure 4.15, where results for $\theta = 20$, 45, 60 and 90° are shown in dotted, dash-dotted, dashed and solid lines, respectively. All the RCs display the same interference behaviour, with $\mathrm{RC_{max}}$ for T(0,1) of approximately 5% at multiples of $L\eta/(2\lambda)$, indicating that the RCs are independent of the circumferential position of the defects for $L > 2a$. At $L < 2a$, multiple scattering increasingly influences the RC.

Similar calculations as presented in figure 4.10 in the axial case ($\theta = 90°$) were also done for $\theta = 20$, 45 and 60°, which are shown in figure 4.16 as dotted, dash-dotted and dashed lines, respectively, in addition to the solid line used to indicate the axial case. The figure inset indicates the variation of hole positions. As for the axially separated defects ($\theta = 90°$), all the maxima occur at $L/\lambda = \eta/2$ and minima at $L/\lambda = (2\eta - 1)/4$, with similar amplitudes indicating that the T(0,1) RCs are independent of the relative circumferential position of the defects for $L > 2a$. At $L < 2a$, multiple scattering increasingly influences the RC, and the RC deviates increasingly as L gets smaller. The deviation varies with L for different θ, as the centre to centre distance between

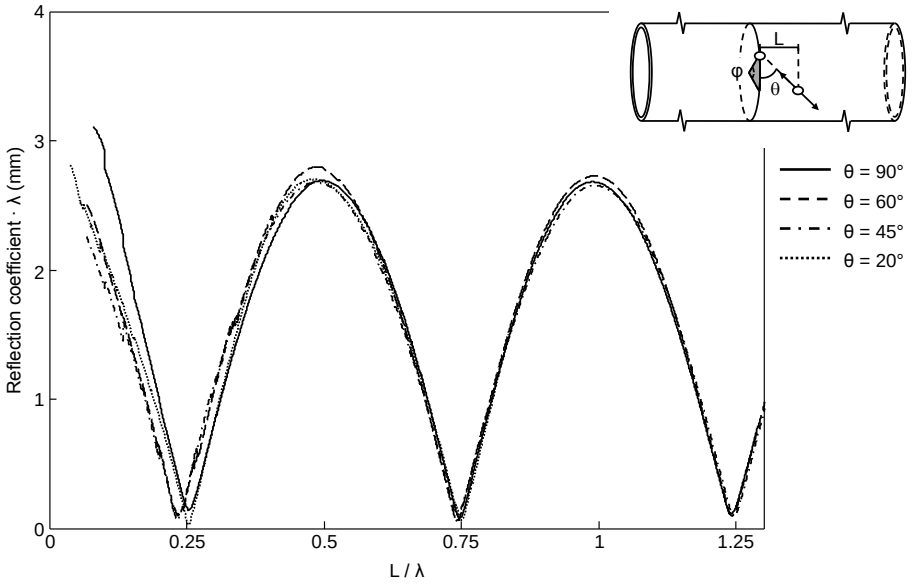

Figure 4.16: Variation of the T(0,1) reflection coefficient with axial separation for two through-thickness circular holes of diameter $a = t$ at $\theta = 20$, 45, 60 and 90°.

the defects increases more rapidly with L for low θ. Also, the angular scattering pattern of the T(0,1) mode from through-thickness holes affects the amplitude of the scattering between the holes at $L < 2a$.

Thus, the T(0,1) mode RC from circular through-thickness holes of the given size is dependent on absolute frequency and axial separation only within this frequency range.

Part-thickness circular holes

The aims of ultrasonic guided wave testing are to detect and size defects, and to evaluate whether the different defects will lead to structure failure. Of special interest is the ability to quantify the maximum depth of defects within the area inspected. Much work has been done to quantify RCs accurately as function of defect depth for cracks and notches in pipes [7, 11, 15, 17] and for cracks, notches and flat bottomed circular holes in plates [22, 28–30, 86, 87]. Here, two circular holes of 50% depth separated axially and circumferentially were modelled, in a similar way as with through-thickness holes. Figure 4.7 shows the RCs for T(0,1), F(1,2) and F(1,3) at 60 kHz for two circumferentially spaced defects, where RCs with 50% defect depth are indicated by solid triangles. Results calculated using superposition are shown in dashed lines. The same

trends as for through-thickness defects can be seen, but the RCs are about 40% of those from through-thickness defects. This is in good agreement with results from notches of comparable width [15]. However, the rise in RC due to multiple scattering and interaction between holes at small φ can be seen to be far less with 50% depth than for through-thickness holes, indicating a wider validity of the superposition approach for part-thickness defects. Also, the oscillation about the superposition results in the T(0,1) and F(1,2) modes seen for through-thickness defects is not present to the same extent, due to reduced multiple scattering from part-depth holes. Excellent agreement is seen between RCs with the full solution and superposition for defects of 50% depth.

The group of curves (d) in figure 4.8 shows the RC for the T(0,1) mode as a function of frequency over the ±10 dB range in excitation amplitude for circumferentially spaced 50% depth circular holes of diameter $a = t$. The angular separations contained within the hatched area limited by the dashed lines are in the range from $\varphi = 11 - 180°$ (see figures 4.7 and 4.8). Results from superposition calculations for the same angular separations are shown as solid lines within the hatched area. A reduced effect of multiple scattering between the holes compared to the through-thickness case can be seen throughout the frequency range as the relative spread between the RCs is small. With angular separations from $11 - 180°$ (i.e. separation distances down to $L = 1.15a$) within (d), the relative spread in RC at any frequency within the frequency range is less than ±5%. As for the through-thickness holes, the RC is a roughly linear function of frequency.

Figure 4.10 also shows RCs multiplied by wavelength as a function of L/λ for axially separated 50% depth holes for the T(0,1) mode. Axial separations of the defects from $L = 1.15a$ (lower limit to avoid geometrical intersection of the holes) upwards in steps of $0.25a$ are included in the averaging. The same periodicity as a function of L/λ as for through-thickness holes is seen, only with amplitudes of 40% of the through-thickness cases, which again agrees well with results from notches of comparable width [15].

Achieving better agreement between superposition and the full solution for part-thickness defects at short separation distances than for through-thickness defects further encourages the investigation of using superposition to simulate multiple part-depth defects and defect clusters. This will be further assessed in Chapter 5.

4.4 Experimental validation

A series of laboratory experiments was carried out on two 6 m long 3 in. nominal bore schedule 40 steel pipes (outer diameter 88.9 mm, wall thickness 5.5 mm) in order to validate the main findings from the FE analyses. The pipes were tested horizontally while resting on wooden supports which produced negligible reflections. A standard Guided Ultrasonic Ltd. [10] transducer ring consisting of two rows of 12 equally spaced piezoelectric transducers applying alternating

forces in the circumferential direction was clamped on the external wall of the pipe to excite the T(0,1) mode in both directions in the pipe.

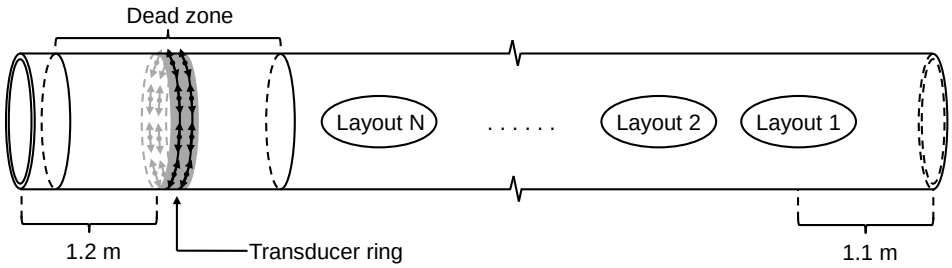

Figure 4.17: Schematic of experimental setup.

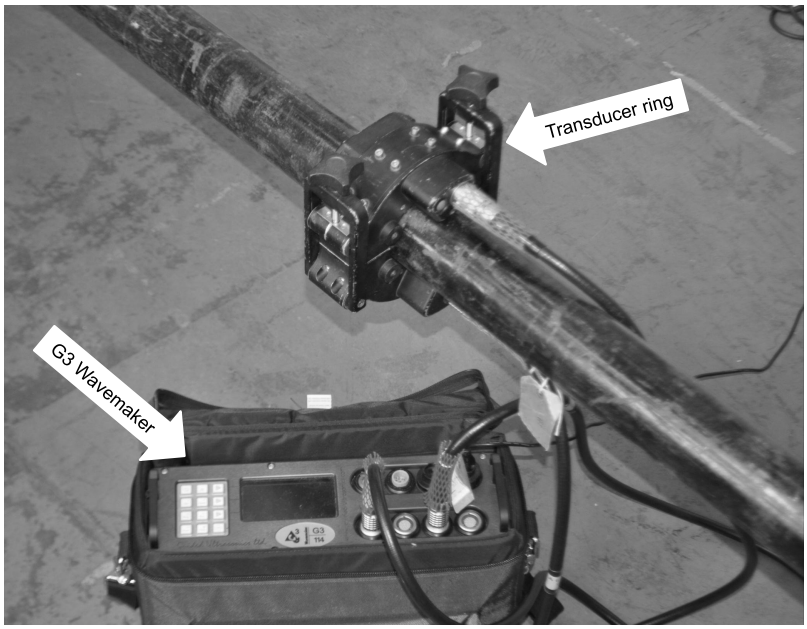

Figure 4.18: Mounted transducer ring and G3 Wavemaker excitation instrument, both from Guided Ultrasonics Ltd.

A Guided Ultrasonics Ltd. G3 Wavemaker instrument was used to generate a series of 8 cycle Hanning windowed tonebursts, giving an excitation bandwidth of around 20–55 kHz. The transducer ring was also used as a receiver. A schematic of the experimental setup is shown in figure 4.17, while the mounted

transducer ring and G3 Wavemaker excitation instrument, both from Guided Ultrasonics Ltd. [10], are shown in figure 4.18.

The reflection from the left hand end of the pipe acts as a reference. In order to avoid the dead zone of the ring, a distance to the left hand end of around 1.2 m was employed. The different defects layouts were drilled at the other end of the pipes in steps sufficiently far apart to separate in time the reflections from the defect cluster of current interest from the reflections caused by defect layouts drilled farther along the pipe, moving from the far end of the pipes towards the ring until the dead zone was reached. Attenuation differences due to different signal propagation distance as the layouts were machined closer to the transducer ring are negligible. The first defect layout was drilled at 1.1 m from the right hand end in order to separate the reflections of interest from the end reflection. Seven series of experiments were carried out in total, and each case was measured sequentially before the next hole was added to the given layout. The transducer ring was removed from the pipe between each addition of a new hole, and put back at approximately the same location for the next measurement. Reflection coefficients were calculated in the time domain as peak-to-peak amplitude ratios between the reflections from the various defects and the reference end reflection. Since the reflection coefficients are small, up to 48 averages were employed, and a signal to noise ratio (SNR) between the reflection from the defect(s) and the background noise greater than 3 dB was required for the results to be used.

Corresponding FE calculations were carried out on 3 in. nominal bore schedule 40 steel pipes (outer diameter 88.9 mm, wall thickness 5.5 mm) for direct comparison, using 2 mm quadratic tetrahedral elements, exciting a 2 cycle Hanning windowed toneburst with a centre frequency of 60 kHz. Figure 4.19 shows a comparison between FE calculations and experiments for circumferentially spaced holes of diameter $a = t$ for the T(0,1) mode. RCs for the experimental results with one, two and three defects are shown by solid diamonds, squares and circles, respectively, while the FE results are shown in solid lines for all cases. The holes were added and measured one at a time, with separation distances along the outer diameter of the pipe as indicated in the figure inset. Excellent agreement can be seen between the FE predictions and experiments, verifying that the RC for circumferentially spaced holes is a roughly linear function of frequency. Likewise, the RCs can be seen to be a linear function of the total circumferential extent of the holes, as the RC for two holes is double that for one hole, while RC for three holes is triple that for one hole.

Figure 4.20 shows results comparing FE calculations and experimental results for axially spaced holes of diameter $a = t$ for the T(0,1) mode. RCs multiplied by the wavelength are shown as a function of L/λ for two and three holes. Results for the case of one hole are shown at $L/\lambda = 0$, since there was no separation distance to another hole, where the triangle shows the experimental result and the star the FE predictions. For the cases with two and three holes,

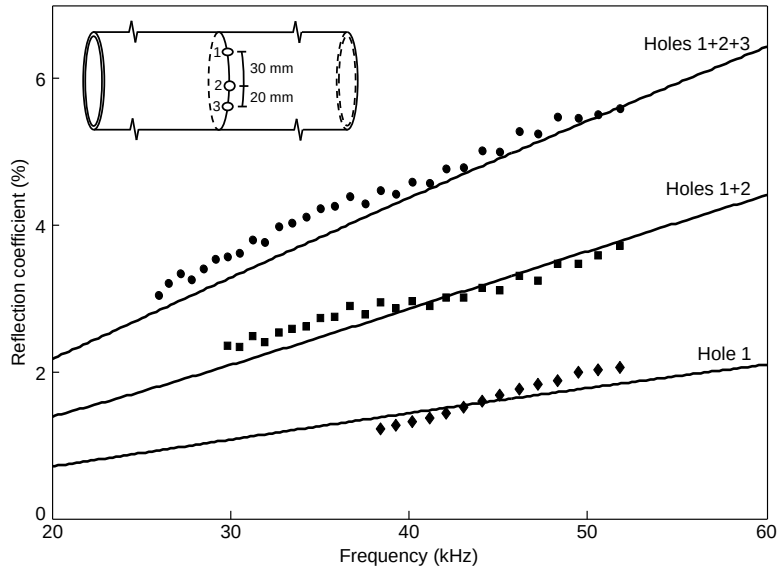

Figure 4.19: Comparison between FE (lines) and experiments (markers) with holes of diameter $a = t$ for the T(0,1) mode. Variation in RC as a function of frequency with one (♦), two (■) and three (•) circumferentially spaced holes.

FE results are shown as lines, while experimental data by markers. FE results for three holes (holes 1+2+3) separated individually by $L = 40$ mm, and for two holes at $L = 40$ mm (holes 1+2) and 80 mm (holes 1+3) are included. Again, the holes were drilled into the pipe and measurements were taken after each hole was added. Measurements with holes 1+3 were done as a separate layout, at a different position on the pipe, than the measurements for hole 1, 1+2 and 1+2+3. The peaks from the measured RCs can be seen to be shifted slightly in frequency compared with the FE results, but in general very good agreement is found, with the largest deviations at the upper and lower ends of the frequency bandwidth. The maximum RC from two holes (at $L/\lambda = 0.5$) is twice that of one hole (at $L/\lambda = 0$); the maximum RC from three holes is three times that from one hole, as the separation between the defects is equal. Good agreement is also seen between RCs from holes separated by $L/\lambda = 0.5$ (holes 1+2) compared with the holes when the distance between them is doubled ($L/\lambda = 1$, holes 1+3).

Figure 4.21 shows a comparison between FE (line) and experiments (markers) of the variation in RC as a function of axial defect separation for two circular holes at angles of $\theta = 90°$ (squares) and 45° (circles) for holes of diameter $a = t$ for the T(0,1) mode, as shown in the figure inset. The axial separation is 40 mm in both cases. The RCs for both angles can be seen to be

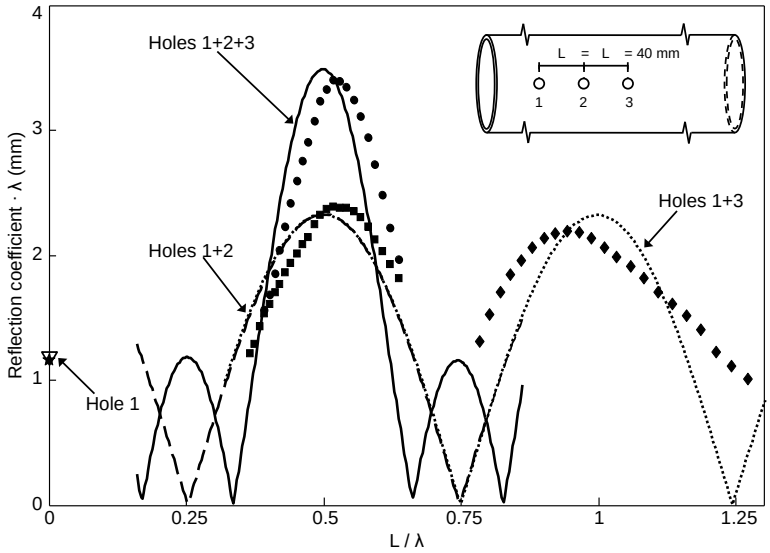

Figure 4.20: Comparison between FE (lines) and experiments (markers) with holes of diameter $a = t$ for the T(0,1) mode. Variation in RC multiplied by wavelength as a function of axial separation for one hole ($\triangledown$ = FE, $\bigstar$ = experiment), two holes (1+2) at $L = 40$ mm (dashed line = FE, $\blacksquare$ = experiments), two holes (1+3) at $L = 80$ mm (dotted line = FE, $\blacklozenge$ = experiments), and three holes (1+2+3) each at $L = 40$ mm (solid line = FE, $\bullet$ = experiment).

comparable, with reasonable agreement between FE and experimental results, which verify the findings from the FE analyses that the RC for the T(0,1) mode is dependent on axial separation only, provided that multiple scattering between the defects can be neglected.

4.5 Conclusions

A parametric study of the reflection from two and three small circular holes at different relative positions in a pipe with the fundamental torsional mode incident has been carried out. The reflection of the T(0,1) mode has been analysed, and the mode converted reflections of the F(1,2), F(1,3) and F(2,2) modes have been assessed. The work has been done using finite element (FE) modelling, and validated experimentally, and is a step towards understanding and estimating the scattering behaviour of multiple and randomly spaced defects. The validity of employing a superposition approach in calculating the reflection coefficients (RCs) has been assessed as a function of defect separation and orientation.

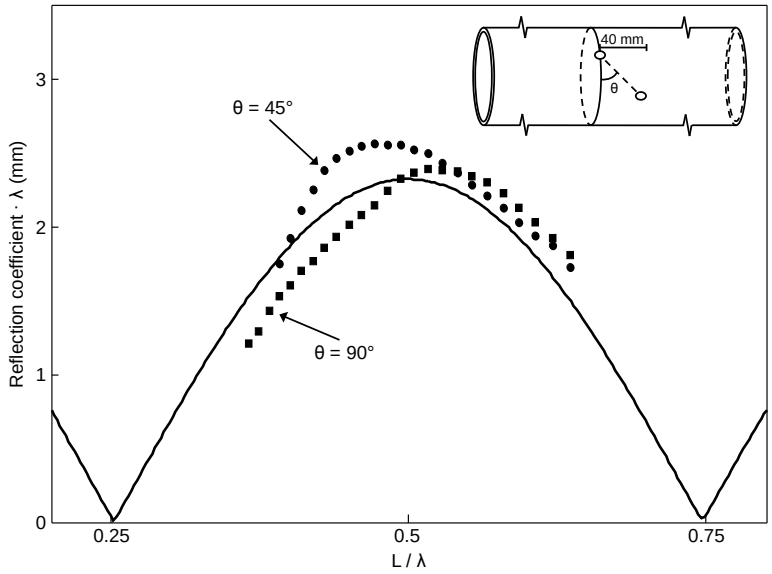

Figure 4.21: Comparison between FE (lines) and experiments (markers) with holes of diameter $a = t$ for the T(0,1) mode. Variation in RC as a function of axial defect separation for two circular holes separated axially by 40 mm at angles of $\theta = 90°$ (■) and 45° (•).

With circumferentially spaced defects, the RC for the T(0,1) mode was found to be independent of the circumferential position of the circular holes, provided the distances between them were larger than around $2a$ for through-thickness defects, where a is the diameter of the holes. At shorter separation distances, multiple reflections between the defects influence the RC. The superposition approach was found to be valid down to similar defect separation distances. A linear relationship between the RCs from circumferentially spaced defects and the total circumferential extent of the defects was seen. Also, since the individual hole diameters were small compared to the wavelength, the RCs were found to be roughly linear functions of frequency.

For axially spaced defects, strong interference effects were seen in the RCs, governed by the defect separation distance, with the maximum RC being equal to that found for circumferentially separated defects for the T(0,1) mode. With two circular holes spaced at other orientations than purely circumferential or axial, the RC was again found to be independent of circumferential position, thus being comparable to the axial case if plotted against the parameter L/λ, where L is the axial separation distance and λ denotes wavelength. Superposition was found to be applicable down to a separation of around $2a$ for all defect orientations for through-thickness holes. With part-thickness defects RCs were

smaller, and superposition was valid down to shorter separation distances as multiple scattering became less significant in this case, which suggests that using superposition to simulate multiple part-depth defects and defects clusters will be satisfactory.

With three axially separated defects, the frequency of the first peak reflection coefficient is governed by the total axial extent of the defect layout. When the holes are separated equally and the distance between successive holes is a multiple of $\lambda/2$, constructive interference occurs and gives rise to maxima in the reflection coefficient. This condition is not necessarily met at the first peak frequency so the reflection coefficient may be higher at subsequent peaks.

As destructive interference between reflections from axially spaced defects results in low reflection coefficients, guided wave testing should preferably be carried out covering a large frequency bandwidth, and also repeated regularly to monitor the potential development and growth of corrosion attacks.

Experiments were carried out to validate the main findings from the finite element predictions. Good agreement was found for all the defect layouts tested.

Chapter 5

The reflection of the fundamental torsional guided wave from pit clusters in pipes

Following the findings in Chapter 4, this chapter studies the reflection coefficient (RC) from pit clusters using the fundamental torsional guided wave. Section 5.1 presents an introduction to localised corrosion and the use of guided waves for its detection, extending the discussion in Section 4.1. Typical realistic defect geometries from a corrosion science point of view are also discussed. As the aim here is to estimate the RC from pit clusters consisting of a random number of pits that have developed randomly in size and depth following certain growth rules, these rules and development procedures are explained in Section 5.2.

Following the approach explained in Section 5.2, the (maximum) RCs from a large number of randomly developed pit clusters are evaluated, and possible relationships to maximum defect depth discussed for clusters growing out of areas otherwise affected by general corrosion only and with clusters being part of a larger attack in Section 5.3. Also, problematic cases where given pit clusters with deep maximum depth result in a low maximum RC are assessed for test optimisation and evaluation. A variety of cluster types, sizes and shapes is evaluated employing efficient calculation techniques, as explained in Section 5.2, and a relevant selection is validated experimentally in Section 5.4. Finally, conclusions are drawn in Section 5.5.

5.1 Introduction

Corrosion of carbon and low-alloy steels, which are used extensively in the petro-chemical industry, caused by CO_2 and H_2S is a major concern for the integrity of subsea pipelines [3]. Corrosion has been reported to account for 25%

of all safety incidents, the majority of which are due to CO_2 [1]. The presence of CO_2 and/or H_2S in oil and gas production always implies a risk of material damage and shutdown due to corrosion, and especially localised corrosion. The morphology of corrosion attack ranges from general corrosion, where the entire surface is evenly attacked, to localised corrosion which is limited to discrete sites, such as pitting and pit clusters, mesa corrosion and crevice corrosion. Pits can be of various shapes and grow together or be adjacent to each other to form pit clusters [2], while mesa corrosion typically consists of broad, shallow pits which grow together to form larger defects [106]. The corrosion rate and growth law of localised corrosion is very variable, as is the maximum pit depth compared to the mean wall loss [4]. Many models exist within the corrosion community to estimate the initiation and growth of pitting corrosion [107, 108]. These models mainly consider stages of the localised corrosion attack where the pits are measured in micrometres. One well-known empirical model for pit depth and diameter growth is $d(t) = \gamma^{tn}$, where t is exposure time while γ and n are parameters related to the corrosion process and the environment [4, 108]. However, Melchers [109] reported that after longer exposure times, when pits are measured in millimetres rather than micrometres, their growth is not consistent with this growth law. Both Melchers [109] and Engelhart et al. [110] reported that corrosion pits tend to grow faster in width than in depth as they increase in size, while the depth growth rate of mesa attacks commonly are in same range or shallower than the lateral growth rate, according to Nyborg [97]. For single pits Codaro et al. [98] reported a depth growth rate equal to, or somewhat larger than, its surface diameter growth, depending on the shape of the pit at the surface, as discussed in Chapter 4, while Nakai et al. [111] reported a typical diameter to depth ratio of pits of around 4–6:1 at the bottom of oil tankers.

When leaks, ruptures or fatigue occur in pipelines it is usually caused by internal H_2S/CO_2 corrosion resulting from large, wide pits and pit clusters [2]. Areas surrounding the pits can be affected by general corrosion or relatively shallow corrosion for most types of steels other than stainless steels, which are only affected to a small extent by general corrosion, or the pits may be part of a wider, shallower corrosion attack [98, 109]. With pit clusters, the maximum pit depth may change between different pits as the clusters develop with time, and commonly there are several pits that have reached a given depth within the cluster [109, 112].

As discussed in Section 4.1, ultrasonic guided wave inspection is now a well-established technique within non-destructive testing (NDT), especially for pipelines in the petro-chemical industry. Guided wave testing allows rapid and reliable inspection over longer distances, including buried, coated or otherwise inaccessible pipe segments, and interrogates the entire pipe wall as the cylindrical guided waves produce stresses throughout the wall thickness. Compared with conventional ultrasonic testing, which is limited to a small area in the vicinity of the transducer, guided wave testing provides the user with a much

higher chance of detecting localised defects, at the expense of less accurate sizing of the detected defects as the testing is carried out from a distance [52, 79]. Extending the applicability of guided wave testing from defect detection to defect sizing is highly desirable, especially to quantify the maximum defect depth within the test range. However, this requires detailed knowledge about the interaction of the incident wave with different defect types in pipes in order to interpret the reflections from them correctly, into which much work has been devoted by many researchers [7, 9, 11, 12, 14–21]. Understanding the scattering from various relatively simple defect shapes, such as cracks [15, 22, 23], notches [11, 17], circular holes [24, 25], and ellipses [26], is a necessity in order to understand more complex defect shapes and/or multiple defect attacks commonly encountered. Real corrosion patches can often be well represented by simpler defect shape approximations.

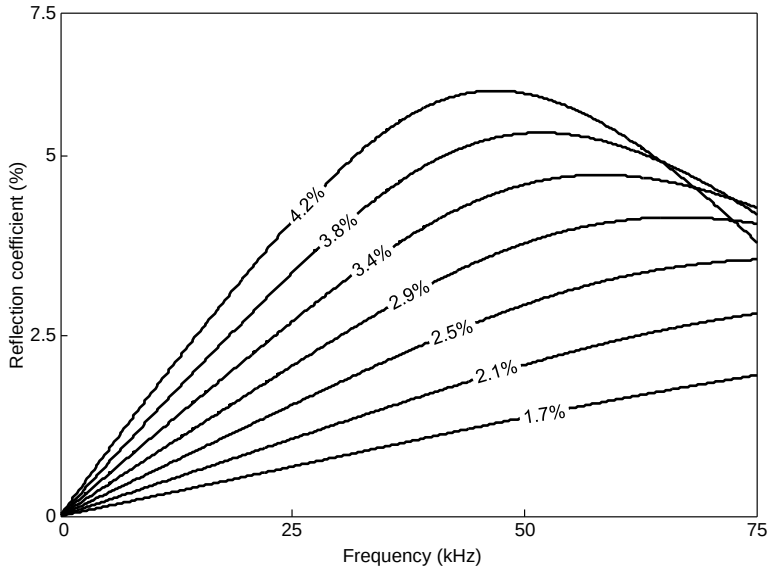

Figure 5.1: Variation of RC with frequency for a single circular hole with depth equal to 90% of the pipe wall thickness. Hole diameters are given as percentage of the total pipe circumference.

The fundamental torsional mode, T(0,1), which presently is the most frequently used mode for NDT in pipes, is used throughout this chapter, as it was in Chapter 4. It has several desirable features such as being non-dispersive at all frequencies and being unaffected by liquid present on the inside or outside of the pipe. Long range screening of pipelines using cylindrical guided waves typically aims to detect defects of order 5% or more of the cross-sectional area at a given axial distance [7], but defects down to 1% of cross-sectional area can

be detected under optimal testing conditions. Long range guided wave testing generally uses frequencies below 100 kHz, with bandwidths of around 30–50 kHz.

Figure 5.1 shows the reflection coefficient (RC) as a function of frequency for different sized single circular holes of depth 90% of the pipe wall thickness calculated from finite element simulations, details of which will be presented in Section 5.2. For single defects successive peaks in the RC occur at $L/\lambda = \eta/4$, where L is the axial extent of the defect, λ is wavelength and η is a counter variable, while the RC is linearly proportional to the circumferential extent of the defect [11, 15, 17, 25, 26]. For the frequency range included in figure 5.1, no peak in the RC is visible for hole diameters shorter than 2.9% of the pipe circumference. Additionally, none of the holes are large enough to include multiple peaks in the RC within this frequency range. With two axially separated holes, successive peaks occur at $L_{\text{sep}}/\lambda = \eta/2$, where L_{sep} is the centre to centre separation between the holes, regardless of their circumferential position. With two circumferentially spaced holes, the RCs from the individual holes will add, and no peaks due to interference between the holes will be seen, as discussed in Chapter 4 and in [25]. As the corrosion attacks become more complex, possibly consisting of multiple defects of various depth, size and shapes, RCs become complex, frequently consisting of multiple peaks. In practical test situations the number and shape of defects are unknown, and the frequency range employed in the test will be limited by the testing equipment. Most commonly the maximum RC is used as the evaluation parameter, which is a sensible choice as the possible presence and values of peaks in the RC within the bandwidth of the interrogating signal depend on the geometrical properties of the defect(s).

As mentioned earlier, the maximum defect depth within the testing range is the most important parameter to quantify in most NDT. Here, the RCs from pit clusters consisting of a random number of pits that have developed randomly in size and depth following certain growth rules explained in Section 5.2 will be predicted. With this approach, the maximum RCs from a large number of randomly developed pit clusters can be evaluated on a statistical basis, and possible relationships to maximum defect depth found. Also, problematic cases where given pit clusters with deep maximum depth result in a low maximum RC can be assessed for test optimisation and evaluation. A variety of cluster types, sizes and shapes is evaluated employing efficient calculation techniques, as explained in Section 5.2.

5.2 Method and finite element model

This section describes the method used to evaluate large numbers of randomly developed pit clusters. For this to be practically achievable the superposition technique is employed to calculate the RCs from the clusters, and the corresponding full solution is calculated for a selection of cases. In employing

superposition, RCs for single pits are calculated using the finite element (FE) method, and subsequently superposed in post processing calculations to calculate the total cluster RC. FE analyses are used to evaluate the full solution cases also.

Firstly, the FE model is explained. Then the pit cluster growth model is discussed in the subsequent subsection, before the properties of superposition are outlined in the following subsection; finally, FE validation and comparison between full solution and superposition results are discussed in last subsection in Section 5.2.

Finite element model

Full 3D FE models were employed in all FE analyses throughout this chapter, modelling 4 in. nominal bore schedule 40 pipes (outer diameter 114.3 mm, wall thickness 6.02 mm) in the commercially available software program ABAQUS version 6.9 [74]. A 2 cycle Hanning windowed toneburst with centre frequency of 50 kHz was used, exciting the T(0,1) mode by applying the excitation toneburst as tangential displacements at 90 evenly spaced nodes around the outer circumference of the pipe, as shown in figure 5.2.

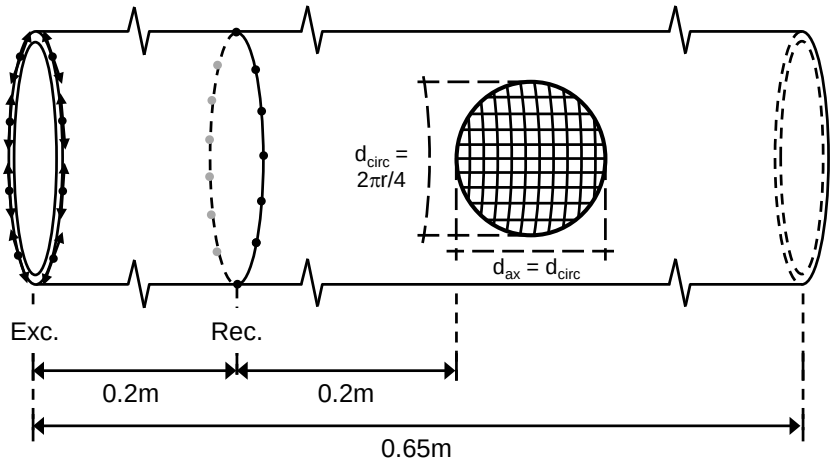

Figure 5.2: Schematic of finite element models and cluster grid. Excitation applied in circumferential direction at outer nodes at the left hand end of the pipe; reception in circumferential direction at nodes around the pipe at the receiver location. The defect grid is located further along the pipe to separate the incident and reflected signals.

The pipe length, location of receiver positions and defect location were chosen so that the incident and reflected signals could be well separated, as indicated on the figure, where an example defect grid with both axial and circumfer-

ential size equal to a quarter of the pipe circumference, $d_{\mathrm{ax}} = d_{\mathrm{circ}} = 2\pi r_{\mathrm{pipe}}/4$, is shown. Throughout this chapter, the term grid designates possible pit initiation sites as shown in figure 5.2, while the term mesh is used in relation to the FE resolution. RCs were calculated in the frequency domain throughout, and are defined as the ratio of the surface circumferential displacement amplitude of the reflection to that of the incident wave.

Quadratic tetrahedral elements with element length of 1.5 mm were used throughout the FE modelling, giving an approximate nodal separation of 0.75 mm. A time step of 10 ns was used. Convergence tests were run to ensure that the mesh size and time steps were appropriate. In this case the mesh size is not controlled by the traditional rule of a given number of elements per shortest wavelength as discussed in Section 2.5 and [76], but by the short distance between deep defects and the inner pipe wall (0.6 mm in the case of 90% deep pits) and/or densely populated pit clusters that require small elements to be modelled satisfactorily.

Pit cluster growth

As discussed in Section 5.1, many different models of pit growth, initiation and morphology exist, and it is the subject of much research and discussion within the corrosion community. A simplistic model is used here, where the clusters are developed through a random number of development steps. For each step there is equal probability at which grid node within the defect grid a pit will grow. If a pit is already present at the given grid node, the pit will grow either in depth or in width with equal probability. Figure 5.3 shows the single pit growth scheme used, where the numbers indicate the number of growth steps needed for the given pit size to develop. Flat-bottomed circular holes are used, with defect diameters from $1t$ to $2.5t$ in increments of $0.25t$, where t is the pipe wall thickness, and with increments in depth of 10% of the pipe wall thickness. If a pit has reached maximum depth it may only grow in width, and vice versa. If the maximum width and depth have been reached, the grid point is unavailable for selection. The reason for limiting the maximum pit diameter to $2.5t$ is related to the use of superposition, and is explained in detail in the next subsection. There are multiple ways for a pit to develop into a given shape, as indicated in the top left quadrant of figure 5.3; the diagonal arrows in the other quadrants indicate similar growth possibilities as shown in detail in the upper left quadrant. Example pit shapes shown explicitly in figure 5.3 are for illustration purposes only, there is no requirement for a given pit to develop through these example growth stages.

Figure 5.4 (a) shows an example cluster grid with three defects at the given stage of development. Because pits may grow in width if the same grid node is selected multiple times, a certain spacing between each possible pit generated is needed to keep two pits from growing into each other. This spacing is given by the pit sizes and the cluster grid size, and is governed by the validity of

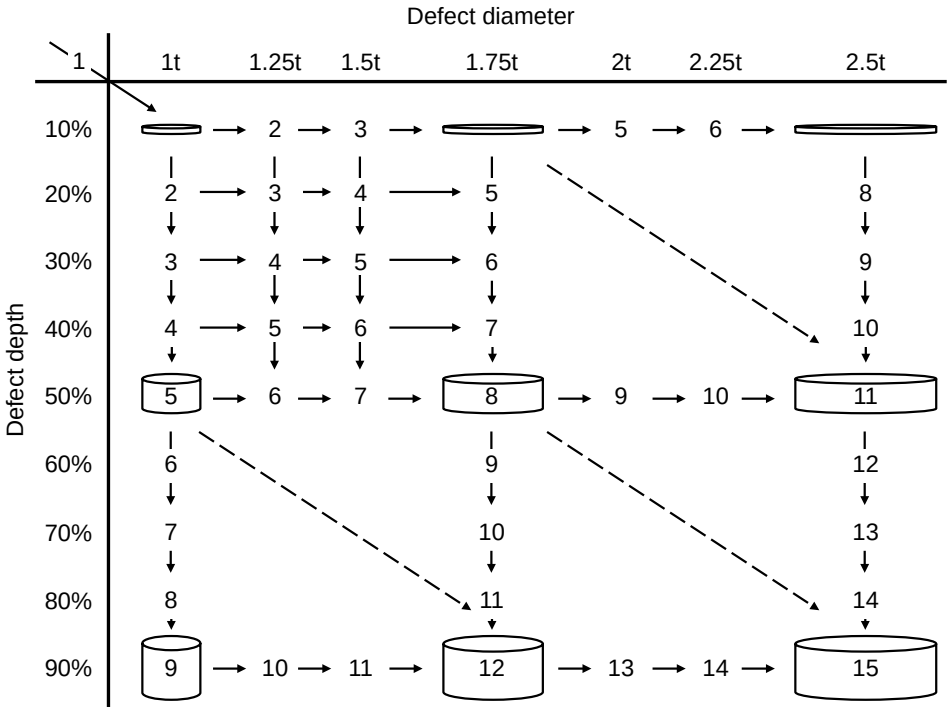

Figure 5.3: Single pit growth scheme; the numbers indicate number of growth steps at a given location in the defect grid. The diagonal arrows indicate the same growth possibilities as shown in detail in the upper left quadrant of the figure.

superposition, as outlined in the following subsection. The black dots around the holes indicate grid nodes where no new pit can be initiated once the three holes shown are present; if any of these intermediate nodes is selected, the choice is ignored and a reselection is made. Different defect grid sizes were studied, and a grid size of $dx = dy = 1t$ was chosen and employed throughout the simulations, as shown in figure 5.4 (b). With the largest pit size of diameter $d = 2.5t$ and a grid size of $1t$, the lowest separation possible between pits then becomes $L_{\text{sep}} = 1.2d$ centre to centre, for which acceptable validity of employing superposition is achieved, as explained in the next subsection. This situation is shown in figure 5.4 (b), which shows a $d = 2.5t$ pit to the left, and the closest a new pit may initiate to the right, where the initial ($d = 1t$) and maximum ($d = 2.5t$) pit sizes are indicated by solid and dashed circles, respectively. With this grid size, range of pit sizes in width and depth, and a circular defect domain in which pits can grow of size $d_{\text{ax}} = d_{\text{circ}} = 2\pi r_{\text{pipe}}/4$, the lowest number of growth steps that can leave no valid growth step remaining is 126. Thus, a

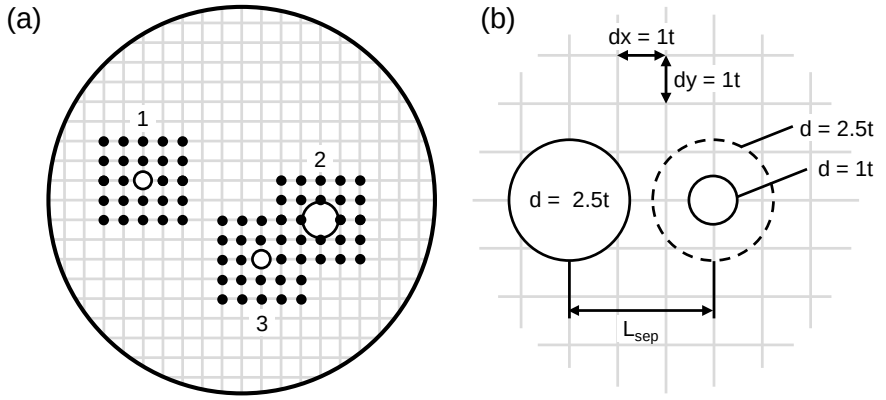

Figure 5.4: (a) Random selection and spacing requirement between adjacent pit locations. (b) Details of grid size and minimum separation between adjacent pits; thus $L_{\text{sep}} \geq 1.2d$ with a grid size of $1t$.

random number of pit development steps in the range 1-126 was employed.

As randomness is an inherent and unavoidable characteristic of pitting corrosion over time [4], the defect domain size and shape may vary accordingly. However, Papavinasam et al. [96] reported that the majority of internal pitting corrosion in oil and gas pipelines lies between the 4 and 8 o'clock positions in the pipe, while Gunaltun et al. [113] reported top of line corrosion in multiphase gas lines to be between the 10 and 3 o'clock position. In the following the circumferential extent of the pit clusters are limited to a maximum of 25% of the pipe circumference.

Superposition calculations

As concluded from the analysis done in Chapter 4, the validity of superposition is valid if $L_{\text{sep}} \geq 2d$ in the worst case with through-thickness defects [25], in accordance with similar earlier studies for bulk waves [64, 100]. However, for part-thickness defects, the validity was found to be significantly better [25]. Obviously, with less developed pit clusters consisting of coarsely populated clusters and/or pits of small diameter, centre to centre distances between pits are likely to be larger than the worst case of $L_{\text{sep}} = 1.2d$.

Superposition calculations are based on FE calculations of single defect types; each defect type (i.e. possible pit sizes and diameters in figure 5.3) was simulated using the model shown in figure 5.2. Based on the location and type of pits in the randomly generated pit clusters, the appropriate time delay (or phase delay in the frequency domain) was added to the reflection from each pit in the cluster depending on their position. Finally, all the shifted reflections

from the defects were added together to obtain the total pit cluster reflection, and the total RC of the cluster was calculated as the ratio of the sum of all the reflections from the individual defects to that of the incident signal.

Finite element validation

Extensive comparison between full solution and superposition results has been done, both with defect grid size of $dx = dy = 1t$ and $1.5t$. Clearly, the finer the defect grid used, the larger number of possible initiation sites for pits in the clusters, which is desirable in order to model as realistic cluster layouts as possible. Very good agreement was seen with both defect grid sizes, with slightly larger deviation with the finer grid of $1t$, as expected.

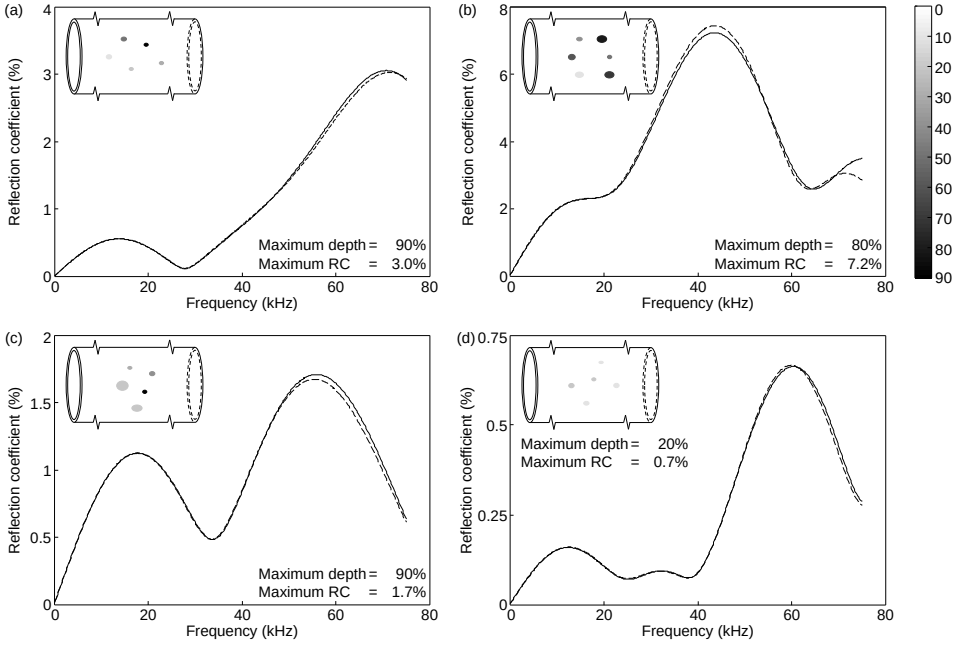

Figure 5.5: Example pit clusters with grid size of $dx = dy = 1.5t$, where full solution (solid lines) and superposition (dashed lines) calculations are compared. Pit depth, size and position are indicated in the figure insets, where pit depths are indicated in color scale (from 10–90%).

Figures 5.5 and 5.6 show four example pit clusters with grid size of $dx = dy = 1.5t$ and $1t$, respectively, comparing the full solution (solid lines) with superposition (dashed lines) calculations, showing frequencies up to 75 kHz. The pits are shown in the figure insets, where the colour scale indicates the depth of each pit (from 10–90%). With a grid size of $dx = dy = 1t$, the deviation

between the full solution and superposition in maximum RC was found to be less than 4% in most cases, and the maxima occurred at frequencies within 5% of each other. With highly developed clusters, where several large and deep pits were adjacent to each other, a somewhat larger shift in frequency was seen in some cases. The largest deviation in maximum RC was found for the highly developed example cluster shown in figure 5.6 (c) where the maximum RC occurs at the highest frequency within the bandwidth of the interrogating signal, where the RC typically changes rapidly with frequency. In this case a deviation in maximum RC of 10% was found. This, and other problematic cases will be discussed in more detail in subsequent sections, two of which are validated experimentally in Section 5.4 also. A defect grid size of $1t$ is employed throughout this remainder of the chapter.

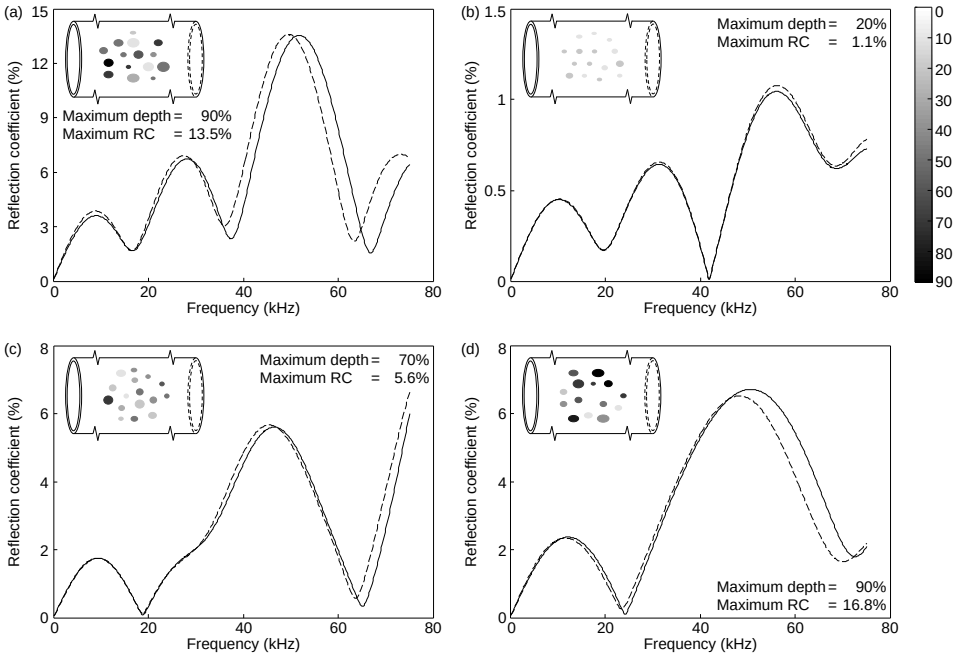

Figure 5.6: Example pit clusters with grid size of $dx = dy = 1t$, where full solution (solid lines) and superposition (dashed lines) calculations are compared. Pit depth, size and position are indicated in the figure insets, where pit depths are indicated in colour scale (from 10–90%).

5.3 Finite element predictions

The first subsection in this section evaluates the reflection from pit clusters in areas that are otherwise affected by general corrosion only, while clusters that are part of larger attacks are discussed in the subsequent subsection. The clusters are developed as described in Section 5.2.

Pit cluster results

Reflections from all single defects shown in figure 5.3 were obtained by modelling them one at the time, as explained in Section 5.2. Randomly generated pit clusters were then developed using the model shown in figure 5.2, as explained in Section 5.2. Frequencies up to 75 kHz are included in the analyses.

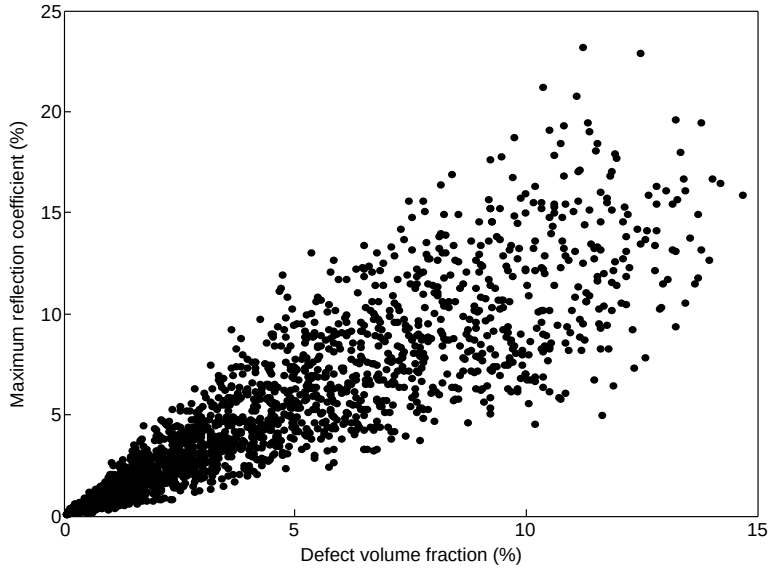

Figure 5.7: Maximum RC as a function of defect volume fraction (ratio of total pit volume to the volume of the circular defect domain multiplied by the pipe wall thickness). Results from 2000 example cases are included in the figure.

Figure 5.7 shows the maximum RC as a function of defect volume fraction for 2000 example layout cases, where the defect volume fraction is defined as the ratio of total pit volume to the volume of the circular defect domain multiplied by the pipe wall thickness. As expected the maximum RC follows a linear trend with increasing volume removed from the pipe (more developed clusters), with very significant scatter. The more and larger pits that are present in a cluster, the larger the maximum RC in general. However, as the clusters have an axial extent, reflections from discrete pits may interfere destructively, leading to lower

maximum RCs. The sample results shown in figure 5.7 illustrate the usefulness of applying a statistical approach in the evaluation of possible pit clusters and other complex corrosion patches in determining probable maximum RC ranges and distributions.

Percentiles are frequently used in statistical analyses to quantify values below which, or intervals into which, a certain per cent of observations fall. Here we will be interested in the percentage of pit clusters in which there is a pit with maximum depth larger than a given value (or lies in a given range) that give maximum RCs that are less than given values, and would therefore be difficult to detect. Figure 5.8 shows the percentage of clusters with maximum RC less than the values of the abscissa for maximum pit depths within certain depth intervals in figure 5.8 (a), or deeper than given depth values in (b), as indicated in the figure legends.

The maximum RCs and depth percentages are calculated from a series of 100,000 randomly generated pit clusters. An example value for interpretation is indicated by the dashed lines in both (a) and (b). In (a) the clusters are divided into maximum depth intervals of 10%; the example value indicated shows that 35% of the maximum RCs for pit clusters with maximum depth in the range from 80–90% of the pipe wall thickness are lower than 6%, from which it follows that 65% of the cases result in a maximum RC that is larger than 6%. Similarly, by extending the dashed line indicating 6% maximum RC up to 100% (all the clusters simulated), it can be seen that almost no pit clusters with maximum defect depth lower than 50% result in a maximum RC larger than 6%, as only a small percentage of the clusters in the maximum depth interval from 40–50% exceed 6% maximum RC, and none of the shallower ones do.

Figure 5.8 (b) uses the same calculation series, but shows the percentage of clusters with maximum defect depth deeper than the thresholds indicated in the legend as a function of the corresponding maximum RCs. Again, an example value is indicated by short dashed lines, which shows that in 12% of the cases with pit clusters with maximum depth deeper than 70% the maximum RC is less than 4%. Even some clusters with maximum pit depth of 90% or deeper result in a maximum RC that is below 3–4%, which consequently will be difficult to detect reliably in practice. As shown in figure 5.1 for 90% deep single circular holes, where the pit sizes correspond to diameters between 1 and $2.5t$ in steps of $0.25t$, the single pit diameter must be $> 2.5\%$ (corresponding to $1.5t$ in this case) of the pipe circumference in diameter to give a RC of 3% within the frequency range used here. If multiple pits interact destructively, pit clusters with larger pits of 90% depth might also give a small reflection and not be detected.

Cluster morphologies with low maximum RC and deep maximum depth are problematic from a NDT detection point of view. Examples of typical problematic cluster morphologies from the calculation series shown in figure 5.8 are given in figure 5.9, where the layouts are shown on the insets; the

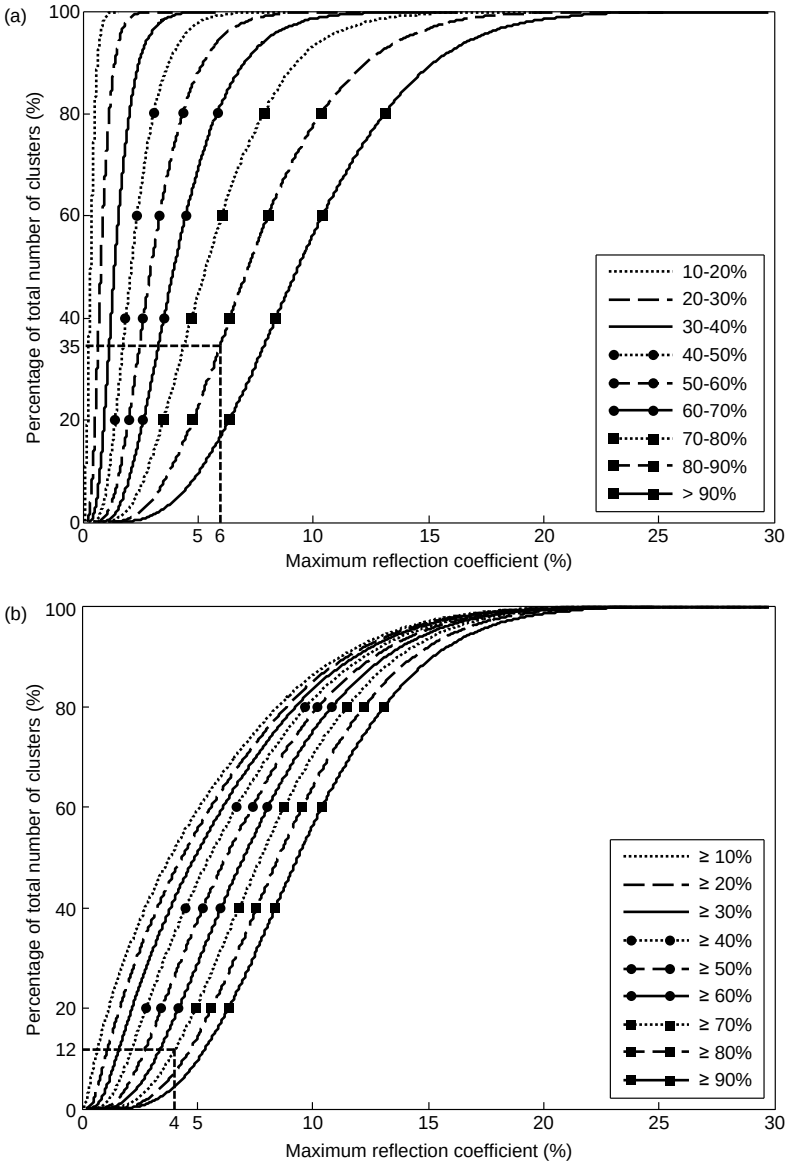

Figure 5.8: Percentage of clusters with a maximum RC less than the values of the abscissa. The pit clusters are developed within a circular defect domain with circumferential and axial extents of $d_{\text{circ}} = d_{\text{ax}} = 2\pi r_{\text{pipe}}/4$. (a) Maximum pit depth intervals of 10% as indicated in the legend. (b) Maximum pit depth greater than the thresholds indicated in the legend.

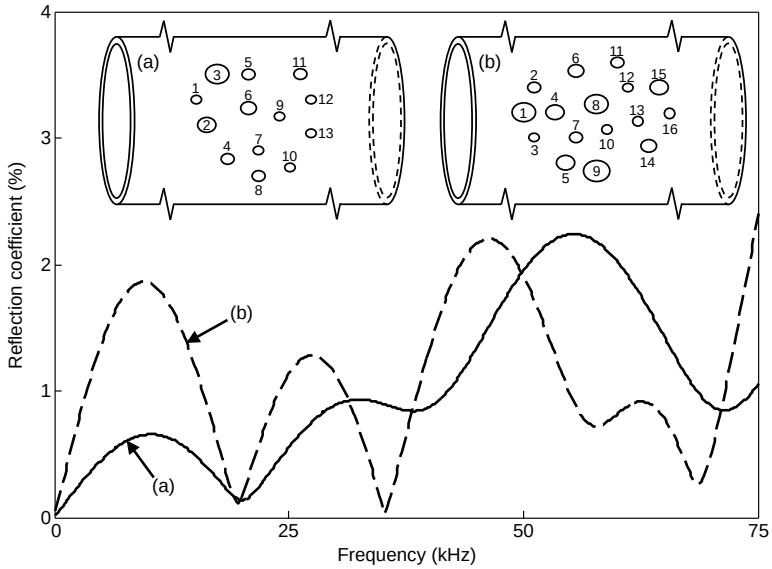

Figure 5.9: Typical problematic cluster morphologies. Reflection coefficients for two example clusters are shown as function of frequency. The figure insets show the corresponding example pit clusters; the corresponding pit depths and diameters are given in table 5.1.

Table 5.1: Details of example problematic morphologies shown in figure 5.9.

Pit cluster (a)			Pit cluster (b)		
Pit no.	Pit diameter	Pit depth (%)	Pit no.	Pit diameter	Pit depth (%)
1	$1t$	20	1	$2.25t$	20
2	$1.75t$	10	2	$1.25t$	30
3	$2.25t$	10	3	$1t$	70
4	$1.25t$	20	4	$1.75t$	50
5	$1.25t$	10	5	$1.75t$	10
6	$1.5t$	20	6	$1.5t$	50
7	$1t$	40	7	$1.25t$	20
8	$1.25t$	10	8	$2.25t$	40
9	$1t$	30	9	$2.5t$	10
10	$1t$	20	10	$1t$	30
11	$1.25t$	10	11	$1.25t$	30
12	$1t$	10	12	$1t$	90
13	$1t$	90	13	$1t$	70
			14	$1.5t$	20
			15	$1.75t$	40
			16	$1t$	20

corresponding pit depths and diameters are given in table 5.1. Most of the pit clusters with large maximum cluster depth and low maximum RC result from layouts similar to the one shown with solid line in (a). As can be seen from table 5.1, the cluster layout consists of many pits, but most are quite shallow and/or small, with one deep pit of diameter $1t$ (pit 13 in this case). Such single, small through-thickness pits are improbable from a practical corrosion morphology point of view [109, 110, 112], which is encouraging for practical guided wave testing, as isolated pits are very difficult to detect. Layout (b) is more problematic in that the pit cluster consists of several rather deep pits (in addition to some shallower ones), but still the maximum RC within the bandwidth covered is less than 3%. This is due to destructive interference between pits in the cluster, and also the limited bandwidth inherent in practical guided wave testing as it is clear from figure 5.9 that the maximum RC would be higher with a slightly larger bandwidth. Evidently, constructive or destructive interference between the reflections from different parts of a corrosion patch affects the total RC. Cluster size and shape compared with the wavelengths included within the frequency range of the interrogating signal governs the extent of interference.

The results reported in figures 5.7–5.9 are all with a circular defect domain of size $d_{\mathrm{ax}} = d_{\mathrm{circ}} = 2\pi r_{\mathrm{pipe}}/4$, which implies a 1:1 ratio between the axial and circumferential extents of the defect domain. Figure 5.10 shows the percentage of clusters with maximum RC less than the values of the abscissa for elliptical defect domains with axial to circumferential ratios of 1:2 and 2:1 as shown in solid and dotted lines, respectively. The same defect domain grid size of $dx = dy = 1t$ was used. As the defect domain is smaller than that discussed in Section 5.2, the lowest number of growth steps that may leave no valid growth step remaining is reduced to 63. Thus, random pit development steps from 1–63 steps were used. Consequently, less volume is on average removed from the pipe compared with the defect domain with circular shape discussed above, so the percentage of clusters with a given maximum depth that result in a certain maximum RC presented in figure 5.10 cannot be directly compared to those in figure 5.8.

As can be seen from figure 5.10, the clusters developed within an elliptic defect domain shape with longer axial than circumferential extent give somewhat larger maximum RC. The axial lengths of the two elliptic cluster layouts are approximately 45 and 90 mm. For the T(0,1) mode half-wavelengths of 45 and 90 mm correspond to frequencies of 36 and 18 kHz, respectively. As successive peaks occur at separation distances of $L_{\mathrm{sep}}/\lambda = \eta/2$ between two axially separated holes, where η is a counter variable, constructive interference between reflections from single pits within the cluster will be more frequent with an axial to circumferential ratio of 2:1 rather than 1:2 within this frequency range and cluster size. RCs are known to increase linearly with the total circumferential extent of defects at a given axial location [7, 11, 25], but in this case the increased possibility of constructive interference between pits due to their

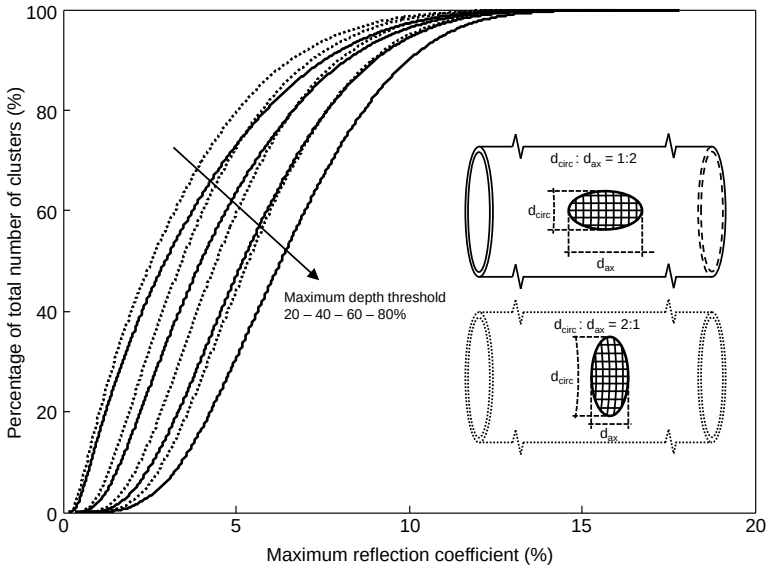

Figure 5.10: Percentage of clusters with a maximum RC less than the values of the abscissa for elliptical shaped pit clusters. Results with defect domains with circumferential and axial extents of $d_{\text{circ}} : d_{\text{ax}} = 1{:}2$ and 2:1 are shown in solid and dotted lines, respectively, as indicated in the insets. Results for maximum pit depth thresholds of 20, 40, 60 and 80% of the pipe wall thickness are included, corresponding to curves from the left to right, as indicated by the arrow.

axial separation with a defect domain shape of $d_{\text{circ}} : d_{\text{ax}} = 1{:}2$ compared with $d_{\text{circ}} : d_{\text{ax}} = 2{:}1$ outweighs the increasing possibility of more and/or larger pits present at the same axial location, which is the case with larger circumferential than axial extent, as seen from figure 5.10. Similar trends were also found with elliptic defect domain shapes of 3:1 and 1:3.

Tapered pit cluster results

The calculations of maximum RC from pit clusters reported above are all based on flat bottomed circular pits with straight sides, as indicated in figure 5.3. As seen from the previous subsection, a certain number of cluster layouts with deep pits would not be detected due to their small maximum RC. Most of the problematic cases were clusters with single, relatively small, deep pits, which from a corrosion morphology point of view are relatively unlikely to develop [109, 110, 112], but also clusters with several rather deep pits were not called due to destructive interference between the various pits present. However, pits are likely to be part of a larger, broader attack [2], and are thus surrounded by

areas of significant wall loss in which the pits are the deepest parts. The latter is especially true for mild and low-alloy steels [109], which includes carbon steels. To accommodate this feature, the pit clusters were superposed on a circular cosine tapered defect with diameter $2\pi r_{\mathrm{pipe}}/4$ on the outer surface of the pipe.

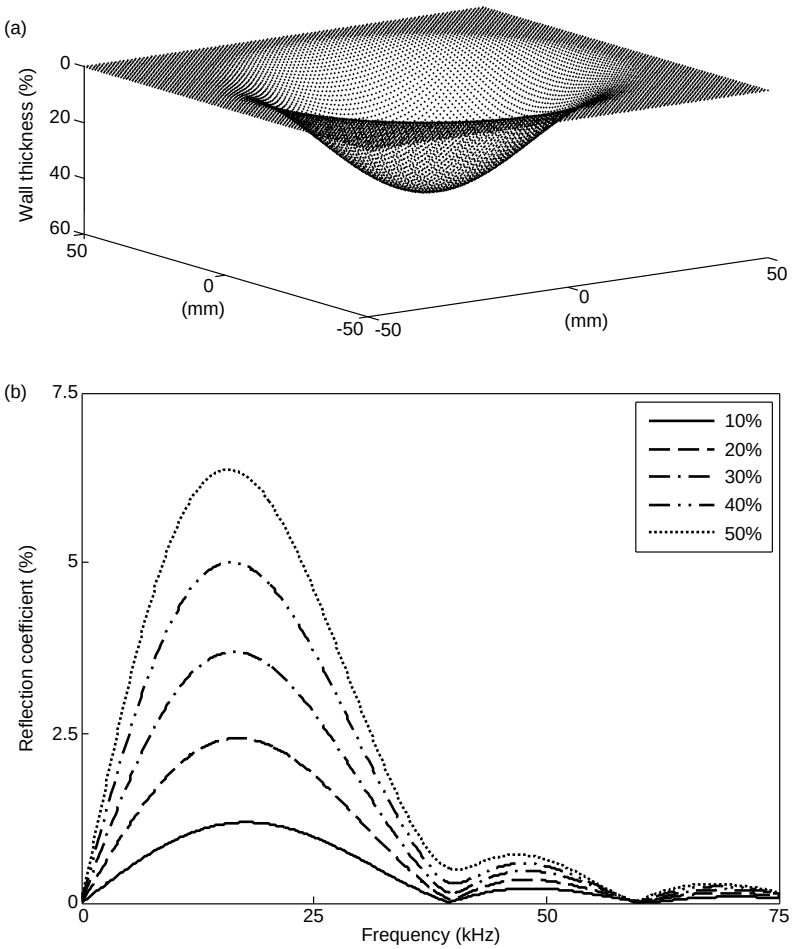

Figure 5.11: (a) Example 40% deep cosine taper shown in a plate. (b) Variation of RC with frequency for cosine tapered defects of depths 10–50% of the pipe wall thickness.

Figure 5.11 (a) shows an example cosine taper of depth 40% of the wall thickness. The geometry is shown straightened out onto a plate for clarity, but all simulations were done on the same 4 in. schedule 40 pipe as with the pit clusters growing out of areas otherwise affected by general corrosion only discussed in the previous subsection. Figure 5.11 (b) shows RCs as a function of

frequency for cosine tapered defects with diameter $2\pi r_{\text{pipe}}/4$ and depths of 10, 20, 30, 40 and 50% of the pipe wall thickness, as indicated in the figure legend. The RCs can be seen to scale approximately linearly with defect depth, with the maximum RC occurring at $L = \lambda/4$, where L is $2\pi r_{\text{pipe}}/4$, in accordance with earlier studies of single defects [11, 17].

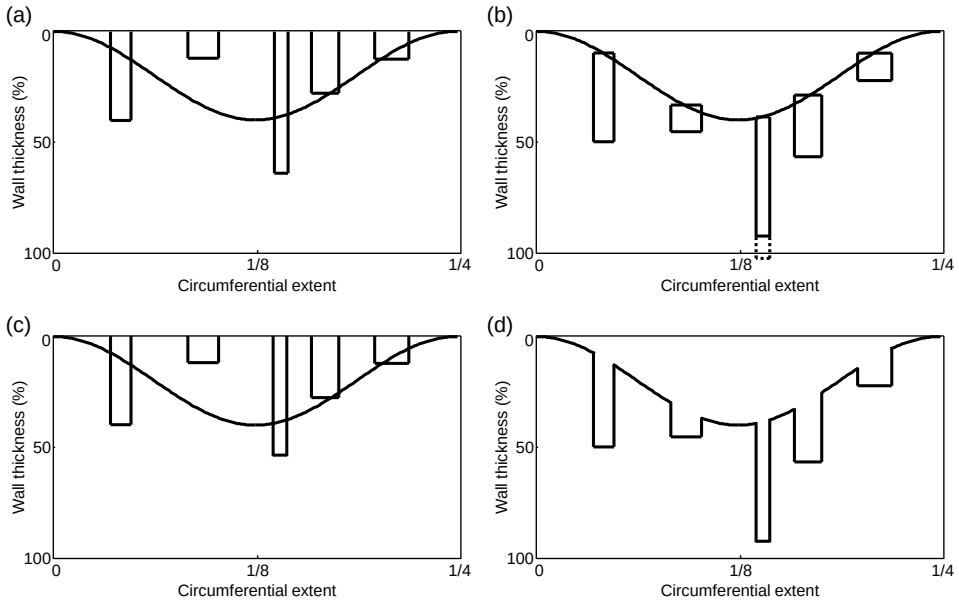

Figure 5.12: Cross-section through the centre of an example cluster domain to illustrate the construction of tapered defect clusters using superposition and full solution. The pipe curvature is not included in the figure. (a) Initial cosine taper and separate cylindrical pits. (b) Shifting of pits to the depth of cosine taper at the centre of the pit; pit depths are reduced in steps of 10% of the total depth exceeds pipe wall thickness (indicated in dotted lines). (c) Defects whose reflections are added to compute the total RC using superposition. (d) Corresponding full solution layout.

Figure 5.12 shows the approach used to superpose the randomly generated pit clusters onto the cosine taper, where the cross section through the centre of an example cluster domain is used as illustration. Firstly, random defect clusters were generated in the same way as done in the previous subsection; with a random number of pit development steps in the range from 1–126, employing the single pit growth scheme shown in figure 5.3 with equal probability of pit growth in depth or width at each growth step. The initial cosine taper and example pits are shown in figure 5.12 (a). The pits are then shifted in depth to the depth value of the cosine taper at the given location, as shown in figure

5.12 (b). Any pits that exceed the pipe wall thickness after being shifted, are reduced in depth in steps of 10% of the pipe wall thickness until their depth is within the pipe wall thickness, as indicated in dotted lines for one example pit in figure 5.12 (b). Figure 5.12 (c) shows the total tapered pit cluster as it is implemented using superposition, while figure 5.12 (d) shows the corresponding full solution.

To be able to run a large number of random clusters, use of superposition is a necessity. In applying superposition with a cosine taper, it is assumed that the RC from each pit is proportional to the volume removed, from which it follows that the mode shape of the T(0,1) mode is constant through the pipe wall thickness, and all pits give the same reflection regardless of their position through the thickness of the pipe. Thus, the individual pits shifted up to the outer surface of the pipe, as shown in figure 5.12 (c), will give the same reflection as those shown in figure 5.12 (b). Also, as is evident from figure 5.12 (b), the pits will not fit perfectly onto the cosine taper as they are simply shifted down onto the cosine taper using the centre point of each pit. This error is also inherently accepted in the superposition calculations; its severity depends on the gradient of the taper, and will thus be larger with increased depth of the taper, and also vary with the locations at which pits develop within the cosine taper area.

Figure 5.13 shows a comparison between superposition and full solution calculations for two cases, both with a cosine taper of depth 40% of the pipe wall thickness. In (a) a single pit with diameter $2t$ and depth 60% of the pipe wall thickness is used. With the full solution, when the pit is superposed on the cosine taper, the total pit depth is 77.7% of the pipe wall thickness, as the depth of the cosine taper at that specific location is 17.7%. The solid, dashed and dotted lines show the RC as a function of frequency for the full solution, superposition and cosine taper only, respectively. The single pit can be seen to mainly influence the RC at frequencies from around 35 kHz upwards, as the RCs are comparable at low frequencies in all cases. The agreement between the full solution results and superposition is good, with slightly larger error at higher frequencies due to the approximations made. In this example, the pit is placed roughly where the cosine taper changes most rapidly in depth, which is where the error due to mismatch between the pit and the cosine taper (as shown in figure 5.12 (b)) will be largest.

Figure 5.13 (b) shows a comparison between full solution (solid line) and superposition (dashed line) for a pit cluster consisting of 14 pits of various depth and size. The agreement between the full solution and superposition is seen to be quite good throughout the frequency range. There is a significant error at about 70 kHz, but the main features of the RC are obtained, and most importantly both the local and global maxima show good agreement. Thus, the use of superposition with cosine tapers is validated within acceptable accuracy.

As for pit clusters without a cosine taper present as shown in figure 5.8 (b), figure 5.14 shows the percentage of clusters with a maximum RC less than

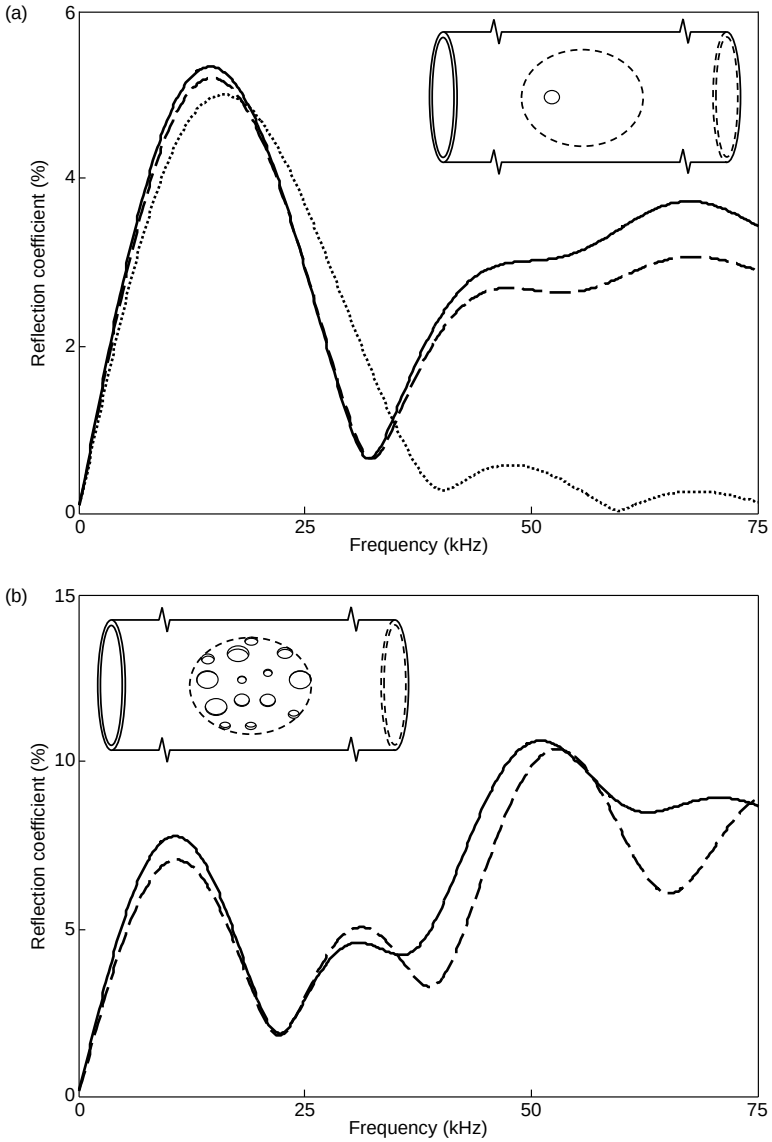

Figure 5.13: Variation of the RC with frequency for (a) a single pit in addition to a circular cosine taper of depth 40% of the pipe wall thickness, and (b) a pit cluster consisting of 14 randomly spaced and sized pits in addition to the cosine taper. The cluster is shown in the figure inset, where the tapered area is indicated by the dashed circle. Results with full solution and superposition are indicated with solid and dashed lines, respectively, while the RC from the tapered area only is shown by the dotted line in (a).

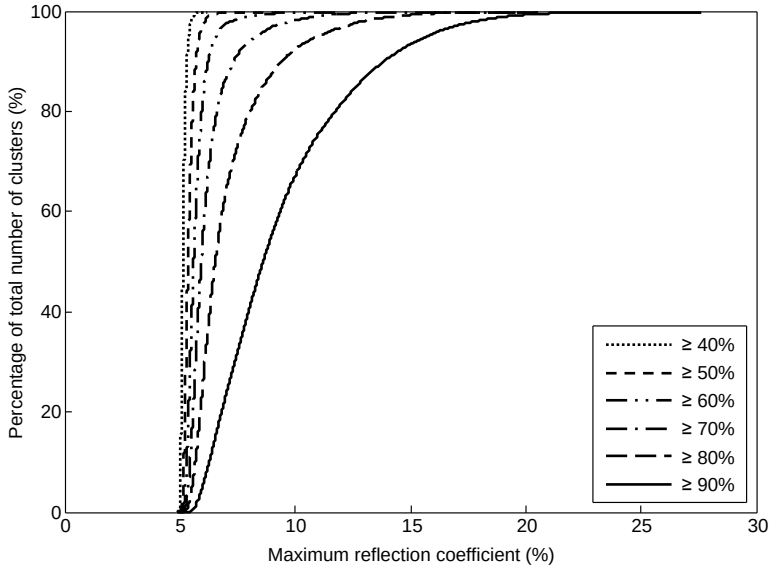

Figure 5.14: Percentage of clusters with a maximum RC that is less than the values of the abscissa for circular cosine tapered pit clusters with taper depth of 40% of the pipe wall thickness. Results for maximum defect depths deeper than, or equal to, 40–90% are shown, as indicated in the figure legend.

the values of the abscissa for pit clusters with maximum depths deeper than the thresholds given in the figure legend. Pit clusters are developed within a circular domain and superposed onto a cosine tapered defect of depth 40% of the pipe wall thickness and with the same axial and circumferential extents as the pit cluster domain. The calculations are based on a series of 100,000 randomly generated pit clusters. The RC from a cosine taper of depth 40% alone is shown in figure 5.11 (b), with a maximum RC of approximately 5%. Accordingly, the maximum RC due to the cosine taper is in figure 5.14 seen to be a lower bound for the maximum RC with the pit clusters included. As can be seen from figure 5.11 (b), the maximum RC from the cosine taper alone occurs at around 18 kHz, at which the cosine taper size $d_{\mathrm{ax}} = 2\pi r_{\mathrm{pipe}}/4$ corresponds to $\lambda/4$ for the T(0,1) mode. At such low frequencies, the interrogating signal will not see the pits separately, but as parts of the larger cosine taper defect, which increases the low frequency RC. This was also seen in the RC from the pit cluster in figure 5.13 (b). At higher frequencies, the individual pits will interfere with each other, with increased probability of a higher maximum RC occurring as the cluster develops; even if the pits interfere destructively with each other, the RC from the cosine taper will still ensure a maximum RC of around 5%, as figure 5.14 shows.

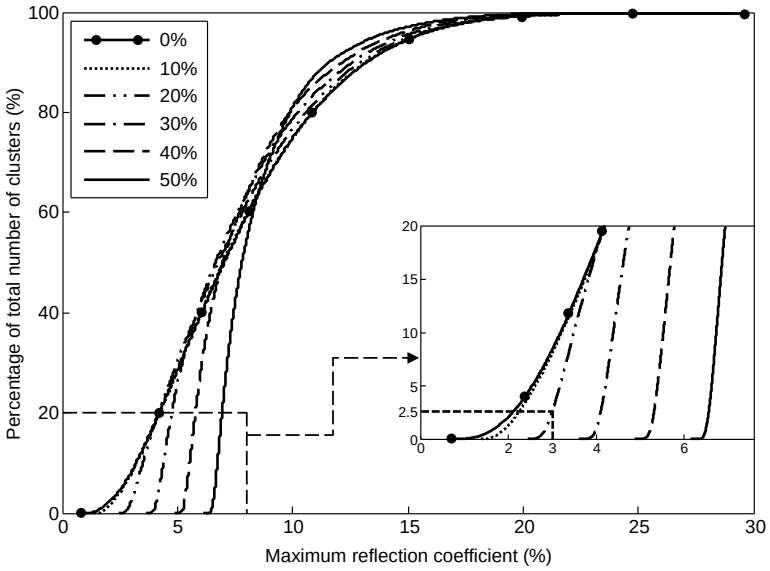

Figure 5.15: Percentage of clusters with a maximum RC that is less than the value of the abscissa for pit clusters with maximum defect depth deeper than, or equal to, 60% of the pipe wall thickness. Pit clusters with cosine tapers of depths 10–50% of the pipe wall thickness are included, while the solid line with circular markers shows results for clusters without tapered area.

The cosine taper used in the calculations shown in figure 5.14 was 40% deep. Similarly, percentages of clusters with maximum depth exceeding certain thresholds as a function of maximum RC were also calculated for pit clusters with various depths of the underlying cosine taper. Figure 5.15 shows results for pit clusters with maximum RC less than the values of the figure abscissa for clusters with maximum defect depth deeper than, or equal to, 60% of the pipe wall thickness. The pit clusters are randomly generated and superposed onto cosine tapers of depth 0 (no taper) 10, 20, 30, 40 and 50% of the pipe wall thickness, as indicated in the figure legend. In each case 100,000 randomly developed clusters were used in the calculations. The number of pit clusters resulting in maximum RCs larger than approximately 8% is comparable regardless of cosine taper depth for all the cases investigated, which suggests that the cosine tapers have little effect on the largest maximum RCs in these cases, while the influence of the taper tends to increase the smallest RCs obtained. This is because large maximum RCs are generated by constructive interference between the pits in a cluster, while if there is destructive interference, the reflections from the individual pits cancel out, leaving just the effect of the taper. In the latter cases, the maximum RCs drops towards the maximum RC of the cosine

tapers alone (see figure 5.11 (b) for maximum RC for the cosine tapers). The shallower the taper, the more the maximum RCs approach the results found with pit cluster only; with cosine taper depth of 10%, only a slight deviation from the results with pit clusters without the cosine taper is seen. The figure inset highlights the 20% of the pit clusters resulting in the lowest maximum RCs, from which it can be seen, for example, that almost all pit clusters with maximum depth 60% of the pipe wall thickness with cosine taper depth of 30% or deeper give a maximum RC above 4%. Likewise, with a 20% deep cosine taper, approximately 2.5% of the pit clusters with maximum depth 60% result in a maximum RC below 3%, as is indicated by dashed lines in the figure inset.

Thus, with realistic pit clusters, normally resulting in maximum RCs from 3–4% upwards, ultrasonic guided wave testing has been shown to have a high probability of detecting clusters before they penetrate through the wall thickness. Single, small and deep pits may not result in a sufficiently high RC to be detected at the low frequencies used in most practical guided wave testing. However, as pits typically tend to grow faster in width than in depth when they are in the millimetre scale [109, 110], commonly occur in clusters of multiple pits [109, 112], and are part of a larger, broader attack [2], the detectability is good.

5.4 Experimental validation

Experiments were conducted on two 3 m long 4 in. nominal bore schedule 40 steel pipes (outer diameter 114.3 mm, wall thickness 6.0 mm) to validate the FE predictions. Figure 5.16 shows the experimental setup.

The pipes were tested horizontally while resting on wooden supports which produced negligible reflections. Two transducer rings from Guided Ultrasonic Ltd. [10], with a total of 32 and 96 piezoelectric transducers, respectively, were used to cover the larger part of the frequency range employed in the FE simulations; covering a higher frequency range requires more transducers [114]. Each ring is divided into two rows of equally spaced transducers, in order to be able to distinguish the direction from which a reflection originates [115]. A total frequency range of 25–75 kHz was covered by the two rings, the excitation being a succession of 8 cycle Hanning windowed tonebursts of different centre frequencies generated by a Guided Ultrasonics Ltd. G3 Wavemaker [10] instrument. Each transducer ring was clamped on the external wall of the pipe to excite and receive the T(0,1) mode in both directions in the pipe as the piezoelectric transducers applies alternating forces in the circumferential direction.

Two pipes were used in the experimental work, of which one had an ellipsoidal defect (axial and circumferential extent 26 and 21 mm, respectively, with maximum depth 75% of pipe wall thickness), already machined into it for other tests. Figure 5.17 shows layout B as it was machined into the pipe, and also the ellipsoidal defect further along it. Because of the presence of this ellipsoid, two different measurement setups were needed, as shown in figure 5.16. Figure

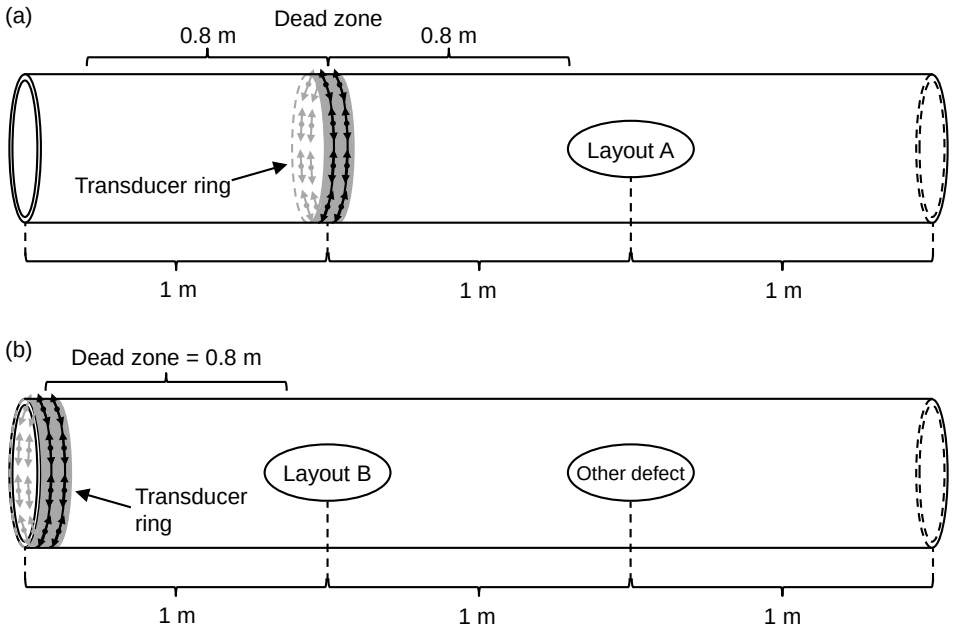

Figure 5.16: Schematic of experimental setup.

5.16 (a) shows the setup used to measure the reflection from layout A, where the reflection from the left hand end of the pipe acts as reference. In figure 5.16 (b) the right hand end was used as reference, introducing a small error in the experimental results as the incident wave and reference reflection produced necessarily need to propagate through both the cluster layout investigated (layout B) and the ellipsoidal defect already present in the pipe. The reduction in amplitude of the T(0,1) mode as it passes through the ellipsoidal defect and cluster twice before reaching the transducer ring again was predicted by FE analysis to be less than 7% of the incident amplitude for all frequencies of interest. This error introduced by using the amplitude of this reflection as the reference signal was therefore modest.

In order to avoid the dead zone of the rings, a distance to the cluster layouts (and the reference left pipe end for the setup shown in figure 5.16 (a)) of around 0.8 m was employed. The pit clusters in layouts A and B were drilled at 1 m distance from the right hand end of pipe (a) and the other defect present in pipe (b), respectively, in order to separate their reflections. RCs were calculated in the time domain as peak-to-peak amplitude ratios between the reflections from the pit clusters and the reference end reflection. Up to 16 averages were employed in each measurement, and a signal to noise ratio between the reflection from the defect(s) and the background noise greater than

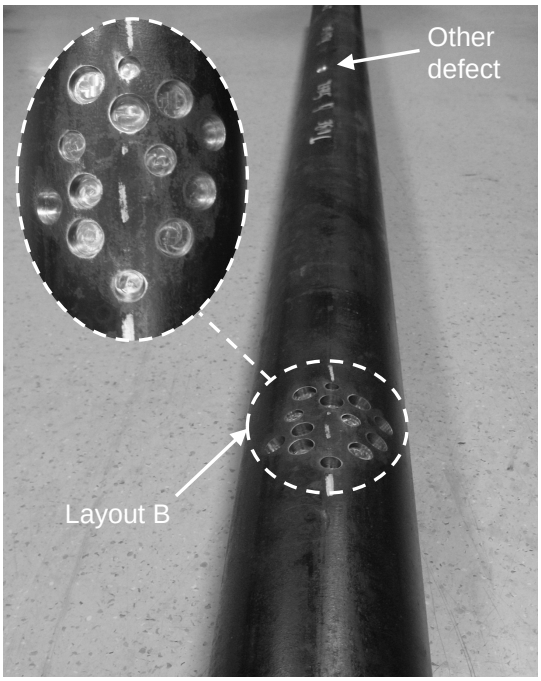

Figure 5.17: Cluster machined into pipe (b) of figure 5.16, where also the other defect already machined into the pipe further along it is seen.

2 dB was required for the results to be used.

Figure 5.18 shows comparisons between full solution FE calculations (solid lines), superposition results based on single pit FE simulations (dashed lines), and experiments (markers), where the figure insets indicate the pit cluster layouts; the corresponding pit depths and diameters are given in table 2. The two pit clusters discussed are two worst case clusters, where the deviation between full solution and superposition is the largest amongst the cases validated. The pit cluster in (a) is the cluster with the largest discrepancy between the full solution and superposition (10% difference in maximum RC) of the cases of Section 5.2. The cluster consists of 16 pits, where the maximum pit depth is 70% of the pipe wall thickness, while seven pits are in the range from 40–60%. Despite this being a relatively developed pit cluster, very good agreement between the full solution and superposition is seen in general, with increasing error towards higher frequencies, as mentioned. The experimental results showed reasonable agreement with the FE analyses, maintaining the main shape of the RC and with comparable maximum RC.

Figure 5.18 (b) shows a pit cluster consisting of many deep, closely situated pits of the largest size ($d = 2.5t$). The cluster consists of 13 pits in total, of

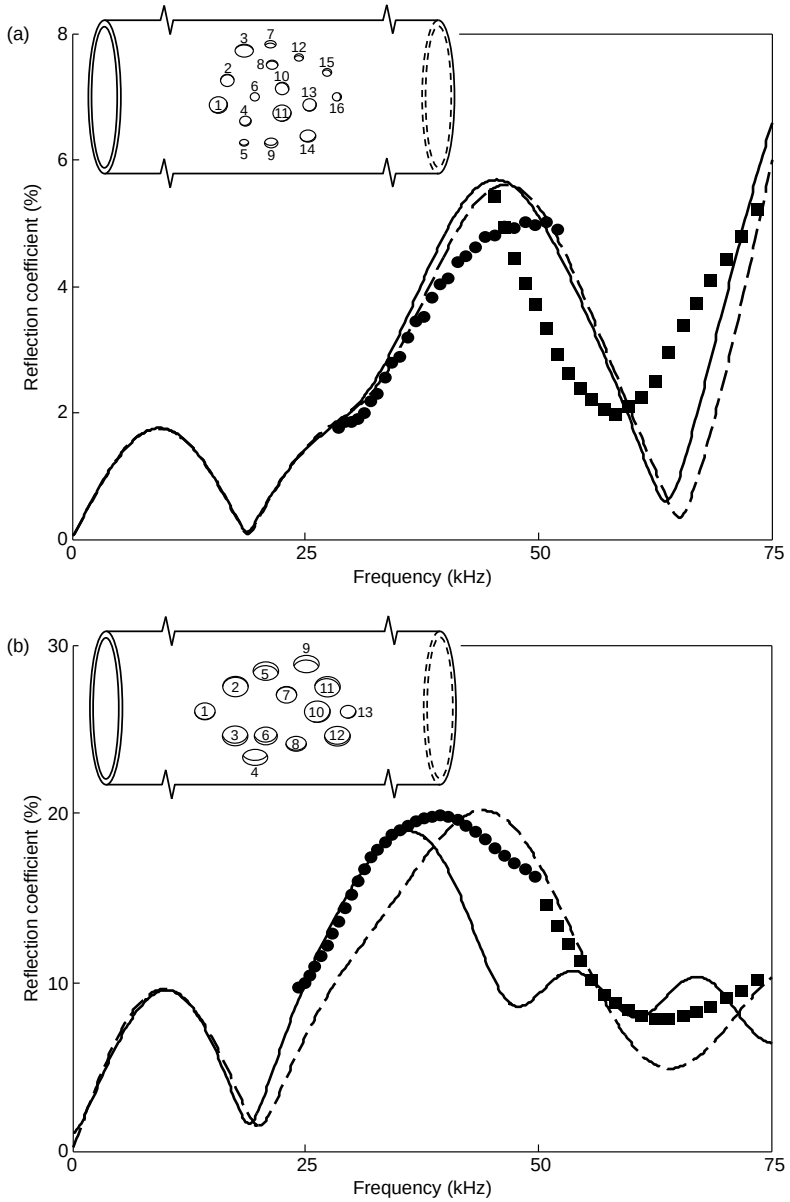

Figure 5.18: Comparison between full solution FE (solid lines), superposition calculations (dashed lines) and experiments (results obtained with the low and high frequency rings are indicated by • and ■, respectively). Defects layouts are shown in the figure insets; the corresponding pit depths and diameters are given in table 5.2.

Table 5.2: Details of cluster morphologies for experimental validation, as shown in figure 5.18.

Pit cluster (a)			Pit cluster (b)		
Pit no.	Pit diameter	Pit depth (%)	Pit no.	Pit diameter	Pit depth (%)
1	$2t$	70	1	$2t$	90
2	$1.5t$	20	2	$2.5t$	40
3	$2t$	10	3	$2.5t$	80
4	$1.25t$	30	4	$2.5t$	90
5	$1t$	20	5	$2.5t$	90
6	$1t$	10	6	$2.25t$	90
7	$1.25t$	40	7	$2t$	30
8	$1.25t$	30	8	$2t$	30
9	$1.5t$	50	9	$2.5t$	90
10	$1.5t$	50	10	$2.5t$	90
11	$2t$	20	11	$2.5t$	90
12	$1t$	40	12	$2.5t$	60
13	$1.5t$	40	13	$1.5t$	60
14	$1.75t$	20			
15	$1t$	60			
16	$1t$	50			

which eight are 80% of the pipe wall thickness or deeper; five are of the largest size included and 90% deep. The validity of superposition can be seen to start to break down from around 25 kHz upwards, but still the main shape of the RC is seen and, most importantly, the maximum RC is comparable. Results from the experimental tests are in good agreement with the FE analyses; some discrepancy can be seen around 40–50 kHz, but the shape and extreme values show good agreement.

5.5 Conclusions

A study of the reflection of the fundamental torsional mode, T(0,1), from randomly generated pit clusters has been reported. The work has been done by FE simulations of all single defect types separately, and subsequent superposition with the appropriate delays to account for their respective positions on the pipe. Full FE analyses have been carried out to verify the validity of employing superposition, and experimental validation has been done for two cases.

The maximum reflection coefficient (RC) from pit clusters was found to be a linear function of the total volume fraction removed, but with very significant scatter due to interference between axially separated pits. Randomly generated pit clusters within a domain of diameter $2\pi r_{\text{pipe}}/4$ were investigated initially, and the percentage of them giving a maximum RC less than certain values was

calculated. Analyses indicated that most defect clusters with high maximum depth result in a maximum RC of 3–4% or higher before they propagate fully through wall. Detailed analyses of typical problematic cases that gave small maximum RC values revealed that most of the clusters that resulted in small maximum RCs were due to single, small and deep defects in otherwise relatively shallow and lightly populated clusters. Despite such cluster morphologies being improbable in practice, some cases do occur and are likely to be missed by guided wave testing; in a few cases, destructive interference between pits in clusters consisting of several larger pits that were axially spaced relative to each other resulted in small maximum RCs.

More commonly pits are part of a larger, broader attack, with several pits of comparable depth in the pit cluster. Pit clusters superposed on cosine tapered defects were investigated to represent this case. With pit clusters being part of a larger attack, rather than growing in regions otherwise unaffected by corrosion, the cosine tapers alone were a lower bound for the maximum RC from the total cluster layouts; for example no pit clusters with maximum depth $\geq$60% of the pipe wall thickness resulted in a maximum RC below 4% with cosine taper depth of 30% or deeper. This reduces the probability of deep defects not being detected.

With pit clusters superposed onto cosine tapered defects, the maximum RC from the cosine tapers alone occurred at $L = \lambda/4$, as expected, while the additional reflections from the pits only to a small extent affected the RC at such low frequency; the RC at higher frequencies was found to depend heavily on the morphology of the pit cluster. This supports the suggestion given in chapter 4, that guided wave testing preferably should be done employing a wide frequency range, which to some extent will be limited by the transducer ring(s) used in practice.

Chapter 6

The influence of sharp edges in corrosion profiles on the reflection of the fundamental torsional guided wave

This chapter discusses the relationships between reflection coefficients and geometrical properties of corrosion profiles, where special attention is given to the influence of sharp edges in the corrosion profiles. Understanding these relationships is of paramount importance in the interpretation of realistic inverse problems encountered in practice; the assessment of the maximum defect depth being the most important parameter. The direct motivation and background for the study is work presented in chapters 4 and 5 (which is the basis of [25, 33]), and also recent work done by Carandente et al. on the reflection from complex defect profiles [116, 117].

Initially, a discussion on the complex and random processes of localised corrosion is provided in Section 6.1, before the finite element (FE) model used in the simulation analyses throughout the chapter is outlined in Section 6.2. Section 6.3 employs a two-dimensional fast Fourier transform (FFT) approach to investigate the dependence between the spatial frequency content of corrosion patches and the reflection from them; the properties of the method are firstly outlined before it is applied to a selection of corrosion profiles ranging from relatively simple axisymmetric defects to real corrosion profiles. Then the validity of representing pit clusters as single, complex defects is assessed in Section 6.4. Experimental validation of one of the corrosion profiles discussed in Section 6.3 is presented in 6.5, before conclusions are made in Section 6.6.

The work in this chapter was partly done in collaboration with Dr Carandente who finished her Ph.d. at Imperial College, London [118] in November 2011. Specifically, the processing algorithms and FE modelling in Section 6.3 were developed in collaboration, while the processing of the real corrosion pro-

file in Section 6.3 and the experimental work in Section 6.5 was done solely by Dr Carandente in the Imperial College laboratory. The work presented in this chapter is included in a paper submitted to NDT&E International [34], except for the short discussion on cosine tapered pit clusters in Section 6.3 and on their representation as a single defect, which is given in Section 6.4.

6.1 Introduction

Corrosion, and the control and management of it, remains a major operational obstacle in securing the integrity of pipelines in the petrochemical industry [1]. Carbon and low-alloy steels are relied heavily upon as pipeline material, which are vulnerable to localised corrosion attacks primarily caused by the presence of CO_2 and H_2S [3]. The corrosion community groups localised corrosion attack either according to the cathodic reaction causing it, or most commonly, according to their visual appearance, as it allows quick, in-situ assessment; the electrochemical reason for their development may also be unknown or unclear [6]. A variety of electrochemical prediction models exist [119]; however, localised corrosion remains an insidious and unpredictable risk factor to the integrity of pipelines in the oil and gas industry.

From a non-destructive testing (NDT) point of view, the scatter and randomness in size, shape, location, growth rate and maximum depth of localised corrosion [2, 4] requires an increased understanding of the relationship between the geometrical properties of corrosion patches and the resulting reflection coefficient from them for correct interpretation and evaluation. The most important parameter in NDT is the maximum defect depth, which is closely related to the time to perforation, and cannot be extracted from measurement results without sufficient knowledge of how geometrical properties of defects affect and are related to the RC. Many researchers have contributed to the understanding of the reflection and scattering of guided waves from relatively simple-shaped corrosion attacks in pipes, such as straight cracks, holes, notches and supports [7, 9, 11, 12, 14–21, 23]. These shapes can sometimes be very good approximations of shapes observed in real corrosion patches, in addition to adding to the fundamental understanding of relationships between defect shape and scattering of the incident guided wave. Recently, also as a consequence of the comprehensive work done with defect of simple shapes, attention has been given to the estimation and scattering from complex corrosion patches [116, 117]. Some of the defects analysed in [116] will be further analysed here.

This chapter aims to assess the influence of sharp edges in corrosion profiles on the reflection of the incident guided wave, and is motivated by the need to understand how the RC spectrum is related to the spatial frequencies of the corrosion patch, which is essential in interpreting practical testing results. Previous studies have revealed that the estimation of maximum defect depth of pit clusters or corrosion patches is a difficult task that depends on a variety of parameters; especially in cases with sudden changes in depth within a small

area of the corrosion patches, where errors in the maximum depth estimation occur [33, 117]. A two-dimensional FFT analysis is employed here to aid in the understanding of the RC from a selection of defect cases. By decomposing the geometries in the spatial frequency domain, the effect of the various spatial components of the defect on the RC from the cluster is discussed. The corrosion profiles are filtered in the wavenumber domain, to separate the low and high spatial frequency content of the profiles. By employing a superposition technique, the sum of RCs calculated from the low and high spatial frequency profiles is compared with the original profiles, the validity limits of which will be discussed.

Following the analyses using the 2D FFT approach, an analysis of whether pit clusters can be represented as a single, complex defect is presented. The idea is based on the difficulty experienced in resolving multiple pits and/or other features within complex corrosion profiles in practical inspection situations, as seen in Chapter 5. The validity of such an approach will be evaluated by comparing the RC of the single defect representations with that of the corresponding pit clusters. If a cluster of pits can be well represented by a single, generalised corrosion defect, and results in comparable reflection coefficients, then the maximum depth estimation methodology presented by Carandente et al. [117] can be employed.

6.2 Finite element model

Full 3D FE models were employed throughout the FE analyses in this chapter, modelling a 4 in. nominal bore schedule 40 pipe (outer diameter 114.3 mm, wall thickness 6.02 mm) in the commercially available software program ABAQUS, version 6.9 [74]. The fundamental torsional mode, T(0,1), was excited by applying a Hanning windowed excitation toneburst as tangential displacements at 90 evenly spaced nodes around the outer circumference of the pipe, as shown in figure 6.1. Signals were calculated in the time domain by adding the tangential components according to equation 4.1.

The pipe length, location of receiver positions and defect location were chosen so that the incident and reflected signals could be well separated. In Section 6.3 model convergence was achieved by using linear tetrahedral elements with element length 1.5 mm, and time steps in the range from 50–100 ns, exciting a 2-cycled Hanning windowed toneburst with a centre frequency of 70 kHz. These quantities were slightly refined in Section 6.4 by employing quadratic tetrahedral elements with the same element size, resulting in an approximate nodal separation of 0.75 mm, which required the time step to be refined to 10 ns for the models to run appropriately. As discussed in Section 2.5 and [76], it is not the traditional rule of a given number of elements per shortest wavelength that governs the mesh size in these cases, as even finer mesh resolution is required in order to model the geometrical properties of the defects satisfactorily.

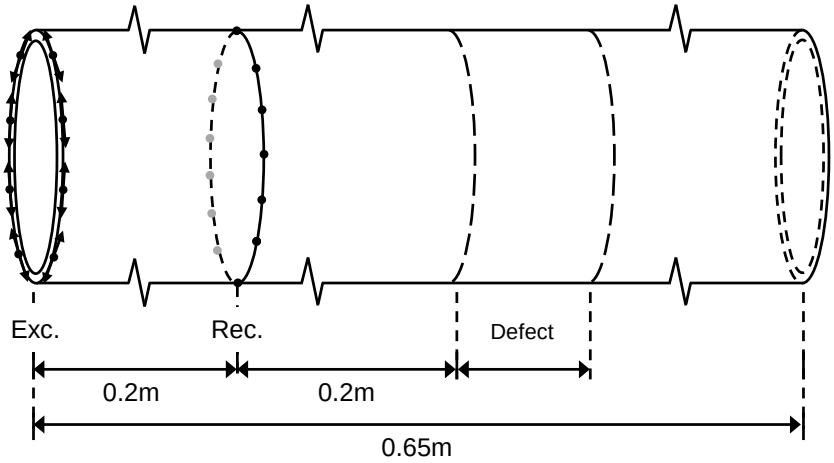

Figure 6.1: Schematic of finite element models. Excitation and reception in the circumferential direction at the outer nodes of the pipe as indicated. Defect region placed to ensure sufficient separation between incident and reflected waves at the receiver location.

RCs were calculated in the frequency domain, and are defined as the ratio of the surface circumferential displacement amplitude of the reflection to that of the incident wave.

6.3 Defect analysis using two-dimensional FFT

A two-dimensional FFT approach is used to assess how the spatial frequency content of corrosion patches is related to the RC from them, which is based on the idea that a periodic function can be broken into its harmonic components and resynthesized by adding together the harmonic components. Corrosion maps are transformed into the spatial frequency domain, where cosine tapered low and high pass filters are employed. Subsequently, an inverse two-dimensional FFT transformation is done before calculating the RCs from the filtered corrosion patches consisting of the low and high spatial frequency components separately, and comparing them to the RC from the original corrosion map and also to the superposition of the RCs from the two filtered maps.

Filtering the corrosion map into patches consisting of low and high spatial frequency components, and evaluating the RC from them individually implicitly assumes that the wavenumber components can be evaluated independently. This approach benefits from the first order Born approximation and neglects the interaction between different parts of the corrosion patch. Gubernatis et al. derived an integral equation describing the exact scattering field of a plane wave

from a single homogeneous defect in their paper [62], which may be written in indicial notation [71] as

$$u_i^{tot} = u_i^{inc} + u_i^{sc}\left(u_i^{tot}, \varepsilon_{ij}^{tot}\right), \tag{6.1}$$

where the scattered field, u_i^{sc}, is dependent on the displacement (u_i^{tot}) and strains (ε_{ij}^{tot}) within the corrosion patch. Equation 6.1 may be rewritten as an iterative approximation that is initialised by the incident wave itself, as described in a subsequent paper by Gubernatis et al. [63]. By only performing the first order iteration, the exact displacement and strain fields inside the corrosion patch is replaced by the incident wave fields, which implies that the scattered field must be comparatively weak [64].

The validity of applying the Born approximation is thus crucial to the accuracy of the two-dimensional FFT analyses, which depends not only on the contrast the corrosion patch represents relative to the surrounding medium, but also to its size relative to the wavelengths of the interrogating signal [91, 120]. For the first order Born approximation to be valid, the change in phase between the incident field and the wave propagating through the defect should be less than π [91, 121], which may be expressed mathematically by comparing the incident wave with the first order Born approximation of the scattered wave at the centre of the defect as

$$n_\delta ka < \pi, \tag{6.2}$$

where k is the wavenumber, a the characteristic dimension of the defect, and n_δ the deviation from the average refractive index, which describes the difference between the physical properties within the defect from those of the surrounding medium [121, 122]. In the following analyses with pipes with defects modelled in FE, this requirement is implemented as

$$\Delta\varphi = \varphi_{\text{inc}} - \varphi_{\text{trans}} < \pi, \text{ that is} \tag{6.3a}$$

$$\Delta\varphi/\pi < 1, \tag{6.3b}$$

where φ_{inc} is the phase of the interrogating signal monitored at a given distance from the excitation without any defects present, while φ_{trans} is the phase of the signal transmitted through a given defect at the same distance.

Gubernatis et al. commented that the Born approximation is especially applicable in a reflection mode, in comparison with forward scattering, and suggested a validity limit of $ka \leq 1$ for spherical voids and inclusions based on qualitative studies [63]. However, as noted by Simonetti [120], there is a question of how to define a weakly scattering medium. Several researchers have suggested different values for the validity of the Born approximation and estimated the error inferred by its application [63, 64, 120–124].

Thus, the validity of the Born approximation is governed by the contrast and size of the scattering object compared to the wavelength; the validity gradually increasing with lower contrast objects and longer wavelengths of the interrogating signal compared with the size of the scatterer. If the first order Born

approximation is valid, the solution of the integral equation can be replaced by performing a spatial Fourier transform, as noted by Schafbuch et al. [64], and adopted here.

In the following subsections, four different corrosion patch types are studied; an axisymmetric defect, a three-dimensional defect consisting of two cosine tapered ellipsoids, a real corrosion patch, and lastly cosine tapered pit clusters.

Axisymmetric defect

Axisymmetric defects may be modelled in 2D as a cross-section of the full defect geometry. However, as mentioned in Section 6.2, full 3D models are employed throughout this chapter for consistency. The solid line in figure 6.2 (a) shows a cross-section of the axisymmetric defect consisting of two cosine shaped defects with axial extents of 1/16 and 1/4 of the outer pipe diameter and with depths of 20 and 40% of the pipe wall thickness, respectively. A spatial resolution of 1/20 of the pipe wall thickness was employed. The dotted and dash-dotted lines show the cross-sections consisting of low- and high spatial frequency components, respectively, obtained using an FFT of length 2^{13}. Figure 6.2 (b) shows the wavenumber domain representation of the original profile. A cosine-tapered [125] low- and high pass filter with a rising/decaying edge of 10 samples and a transition around $k = 0.2$ (1/mm) is applied to obtain the filtered profiles shown in (a), as indicated by the dashed lines in (b). Note that the profile containing the high spatial frequency components displays negative depth values in the space domain, which is inevitable due to the properties of the FFT algorithm. These negative depth values were accounted for in the FE analyses by increasing the thickness of the wall at these locations accordingly.

The RC for the T(0,1) mode for the full solution (original profile, solid line), is compared with the RC obtained by superposition (dashed line) of the low and high spatial component profiles in figure 6.3, where the RCs from the low (dotted line) and high (dash-dotted line) profiles individually are also shown. The effect of removing of the low- and high spatial frequency components of the profile is clearly reflected in the resulting RC from the filtered profiles, as the profile with low spatial frequency content (dotted line) contributes little above, say, 60 kHz, while the profile with high spatial frequency content contributes increasingly with increasing frequency relative to the RC from the original profile.

An increasing deviation between the superposition and full solution results is seen towards higher frequencies. The deviation is due to the violation of the validity limits of the Born approximation, as the dimensions of the defect become larger compared with the wavelengths of the interrogating guided wave signal with increased frequency, and the phase shift of the transmitted wave relative to the incident wave is larger than π over the entire frequency range evaluated, as can be seen from figure 6.4, where the phase shift normalised by

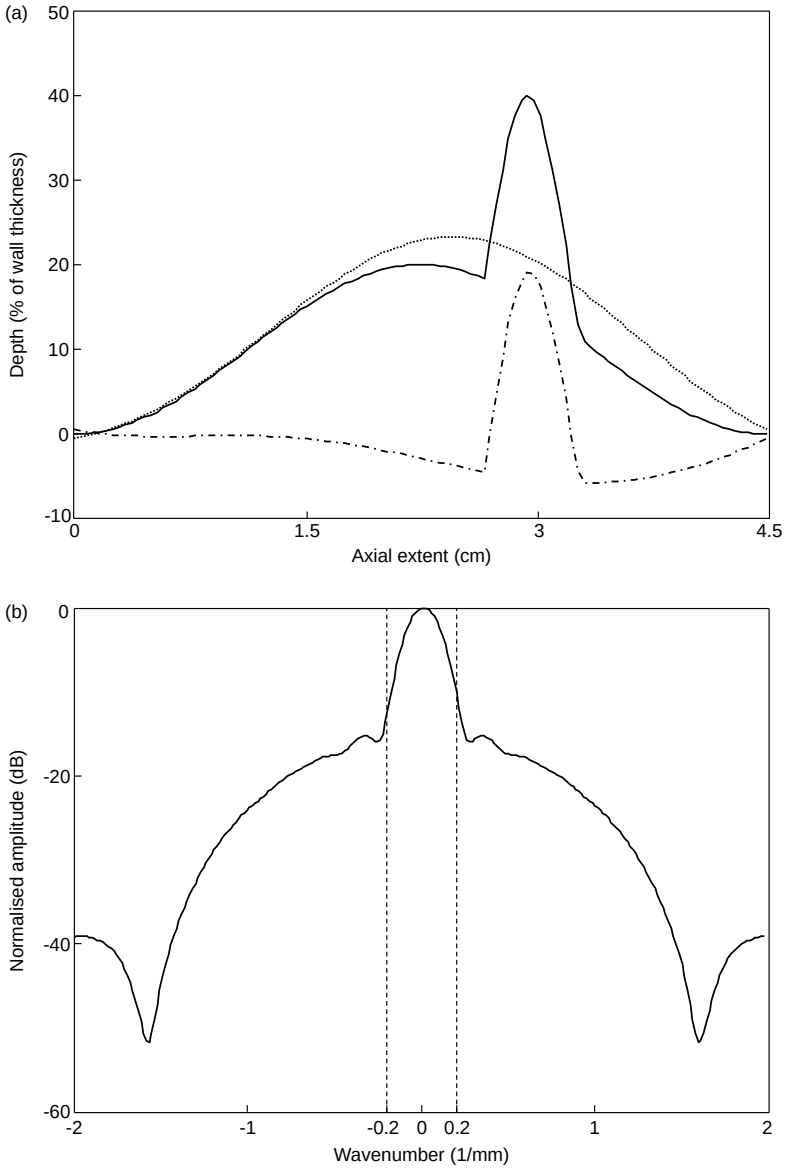

Figure 6.2: (a) Cross-section of axisymmetric defect (solid line). Profiles obtained after filtering in the wavenumber domain shown in dotted (low spatial frequencies) and dash-dotted lines (high spatial frequencies). (b) Wavenumber spectrum of axisymmetric defect. Cosine-tapered low- and high pass filters were applied at $k = 0.2$ (1/mm) to obtain the profiles consisting of low- and high spatial frequencies shown in (a), respectively.

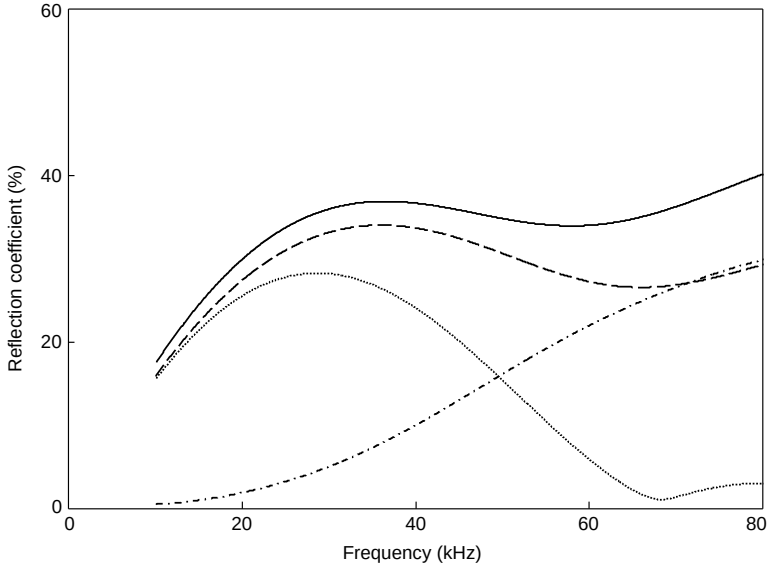

Figure 6.3: Reflection coefficients as a function of frequency for the original profile (solid line), low (dotted line) and high (dash-dotted line) spatial component profiles shown in figure 6.2 (a). The RC obtained from superposition of the low and high spatial component FE calculations is indicated by the dashed line.

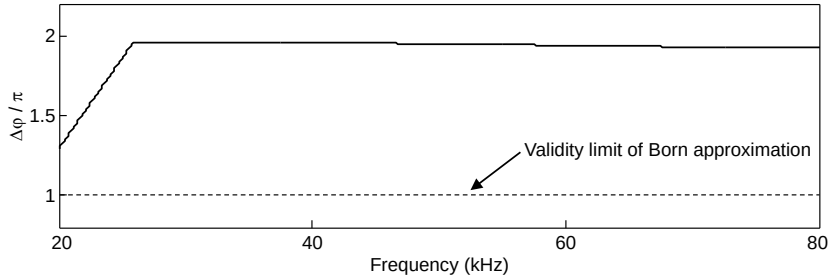

Figure 6.4: Phase shift normalised by π of the reflection from the axisymmetric defect shown in solid line in 6.2, where the validity limit of the Born approximation ($\Delta\varphi/\pi < 1$) is indicated by the dashed line.

π is shown as a function of frequency. The dashed line indicates the validity limit of the Born approximation.

That the Born approximation has limited validity in this case is in agreement with the general comments on the validity of the Born approximation made initially in this section. An axisymmetric defect is a worst case since ka in the circumferential direction is as large as it can be, and violates qualitative requirements suggested [15, 63, 71]. Additionally, the RC from the defect is large, approximately 40% from 30-80 kHz, meaning the defect can hardly be considered a low contrast scatterer.

Three-dimensional ellipsoidal defects

Following the analysis procedure used with the axisymmetric defect above, a three-dimensional defect patch consisting of two cosine tapered ellipsoidal shaped defects is considered. Figure 6.5 shows the layout unwrapped onto a plate for clarity. Related to the circumferential extent of the pipe, the extents of each of the two defects are 1/8 in the circumferential direction, and 1/4 of and 1/8 in the axial direction, with depths of 40 and 80% of the pipe wall thickness, respectively. A spatial resolution of 1/5 of the pipe wall thickness was used.

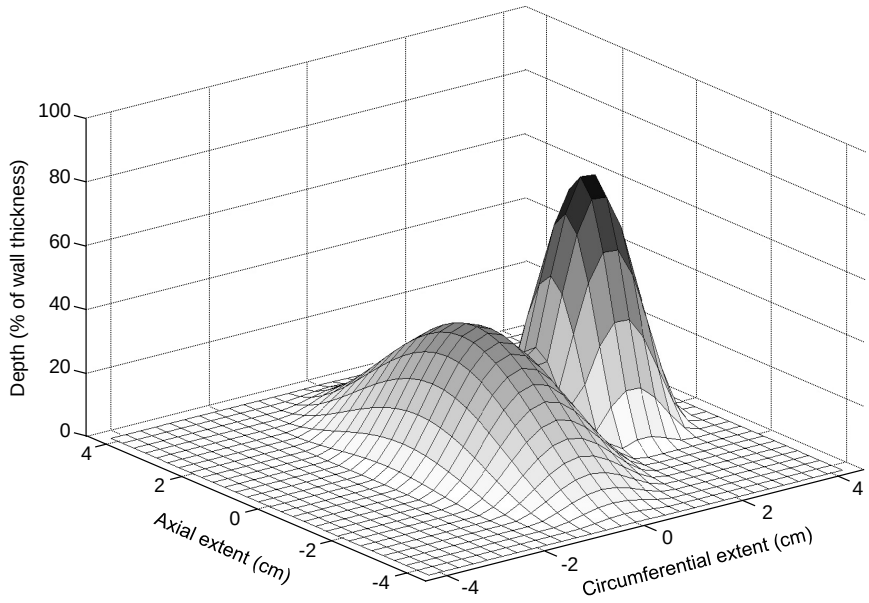

Figure 6.5: Defect layout consisting of two cosine tapered ellipsoidal defects of maximum depth 40 and 80% of the wall thickness, respectively. The layout is straightened out onto a plate for clarity.

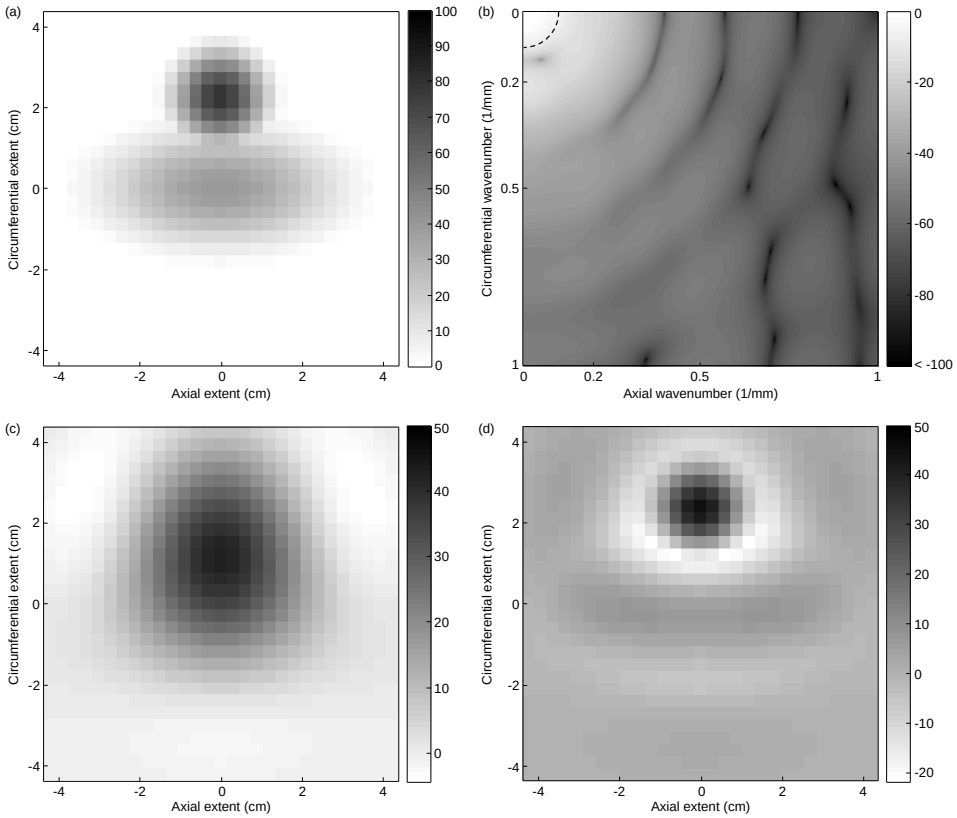

Figure 6.6: (a) Topside view of the defect layout shown in figure 6.5. (b) 2D FFT of the defect in (a) into the wavenumber domain, where the dashed line indicates the cross-over of the filter. (c) and (d) show layouts consisting of the low and high spatial frequency components of layout (a), respectively. All layouts are straightened out onto a plate. The scale bar in (a), (c) and (d) indicates depth as percentage of total wall thickness (note the different scales employed), and normalised dB-scale in (b).

Figure 6.6 (a) shows the defect in figure 6.5 from a topside view, as all subsequent defect layouts will be shown. All the layouts in the figure are straightened out onto a plate, with depth indicated as a percentage of the total pipe wall thickness on the scale bars. Note the different scales on the figures. Figure 6.6 (b) shows the positive quadrant of the wavenumber space representation of (a) obtained by employing a spatial 2D FFT (length 2^{12}), where the scale bar is on a normalised dB-scale. In this case a cosine tapered filter [125] was employed to filter the wavenumbers into low and high components at the wavelength corresponding to 50 kHz (tapered cross-over of 10 samples), which correspond

to roughly $k = 0.1$ (1/mm), as indicated by the dashed line in figure 6.6 (b). After filtering and performing an inverse FFT (length 2^{12}), (c) and (d) show the resulting layouts containing the low and high spatial components, respectively. As in the axisymmetric case, negative depths are obtained as a result of the FFT calculation and filtering. The low spatial frequency components show the main shape of the total layout, where details and separation of the two ellipsoids are lost; these details can be seen in the layout containing the high spatial frequencies in (d).

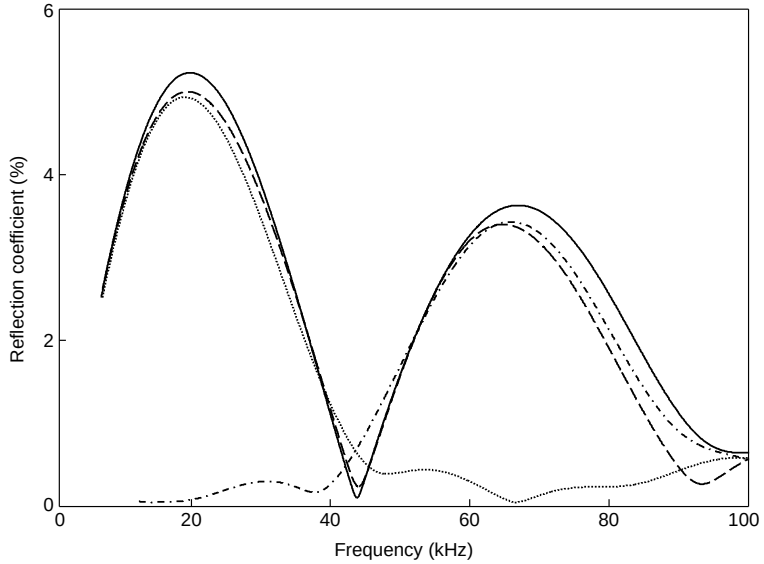

Figure 6.7: Reflection coefficient as a function of frequency for the defect layouts shown in figure 6.6. The solid line shows the RC for the original layout (figure 6.6 (a)), while the filtered layouts consisting of low and high spatial frequency components are shown in dotted and dash-dotted lines, respectively. The superposition of the low and high spatial frequency components is indicated by the dashed line.

Figure 6.7 shows the RCs calculated using FE for the full solution (solid line), superposition of low and high spatial frequency components (dashed line), and the low (dotted line) and high (dash-dotted line) frequency component layouts individually. The RC from the layout containing low spatial components has significant amplitude for frequencies below 50 kHz only, being comparable to that of the original layout in this frequency range. Similarly, the layout containing the high spatial frequencies gives a significant RC for frequencies above 50 kHz, which suggest that sharp changes in a defect profile result in RC at higher frequencies, and only affect the low frequency RC to a limited extent.

Relatively good agreement between the RC from the original profile and the superposition calculation is seen. Using the largest extent of the profile, roughly 9 cm, the ka values within the 20–80 kHz are from around 3 to 14, and so are significantly larger than the typical limit values suggested by e.g. Gubernatis et al. [63]. However, as the cosine tapered ellipsoidal profile is a rather weak scatterer with a smooth onset, the validity of the Born approximation is increased due to the low contrast of the defect. Indeed other researchers have employed an equivalent length expressed as the geometric average axial extent to describe the characteristic dimension of tapered defects, where it was also found that the RC at higher frequencies was lower with cosine tapered defects compared with linear tapers [17], as the cosine taper geometry is less sharp. This is in accordance with the relatively low RC seen in figure 6.7 in this case.

Real corrosion patch

A real corrosion patch obtained from a scanned area in an operational oil pipeline is considered in this section. Figure 6.8 shows the corrosion patch, which exhibits a sharp change in corrosion depth within a relatively limited area in an otherwise relatively modestly corroded section of the pipe.

The patch, with a spatial resolution 1/5 of the pipe wall thickness, is filtered into low and high spatial components using a 2D FFT (length 2^{12}) and the same cosine tapered filter as in the subsections above, with a spatial cross-over frequency corresponding to 70 kHz. The original layout is shown in (a), its wavenumber space representation in (b), and the layout corresponding to the low and high spatial frequency components in (c) and (d). Note the different scales on the figures. As seen for the patch consisting of the two ellipsoids in figure 6.6, the layout consisting of the high spatial frequencies (d) contains the details of the corrosion patch, while the main shape is governed by the low spatial frequencies (c).

Figure 6.9 shows the resulting RCs, where the RCs from the low and high spatial frequencies can be seen to only have significant amplitude within the frequency ranges corresponding to the wavenumbers of the filter employed. Thus, the small and deep pit will not influence the test results much if the testing range is limited to frequencies below 70 kHz, which is likely in many practical testing situations.

Very good agreement is seen between superposition and full solution results. In this case the phase shift within the bandwidth of evaluation complies with the validity limit of the Born approximation of $\Delta\varphi/\pi < 1$, as seen from figure 6.10.

Cosine tapered pit clusters

The two-dimensional FFT approach was likewise applied to the two example pit clusters shown in figure 5.13, which were used to validate the superposition

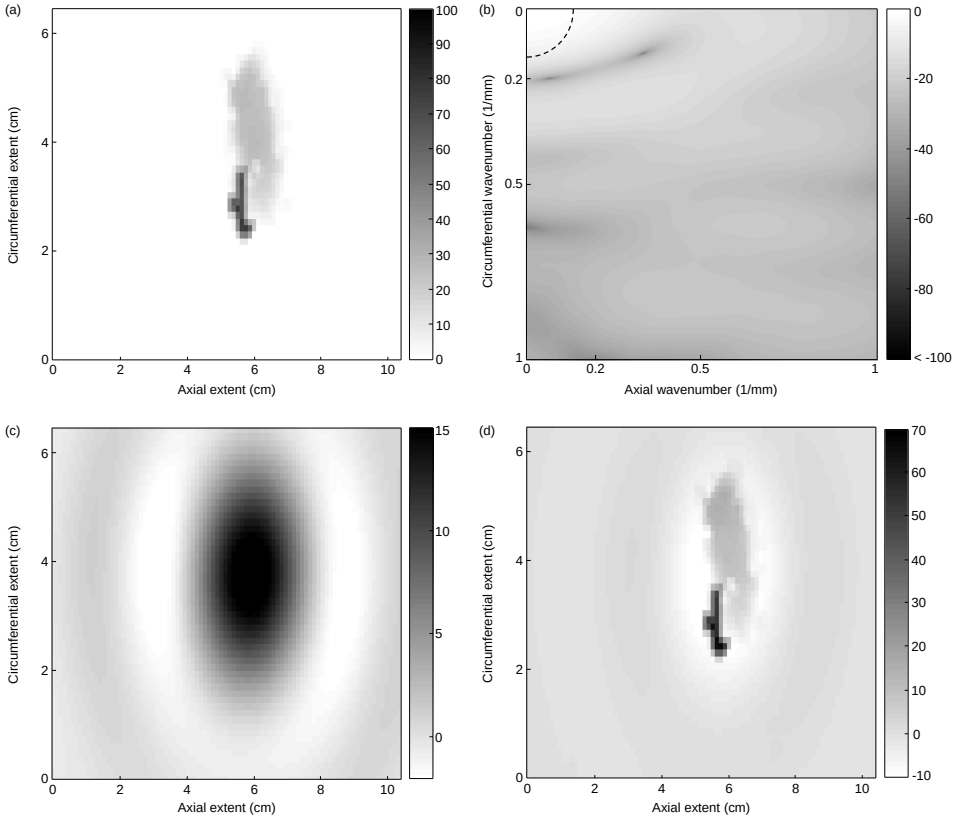

Figure 6.8: (a) Real corrosion patch, topside view. (b) 2D FFT of the defect in (a) into the wavenumber domain, where the dashed line indicates spatial cross-over of the filter. (c) and (d) show layouts consisting of the low and high spatial frequency components of layout (a), respectively. All layouts are straightened out onto a plate. Scale bars in (a), (c) and (d) indicate depth as percentage of total wall thickness (note the different scales employed), and normalised dB-scale in (b).

approach for tapered pit clusters in Section 5.3. This section only shows the effect of separating the wavenumber components on the filtered layouts, as a basis for further analyses in Section 6.4, and refrains from a discussion on their resulting RCs.

Figure 6.11 shows a cosine tapered defect of depth 40% of the pipe wall thickness, with a single pit of diameter $2t$ and depth 60% superposed onto it, where t is the pipe wall thickness; as the depth of the cosine taper at that specific location is 17.7%, the total depth of the pit is 77.7%. (c) and (d) show the cross-sections A–A and C–C, as indicated in (a). (b) shows the wavenumber

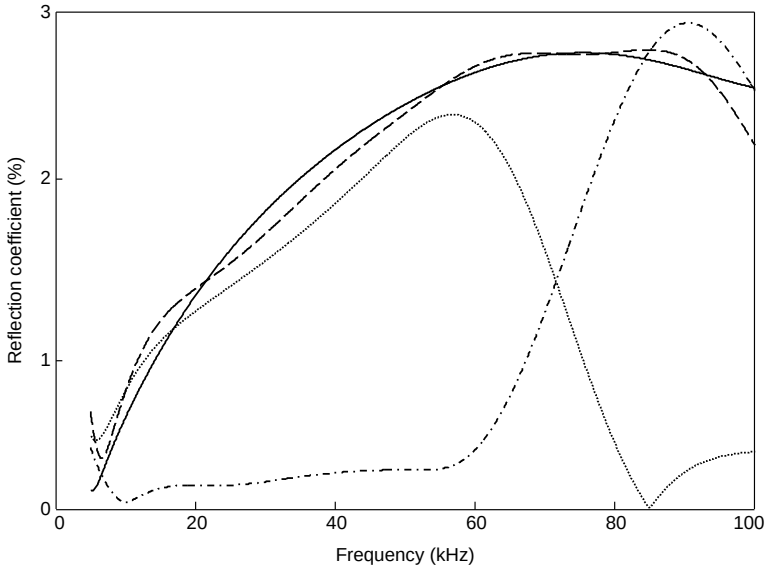

Figure 6.9: Reflection coefficient as a function of frequency for the defect layouts shown in figure 6.8. The RC for the original layout (figure 6.8 (a)) is shown in solid line, while the filtered layouts consisting of low and high spatial frequency components are shown in dotted and dash-dotted lines, respectively. The superposition of the low and high spatial frequency components is indicated by the dashed line.

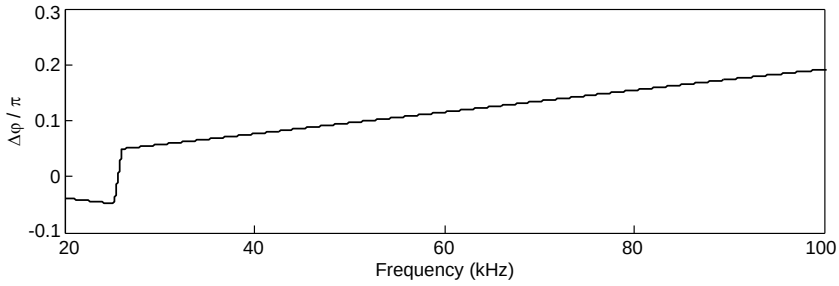

Figure 6.10: Phase shift normalised by π of the reflection from the axisymmetric defect shown in solid line in figure 6.8.

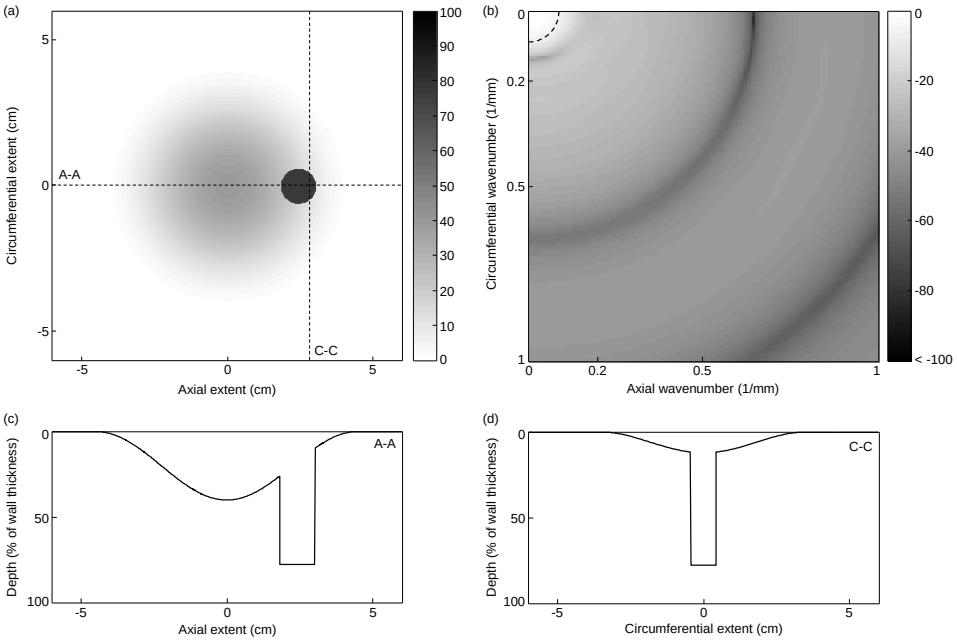

Figure 6.11: (a) Cosine taper with a pit cluster superposed onto it, straightened out onto a plate. (b) 2D FFT of the defect in (a) into the wavenumber domain, where the dashed line indicates spatial cross-over of the filter. The scale bar indicates depth as percentage of total wall thickness in (a), while normalised dB levels in (b). (c) and (d) show cross-sections A–A and C–C as indicated by the dashed lines in (a).

domain representation of the defect layout in (a), where a cosine tapered low and high pass filter with cross-over at the wavenumber corresponding to 40 kHz is applied to obtain defect layouts with the corresponding low and high wavenumber components, as shown in figure 6.12 (a) and (c), respectively. Figure 6.12 (b) and (d) show cross-sections (A–A and C–C) of the filtered layouts consisting of low and high wavenumber components, respectively, as indicated in the respective figures. Similarly as in the analysis with a cosine taper with the single defect in figures 6.11 and 6.12, calculations with a cosine taper with a pit cluster are shown in figures 6.13 and 6.14. A 2D FFT of length 2^{12} and a spatial resolution of 1/13 of the pipe wall thickness are used throughout in the calculations involving tapered pit clusters in this section.

From the pit clusters filtered into spatial frequency component ranges shown in figures 6.11 to 6.14, it is evident that sharp features in corrosion patches correspond to high spatial frequencies, while the extents of the main shape of the defect geometries are governed by the low spatial frequencies, as expected.

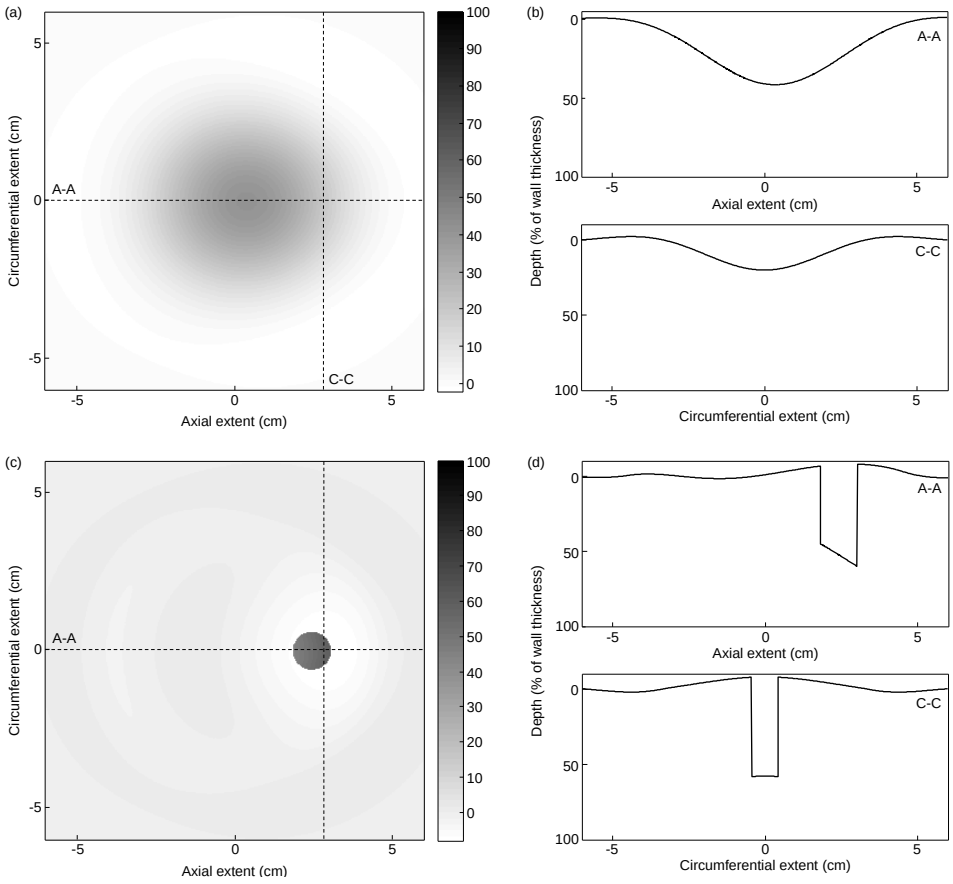

Figure 6.12: Defect profiles consisting of the low and high spatial frequency components of the layout shown in figure 6.11 (a) is shown in (a) and (c), respectively, where the respective cross-sectional profiles are indicated in (b) and (d). The layouts in (a) and (c) are straightened out onto a plate, while the scale bars indicate depth as percentage of total wall thickness (note the different scales employed).

To further investigate the influence of sharp edges within a defect patch an analysis of whether pit clusters can be represented as a single, complex defect by applying a smoothing algorithm to them is presented in the next section.

6.4 Representation of pit clusters as a single defect

The 2D FFT analyses in Section 6.3 suggest that sharp and sudden changes in depth within a corrosion patch result in increased RC at high frequencies.

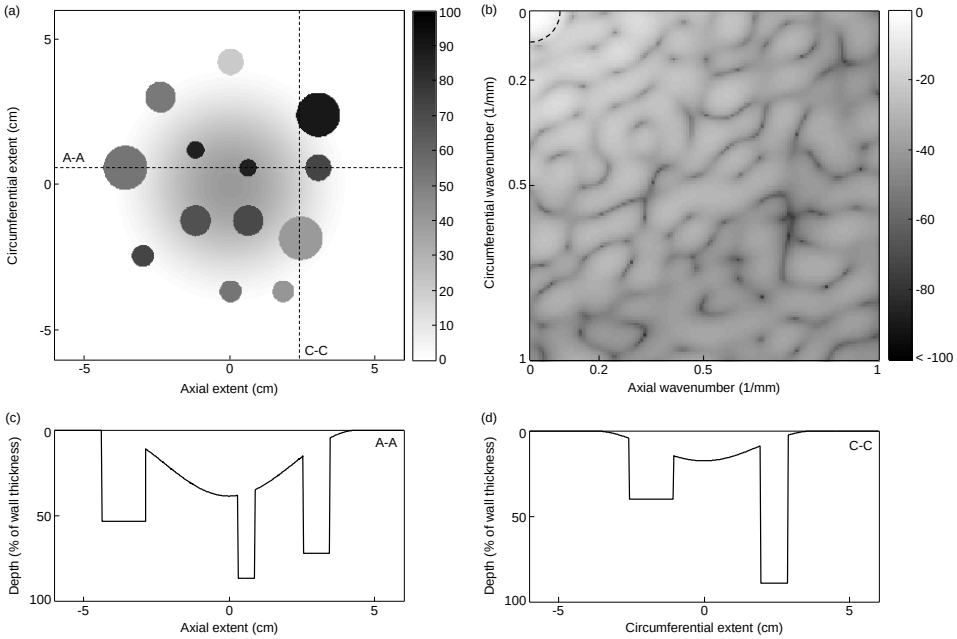

Figure 6.13: (a) Cosine taper with a pit cluster superposed onto it, straightened out onto a plate. (b) 2D FFT of the defect in (a) into the wavenumber domain, where the dashed line indicates spatial cross-over of the filter. The scale bar indicates depth as percentage of total wall thickness in (a), while normalised dB levels in (b). (c) and (d) show cross-sections A–A and C–C as indicated by the dashed lines in (a).

Specifically, the analyses with the tapered pit clusters indicated that removal of high spatial frequency components in corrosion patches with pit clusters superposed onto it removes pits of size smaller than certain diameter. This section follows the findings in Section 6.3, and assesses whether pit clusters can be represented as a single, complex defect. The idea is motivated by the difficulty experienced in resolving multiple pits and/or other features within complex corrosion profiles in practical inspection situations. If a cluster of pits can be well represented by a single, generalised corrosion defect, and results in comparable reflection coefficients, then known procedures to estimate the maximum depth of complex corrosion profiles [117] are directly applicable.

Figure 6.15 (a) and (b) show two example clusters to be used in evaluating the validity of representing a pit cluster as a single defect, which are two of the pit clusters used to evaluate the validity of applying superposition in the calculation of the RC from pit clusters in Section 5.2 (figures 5.5 (a) and 5.6 (a), respectively). The latter is used to explain the procedure used to vary the

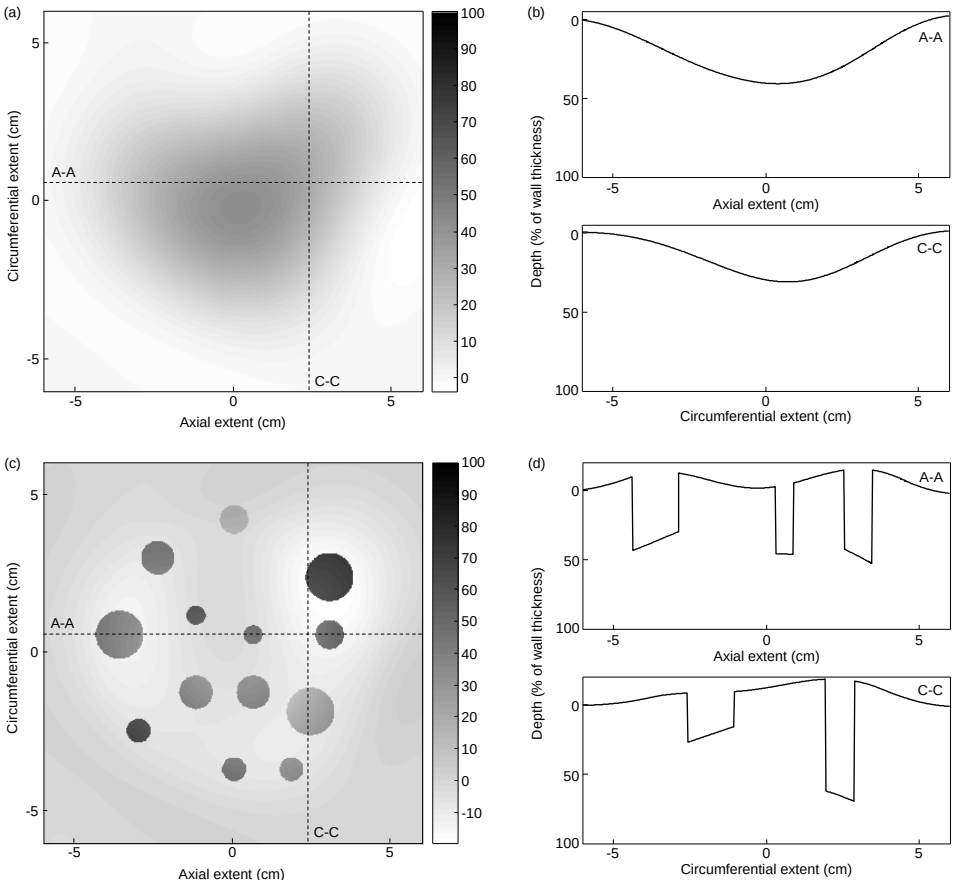

Figure 6.14: Profiles consisting of the low and high spatial frequency components of the layout shown in figure 6.13 (a) is shown in (a) and (c), respectively. (b) and (d) show cross-sections of the filtered profiles in (a) and (c), respectively. The layouts in (a) and (c) are straightened out onto a plate, while the scale bars indicate depth as percentage of total wall thickness (note the different scales employed).

size of the smoothing domain in (c) and (d), which is done as follows: a square is fitted to the extents of the layout, and the size of the circular domain is found as the distance from the centre of the square to the farthest point on the pits in the cluster (c). The size of the smoothing domain is then varied by increasing the radius of the circular domain in steps of t, which is the wall thickness of the pipe (d). A least-squares smoothing algorithm was used to obtain the single defect representations of the pit clusters. Single defect representations of the cluster in (b) with $t = 0$ and 4 are shown in (e) and (f), respectively.

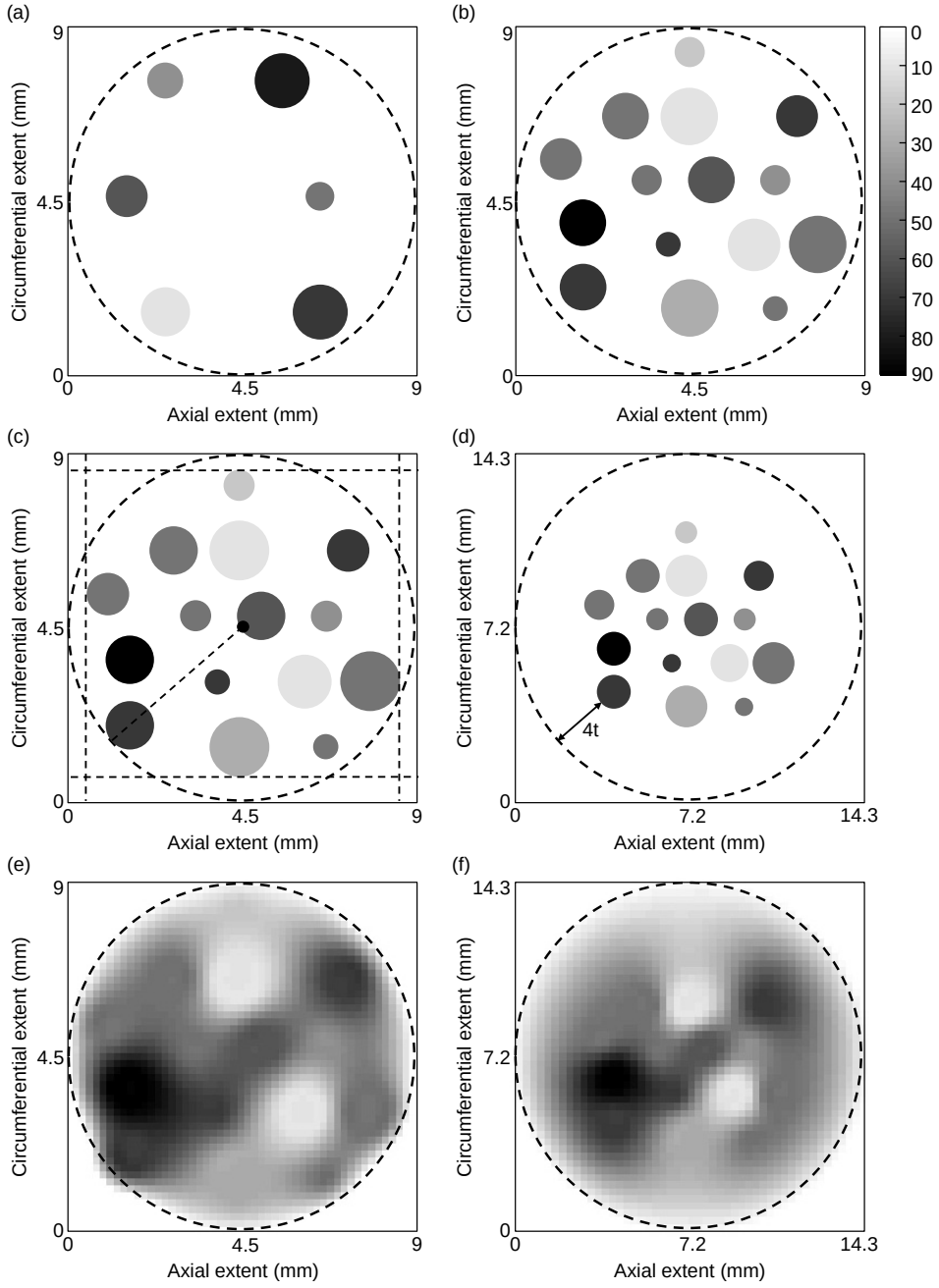

Figure 6.15: Example clusters (a) and (b), where the latter is used to illustrate a procedure to increase the smoothing area of the clusters in (c) and (d). (e) and (f) show the representation of the clusters in (c) and (d) as single defect, respectively. All layouts are straightened out onto a plate. The scale bar indicates depth as percentage of total wall thickness.

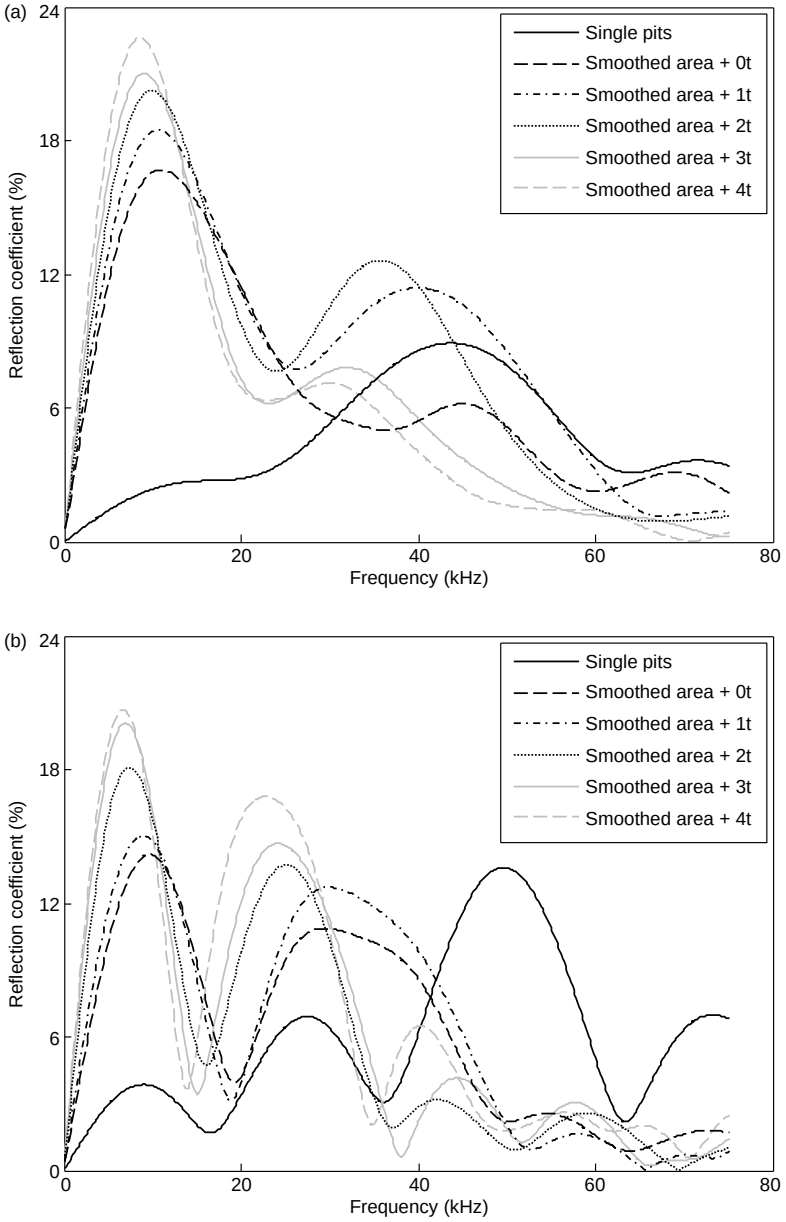

Figure 6.16: Reflection coefficient as a function of frequency for the pit clusters shown in (a) figure 6.15 (a) and (b) figure 6.15 (b), with increased smoothing area following the procedure described in figure 6.15 (c) and (d).

Figure 6.16 (a) and (b) compare the RCs from the pit clusters in figure 6.15 (a) and (b) with their representation as single defects calculated with increasing size of the smoothing area, as indicated in the figure legends. The calculated RCs exhibit similar results for both layouts, in that the first peak of the reflection coefficient occurs at a frequency where the total axial extent of the defect corresponds to $\lambda/4$ (in accordance with e.g. [11, 17]), and thus occurs at lower frequency with increasing axial extent; its amplitude increases due to the larger circumferential extent of the smoothing area (e.g. circumferential extent of figure 6.15 (d) compared with (c)). The significant volume added to the clusters by the smoothing algorithm results in increased RC at the first peak compared with the pit cluster.

For the pit clusters, interference between axially separated pits govern the RC at low frequency, while from around 40 kHz reflections from individual pits also increasingly affects the total RC (sizes from $1 - 2.5t$, which result in first peak from roughly 45-120 kHz). As the individual pits gets less defined when the smoothing algorithm is applied, the RC towards higher frequencies from the smoothed clusters is reduced compared with the pit clusters. This is seen throughout the simulations, and is especially evident in the more populated cluster in (b). Thus the presence of sharp edges in the corrosion profiles increases the RC at high frequencies. Consequently, in the absence of sharp changes in depth on corrosion profiles, low RC at high frequencies is to be expected. Therefore, representing pit clusters with sharp sided pits as single, complex defects is not a valid approximation. Even more populated and developed clusters and/or tapered pits are likely to give better results; however, this is not pursued further here.

6.5 Experimental validation

Experiments were conducted on three 3 m long 4 in. nominal bore schedule 40 steel pipes (outer diameter 114.3 mm, wall thickness 6.0 mm) to validate the FE predictions. Figure 6.17 shows the experimental setup.

The pipes were tested horizontally while resting on wooden supports which produced negligible reflections. Two transducer rings from Guided Ultrasonic Ltd. [10], with a total of 32 and 96 piezoelectric transducers, respectively, were used to cover the larger part of the frequency range employed in the FE simulations; covering a higher frequency range requires more transducers [114]. Each ring is divided into two rows of equally spaced transducers, in order to be able to distinguish the direction from which a reflection originates [115]. A total frequency range of 25–75 kHz was covered by the two rings, the excitation being a succession of 8 cycle Hanning windowed tonebursts of different centre frequencies generated by a Guided Ultrasonics Ltd. G3 Wavemaker [10] instrument. Each transducer ring was clamped on the external wall of the pipe to excite and receive the T(0,1) mode in both directions in the pipe as the piezoelectric transducers apply alternating forces in the circumferential direction.

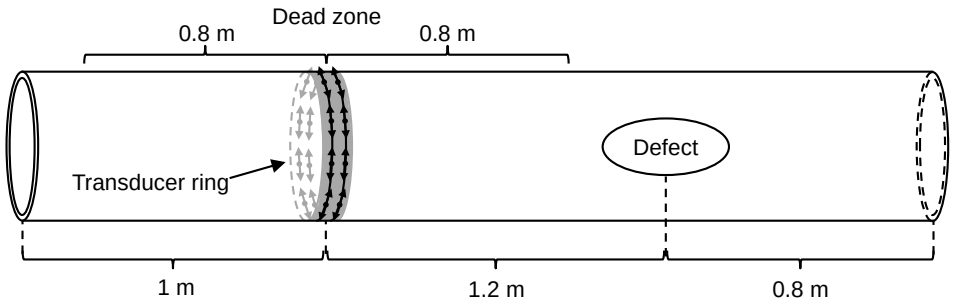

Figure 6.17: Schematic of experimental setup.

The reflection from the left hand end of the pipe acts as reference. Sufficient distance from the transducer ring to the defect and the left hand end of the pipe was applied to avoid the dead zone of the rings and ensure reliable results. Likewise, the defects were machined at 0.8 m distance from the right hand end of the pipe, so that their reflections could be separated from the stronger reflection from the right hand end of the pipe. RCs were calculated in the time domain as peak-to-peak amplitude ratios between the reflections from the defects and the reference end reflection. Up to 16 averages were employed in each measurement.

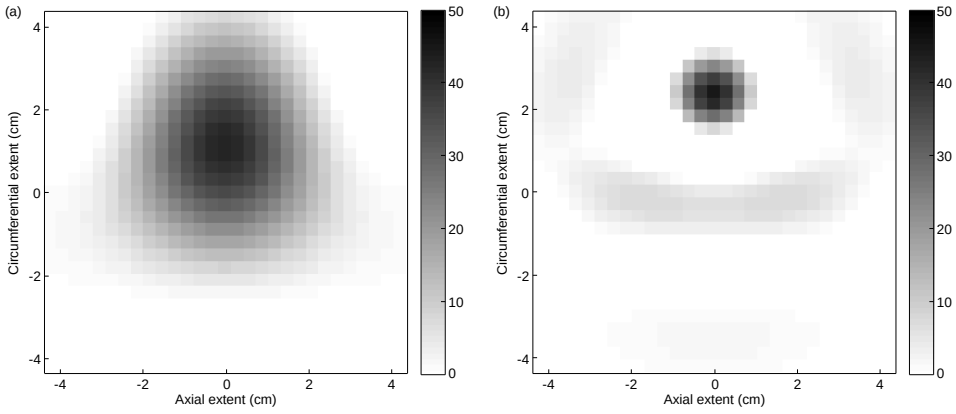

Figure 6.18: Topside view of the layouts consisting of the low (a) and high (b) spatial frequency components of the corrosion patch shown in figure 6.6 (a), with all negative depths due to the FFT and filtering algorithms set to zero. Both layouts are straightened out onto a plate, while the scale bars indicate depth as percentage of total wall thickness.

The experimental work is done on the three-dimensional ellipsoidal case discussed in Section 6.3, with all increases in wall thickness due to the FFT calculations neglected and set to zero depth, as the pipe wall thickness cannot be increased in the experiments. Figure 6.5 and 6.6 (a) show the defect layout to be evaluated, which consists of two cosine tapered ellipsoidal defects of depth 40 and 80%, as explained in detail in Section 6.3. Figure 6.18 (a) and (b) show the patches consisting of the low and high spatial frequency components, respectively, which correspond to the filtered patches of figure 6.6 (c) and (d), only with negative depths set to zero.

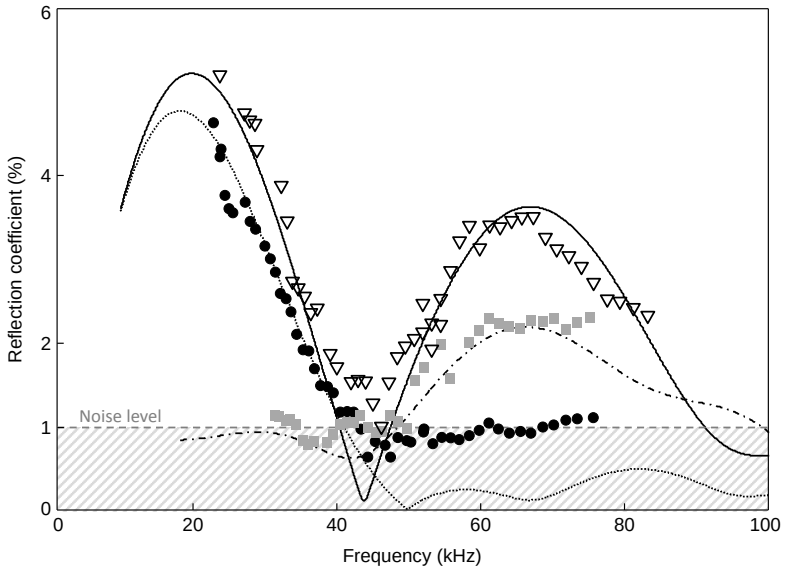

Figure 6.19: Comparison between FE (lines) and experiments (markers). Results for the original layout (figure 6.6 (a)), and the layouts consisting of its low (figure 6.18 (a)) and high (figure 6.18 (b)) spatial frequency components are indicated by solid line / ▽ , dotted line / • , and dash-dotted line / ■ , respectively. The noise level observed in the experiments is indicated by the hatched area.

Figure 6.19 shows comparisons between FE simulations and experimental results for all the three defect layouts. The solid line and open triangles (▽) show results for the original profile as shown in figure 6.6 (a), the layout consisting of its low spatial frequencies is indicated by dotted line and filled circles (•), and lastly the layout with its high spatial frequency content is indicated by dash-dotted line and grey squares (■). Excellent agreement can be seen throughout between the RC values obtained experimentally and through FE simulations.

A noise floor of approximately 1% was seen in the experiments, as indicated by the hatched area in figure 6.19, which thus is a lower bound for practically measureable RC values. Despite not being able to practically measure values below the noise floor, the experimentally obtained RCs within frequency regions where the simulated RC is below the noise floor are thus lower than the 1%, which validates the experiments to a certain extent also within these frequency regions.

The experiments confirm that the low spatial components mainly affect the RC at lower frequencies, which is comparable to the RC from the original defect patch at frequencies below 50 kHz in this case. Likewise, the layout containing the high spatial frequencies mainly result in a RC of certain amplitude for frequencies above 50 kHz, and agrees well with the FE results, which suggests that sharp changes in a defect profile result in RC at higher frequencies, and only to a limited extent affect the RC at lower frequencies.

6.6 Conclusions

A two-dimensional FFT approach is used to assess relationships between RC spectrums and the spatial frequencies of corrosion patches. Analyses of defects that are separated into patches consisting of low and high spatial frequency components have been investigated and compared with results obtained with the full defect profile.

Superposition of the two low and high frequency components was found to reconstruct the original defect profile with a small error. Furthermore, superposition of the reflections from the two filtered defects gave comparable reflection spectrums as with the full defect profile, limited by the validity of the superposition approach.

Low pass defects obtained by filtering the full profile in the spatial frequency domain with a low pass filter were found to give significant reflection only at low frequencies, while the high pass defect obtained by the same filtering procedure but with a high pass filter resulted in significant reflection only at high frequencies. These results indicate that sharp changes in depth result in significant reflections at high frequencies, and only to a minor extent affect RCs at lower frequencies. In contrast, corrosion patches with more gradual changes in depth result in a moderate contribution to the reflection coefficient at higher frequencies.

Representations of pit clusters with sharp sided pits as single, complex defects showed poor agreement between their calculated RCs, and is not a valid approximation. The single defect representation tended to overestimate the RC at low frequencies due to the increased volume of the defect, and also underestimate the RC at high frequencies due to the absence of sharp features in the corrosion patch. This agrees well with the findings from the FFT analyses; sharp changes in depth contribute significantly to the RC at high frequency, while the main shape of the defect governs the low frequency response in that

the total axial extent of the defect corresponds to $\lambda/4$ at the frequency where the first peak RC occurs. As a consequence of the poor agreement between the single defect approximation and the pit cluster, the maximum depth of corrosion profiles cannot be well estimated without better consideration and assessment of the high spatial frequency content of the corrosion profiles.

Chapter 7

Conclusions

In this chapter a review of the background and content of the thesis is given in Section 7.1, before the main findings are summarised in Section 7.2. Section 7.3 provides suggestions for future work and development.

7.1 Thesis review

The use of guided waves as a non-destructive testing (NDT) and evaluation technique has been investigated in this thesis. The work was motivated by a need to improve NDT techniques as petrochemical production moves towards harsher environments, with increasing presence of CO_2 and/or H_2S in production lines, which imply an increasing risk of shutdown due to localised corrosion. Localised corrosion is presently one of the main causes of degradation of subsea pipelines, and is insidious and difficult detect from a practical NDT point of view due to the large scatter in measurable parameters it exhibits, amongst which the maximum defect depth is the most important to assess and quantify accurately to achieve reliable and sustainable production conditions.

Initially, a discussion on the theoretical properties, basic principles of guided wave propagation, and finite element (FE) meshing and time stepping rules is provided in Chapter 2 as a basis for the analyses in subsequent chapters. In order to validate the FE models employed and understand the influence of modal properties on the reflection of the guided wave incident on a discontinuity, studies considering relatively simple shaped defects such as infinite notches and single through-thickness holes were done in Chapter 3, comparing the reflection and scattering from them with available results from the literature for validation. Excellent agreement was found throughout. The only slightly novel work in this chapter considered the reflection of the SH_0 and S_0 modes from a through-thickness hole with plane SH_0 wave incidence as a function of distance from the hole and hole size; albeit closely related to the work of Cegla et al. [32], who solved the same problem analytically and presented results as

a function of scattering angle at 0.5 m from the centre of the hole, with which the FE results presented here agreed well.

With chapters 1 to 3 as the basis, attention was turned to more complex defect in pipes from Chapter 4 onwards. In Chapter 4 a parametric study of the reflection of the fundamental torsional mode, T(0,1), from two and three small circular holes at different relative positions in a pipe was done, and the applicability limits of employing a superposition technique in doing so assessed as a function of defect separation, orientation and depth. As localised corrosion often occurs in clusters, the reflection from two and three circular holes is a step towards understanding the scattering behaviour of multiple and randomly spaced defects. A lower typical diameter to depth ratio of 1:1 for defects due to localised corrosion was established from the literature on corrosion morphology, which was employed throughout the chapter.

Following the results with two and three circular holes, the reflection of the fundamental torsional mode from a large number of randomly developed pit clusters was investigated in Chapter 5. The approach chosen was to calculate the maximum reflection coefficient (RC) from the clusters and investigate possible relationships to maximum defect depth. This was done both for clusters growing out of areas otherwise affected by general corrosion only, and for clusters being part of a larger attack. In doing so, problematic cases from a practical NDT point of view, where given pit clusters with deep maximum depth result in a low maximum RC, were assessed for test optimisation and evaluation.

As Chapter 5 indicated some problematic cases of pit clusters that would be difficult to detect in practical guided wave testing, Chapter 6 pursued the problematic features identified and investigated the influence of sharp edges in corrosion profiles on the resulting RCs. In doing so, a two-dimensional FFT approach was used to assess relationships between RC spectra and the spatial frequencies of corrosion patches. Following the analyses using the 2D FFT approach, an analysis of whether pit clusters can be represented as a single, complex defect was done. The validity of such an approach was evaluated by comparing the RC of the single defect representations with that of the corresponding pit clusters. If a cluster of pits can be well represented by a single, generalised corrosion defect, and results in comparable RCs, existing methodologies [117] to estimate the maximum depth may be employed.

7.2 Main findings

The main findings in this thesis can be summarised as follows:

- With circumferentially spaced holes, the RC for the T(0,1) mode was found to be independent of their circumferential position, provided the distances between them were larger than around $2a$ for through-thickness

defects, where a is the diameter of the holes. At shorter separation distances, multiple reflections between the defects influence the RC. A linear relationship between the RCs from circumferentially spaced defects and the total circumferential extent of the defects was found.

- With axially spaced circular holes, strong interference effects were seen in the RCs, governed by the defect separation distance, with the maximum RC being equal to that found for circumferentially separated defects for the T(0,1) mode. With two holes spaced at other orientations than purely circumferential or axial, the RC was again found to be independent of circumferential position.

- Superposition was found to be applicable down to a separation of around $2a$ for all defect orientations for through-thickness holes. With part-thickness defects superposition was valid down to shorter separation distances as multiple scattering became less significant in this case, which suggests that using superposition to simulate multiple part-depth defects and defects clusters will be satisfactory.

- With three axially separated defects, the frequency of the first peak RC is governed by the total axial extent of the defect layout. When the holes are separated equally and the distance between successive holes is a multiple of $\lambda/2$, constructive interference occurs and gives rise to maxima in the RC. This condition is not necessarily met at the first peak frequency so the RC may be higher at subsequent peaks, which suggests that the maximum RC is a better evaluation parameter.

- The maximum RC from pit clusters was found to be a linear function of the total volume fraction removed, but with very significant scatter due to interference between axially separated pits. Based on reports from the corrosion community on the typical area confinement of localised corrosion, a circular defect domain with diameter equal to a quarter of the pipe circumference was employed. With pit clusters developing in areas otherwise affected by general corrosion only, more than 99% of the pit clusters with maximum depth deeper than 70% of the pipe wall thickness resulted in a maximum RC of 2% or higher, and are therefore likely to be detected before they propagate fully through wall.

- Detailed analyses of typical problematic cases that gave small maximum RC values revealed that most of these clusters consisted of single, small and deep defects in otherwise relatively shallow and lightly populated clusters. Despite such cluster morphologies being improbable in practice, some cases do occur and are likely to be missed by guided wave testing; in a few cases, destructive interference between pits in clusters consisting of several larger pits that were axially spaced relative to each other resulted in small maximum RCs. Such cases are likely to be detected if the pipe

segment was monitored over time, as the cluster then would be assessed multiple times during its development, as noted in Section 7.3.

- The probability of detecting pit clusters with deep maximum depth increases if they are part of a larger attack rather than growing in regions otherwise unaffected by corrosion. For the cosine tapered pit clusters investigated, no cluster with maximum depth $\geq$60% of the pipe wall thickness resulted in a maximum RC below 4% with cosine taper depth of 30% or deeper.

- Analyses of defects that are separated into corrosion patches consisting of low and high spatial frequency components indicate that sharp changes in depth result in significant reflections at high frequencies, and only to a minor extent affect RCs at lower frequencies. In contrast, corrosion patches with more gradual changes in depth result in a moderate contribution to the RCs at higher frequencies.

- Representations of pit clusters with sharp sided pits as single, complex defects showed poor agreement between their calculated RCs, and is not a valid approximation. The single defect representation tended to overestimate the RC at low frequencies due to the increased volume of the defect, and also underestimate the RC at high frequencies due to the absence of sharp features in the corrosion patch.

7.3 Future work

Non-destructive guided wave testing and evaluation is a massive research field, with a wide range of problems and challenges that needs to be solved. As a direct extension to the work in this thesis, suggestions for further research and development include:

- Investigate the possibilities of increasing the bandwidth employed in practical guided wave testing, as is presently in progress in leading commercial guided wave companies, e.g. [10]. This would enable better assessment and resolution of smaller defects and defects with sharp changes in depth within a small geometrical area.

- Further investigate the influence of various defect shapes and of specific features in them on the (maximum) reflection coefficient. More extensive analyses of realistic corrosion profiles will further help to identify potential development steps needed.

- Investigate typical problematic corrosion attacks at several stages during their development, to assess whether they could be detected if monitored regularly over time.

- Develop improved links with corrosion groups to identify and explore guided wave possibilities, and to ensure that guided wave inspection research include realistic corrosion profiles in the present (and future) petrochemical production environments.

Bibliography

[1] M. B. Kermani and A. Morshed, "Carbon dioxide corrosion in oil and gas production - A compendium," *Corrosion*, vol. 59, no. 8, pp. 659–683, 2003.

[2] J. Kvarekvål, "Morphology of localised corrosion attacks in sour environments," in *Corrosion/2007*, paper 07659, (Nashville, Tn, US), NACE International, 11-15 March 2007.

[3] S. Papavinasam, W. Friesen, R. W. Revie, and A. Doiron, "Predicting internal pitting corrosion of oil and gas pipelines: A corrosion engineering approach," in *Corrosion/2005*, paper 05645, (Houston, Tx, US), NACE International, 3-7 April 2005.

[4] A. Valor, F. Caleyo, L. Alfonso, D. Rivas, and J. M. Hallen, "Stochastic modelling of pitting corrosion: A new model for initiation and growth of multiple corrosion pits," *Corrosion science*, vol. 49, pp. 559–579, 2007.

[5] SINTEF. `http://www.sintef.no/Projectweb/SmartPipe/` (date last viewed 2011-08-28).

[6] E. Bardal, *Corrosion and protection*. Springer Verlag, 2004.

[7] P. Cawley, M. J. S. Lowe, F. Simonetti, C. Chevalier, and A. G. Roosenbrand, "The variation of the reflection coefficient of extensional guided waves in pipes from defects as a function of defect depth, axial extent, circumferential extent and frequency," *J. Mech. Eng. Sci.*, vol. 216, pp. 1131–1143, 2002.

[8] J. L. Rose, *Ultrasonic waves in solid media*. Cambridge University Press, 1999.

[9] J. L. Rose, "A baseline and vision of ultrasonic guided wave inspection potential," *J. Pressure Vessel*, vol. 124, pp. 273–282, 2002.

[10] Guided Ultrasonics Ltd. `http://www.guided-ultrasonics.com` (date last viewed 2011-08-23).

[11] A. Demma, P. Cawley, M. Lowe, A. G. Roosenbrand, and B. Pavlakovic, "The reflection of guided waves from notches in pipes: a guide for interpreting corrosion measurements," *NDT&E Int.*, vol. 37, pp. 167–180, 2004.

[12] J. Davies and P. Cawley, "The application of synthetic focusing for imaging crack-like defects in pipelines using guided waves," *IEEE Trans. Ultrason. Ferroelectr. Freq. Control*, vol. 56, pp. 759–771, 2009.

[13] W. Luo and J. L. Rose, "Phased array focusing with guided waves in a viscoelastic coated hollow cylinder," *J. Acoust. Soc. Am.*, vol. 121, no. 4, pp. 1945–1955, 2007.

[14] J. J. Ditri, "Utilization of guided waves for the characterization of circumferential cracks in hollow cylinders," *J. Acoust. Soc. Am.*, vol. 96, no. 6, pp. 3769–3775, 1994.

[15] A. Demma, P. Cawley, M. J. S. Lowe, and A. G. Roosenbrand, "The reflection of the fundamental torsional mode from cracks and notches in pipes," *J. Acoust. Soc. Am.*, vol. 114, no. 2, pp. 611–625, 2003.

[16] H. Bai, A. H. Shah, N. Popplewell, and S. K. Datta, "Scattering of guided waves by circumferential cracks in steel pipes," *J. Appl. Mech.*, vol. 68, pp. 619–631, 2001.

[17] R. Carandente, J. Ma, and P. Cawley, "The scattering of the fundamental torsional mode from axi-symmetric defects with varying depth profile in pipes," *J. Acoust. Soc. Am.*, vol. 127, no. 4, pp. 3440–3448, 2010.

[18] W. Zhu, "An FEM simulation for guided wave generation and reflection in hollow cylinders with corrosion defects," *J. Pressure Vessel Technol.*, vol. 124, pp. 108–117, 2002.

[19] M. Castaings and C. Bacon, "Finite element modelling of torsional wave modes along pipes with absorbing materials," *J. Acoust. Soc. Am.*, vol. 119, no. 6, pp. 3741–3751, 2008.

[20] A. Galvagni and P. Cawley, "The reflection of guided waves from simple supports in pipes," *J. Acoust. Soc. Am.*, vol. 129, no. 4, pp. 1869–1880, 2011.

[21] X. Wang, P. W. Tse, C. K. Mechefske, and M. Hua, "Experimental investigation of reflection in guided wave-based inspection for the characterization of pipeline defects," *NDT&E Int.*, vol. 43, pp. 365–374, 2010.

[22] P. Rajagopal and M. J. S. Lowe, "Scattering of the fundamental shear horizontal guided wave by a part-thickness crack in an isotropic plate," *J. Acoust. Soc. Am.*, vol. 124, no. 5, pp. 2895–2904, 2008.

[23] M. Ratassepp, S. Fletcher, and M. J. S. Lowe, "Scattering of the fundamental torsional mode at an axial crack in a pipe," *J. Acoust. Soc. Am.*, vol. 127, no. 2, pp. 730–740, 2010.

[24] T. Grahn, "Lamb wave scattering from a circular partly through-thickness hole in a plate," *Wave Motion*, vol. 37, pp. 63–80, 2003.

[25] A. Løvstad and P. Cawley, "The reflection from the fundamental torsional mode from multiple circular holes in pipes," *NDT&E Int.*, vol. 44, pp. 553–562, 2011.

[26] J. Ma and P. Cawley, "Low-frequency pulse echo reflection of the fundamental shear horizontal mode from part-thickness elliptical defects in plates," *J. Acoust. Soc. Am.*, vol. 127, no. 6, pp. 3485–3493, 2010.

[27] A. Velichko and P. Wilcox, "Excitation and scattering of guided waves: Relationships between solution for plates and pipes," *J. Acoust. Soc. Am.*, vol. 125, no. 5, pp. 3623–3631, 2009.

[28] M. J. S. Lowe and O. Diligent, "Low-frequency reflection characteristics of the s_0 Lamb wave from a rectangular notch in a plate," *J. Acoust. Soc. Am.*, vol. 111, no. 1, pp. 64–74, 2001.

[29] M. J. S. Lowe, P. Cawley, J.-Y. Kao, and O. Diligent, "The low frequency reflection characteristics of the fundamental antisymmetric Lamb wave a_0 from a rectangular notch in a plate," *J. Acoust. Soc. Am.*, vol. 112, no. 6, pp. 2612–2622, 2002.

[30] A. Demma, P. Cawley, and M. Lowe, "Scattering of the fundamental shear horizontal mode from steps and notches in plates," *J. Acoust. Soc. Am.*, vol. 113, no. 4, pp. 1880–1891, 2003.

[31] O. Diligent, T. Grahn, A. Boström, P. Cawley, and M. J. S. Lowe, "The low-frequency reflection and scattering of the s_0 Lamb mode from a circular through-thickness hole in a plate: Finite element, analytical and experimental studies," *J. Acoust. Soc. Am.*, vol. 112, no. 6, pp. 2589–2601, 2002.

[32] F. B. Cegla, A. Rohde, and M. Veidt, "Analytical prediction and experimental measurement for mode conversion and scattering of plate waves at non-symmetric circular blind holes in isotropic plates," *Wave Motion*, vol. 45, pp. 162–177, 2008.

[33] A. Løvstad and P. Cawley, "The reflection of the fundamental torsional mode from pit clusters in pipes," *NDT&E Int.*, vol. 46, pp. 83–93, 2012.

[34] R. Carandente, A. Løvstad, and P. Cawley, "The influence of sharp edges in corrosion profiles on the reflection of guided waves," *submitted to NDT&E Int.*, 2012.

[35] B. A. Auld, *Acoustic fields and waves in solids*, vol. 2. Krieger Publishing Company Malabar, 1990.

[36] K. F. Graff, *Wave motion in elastic solids*. Dover Publications inc., 1973.

[37] M. J. S. Lowe, "Matrix techniques for modelling ultrasonic waves in layered media," *IEEE Trans. Ultrason. Ferroelectr. Freq. Control*, vol. 2, no. 4, pp. 525–542, 1995.

[38] M. C. Pochhammer, "Ueber die Fortpflanzungsgeschwindigkeiten kleiner Schwingugen in einem unbegrenzten isotropen Kreisecylinder," *J. für die reine und angewandte mathematik*, vol. 81, pp. 324–336, 1876.

[39] C. Chree, "The equations of an isotropic elastic solid in polar and cylindrical coordinates, their solution and applications," *Trans. Cambridge. Philos. Soc.*, vol. 14, pp. 250–369, 1889.

[40] D. C. Gazis, "Three-dimensional investigation of the propagation of waves in hollow circular cylinders. I. Analytical foundation," *J. Acoust. Soc. Am.*, vol. 31, no. 5, pp. 568–573, 1959.

[41] D. C. Gazis, "Three-dimensional investigation of the propagation of waves in hollow circular cylinders. II. Numerical results," *J. Acoust. Soc. Am.*, vol. 31, no. 5, pp. 573–578, 1959.

[42] A. H. Fitch, "Observation of elastic-pulse propagation in axially symmetric and nonaxially symmetric longitudinal modes of hollow cylinders," *J. Acoust. Soc. Am.*, vol. 35, no. 5, pp. 706–708, 1963.

[43] B. N. Pavlakovic, *Leaky guided ultrasonic waves in NDT*. PhD thesis, Imperial College, London, 1998.

[44] B. N. Pavlakovic, M. J. S. Lowe, D. N. Alleyne, and P. Cawley, "DISPERSE: A general purpose program for creating dispersion curves," in *Review of progress in quantitative NDE* (D. Thompson and D. Chimenti, eds.), vol. 16, pp. 185–192, San Diego, Ca, US: Plenum Press, 3-8 August 1997.

[45] B. N. Pavlakovic and M. J. S. Lowe, "A general purpose approach to calculating the longitudinal and flexural modes of multi-layered, embedded, transversely isotropic cylinders," in *Review of progress in quantitative NDE* (D. Thompson and D. Chimenti, eds.), vol. 18, pp. 239–246, Montreal, Canada: Plenum Press, 25-30 July 1999.

[46] L. Knopoff, "A matrix method for elastic wave problems," *Bull. Seism. Soc. Am.*, vol. 54, pp. 431–438, 1964.

[47] H. Schmidt and F. B. Jensen, "Efficient numerical solution technique for wave propagation in horizontally stratified environments," *Comput. Math. Appl.*, vol. 11, pp. 699–715, 1985.

[48] M. G. Silk and K. F. Bainton, "The propagation in metal tubing of ultrasonic wave modes equivalent to Lamb waves," *Ultrasonics*, vol. 17, pp. 11–19, 1979.

[49] M. J. S. Lowe, D. Alleyne, and P. Cawley, "The mode conversion of a guided wave by a part-circumferential notch in a pipe," *J. Appl. Mech.*, vol. 65, pp. 649–656, 1998.

[50] P. Wilcox, M. Lowe, and P. Cawley, "The effect of dispersion on long-range inspection using ultrasonic guided waves," *NDT&E Int.*, vol. 34, pp. 1–9, 2001.

[51] T. Hayashi and M. Murase, "Defect imaging with guided waves in a pipe," *J. Acoust. Soc. Am.*, vol. 117, no. 4, pp. 2134–2140, 2005.

[52] M. J. S. Lowe, D. N. Alleyne, and P. Cawley, "Defect detection in pipes using guided waves," *Ultrasonics*, vol. 36, pp. 147–154, 1998.

[53] D. Alleyne, M. Lowe, and P. Cawley, "The reflection of guided waves from circumferential notches in pipes," *J. Appl. Mech.*, vol. 65, pp. 635–641, 1998.

[54] R. Sicard, J. Goyette, and D. Zellouf, "A numerical dispersion compensation technique for time compression of Lamb wave signals," *Ultrasonics*, vol. 40, pp. 727–732, 2002.

[55] P. D. Wilcox, M. J. S. Lowe, and P. Cawley, "A signal processing technique to remove the effect of dispersion from guided wave signals," in *Review of progress in quantitative NDE* (D. Thompson and D. Chimenti, eds.), vol. 20, pp. 555–562, Brunswick, Me, US: Plenum Press, 29 July - 3 August 2001.

[56] H. Lamb, "On waves in an elastic plate," in *Proc. R. Soc. Lond. A*, 93, pp. 114–128, 1917.

[57] J. D. Achenbach and Y. Xu, "Wave motion in an isotropic elastic layer generated by a time harmonic point load of arbitrary direction," *J. Acoust. Soc. Am.*, vol. 106, no. 1, pp. 83–90, 1999.

[58] J. D. Achenbach, "Lamb waves as thickness vibration superimposed on a membrane carrier wave," *J. Acoust. Soc. Am.*, vol. 103, no. 5, pp. 2283–2286, 1998.

[59] H. Nishino, S. Takashina, F. Uchida, M. Takemoto, and K. Ono, "Modal analysis of hollow cylindrical guided waves and applications," *Jpn. J. Appl. Phys.*, vol. 40, pp. 364–370, 2001.

[60] J. Li and J. L. Rose, "Natural beam focusing of non-axisymmetric guided waves in large-diameter pipes," *Ultrasonics*, vol. 44, pp. 35–45, 2006.

[61] G. Kino, *Acoustic waves: Devices, imaging and analogue signal processing*. Prentice-Hall, 1987.

[62] J. E. Gubernatis, E. Domany, and J. A. Krumhansl, "Formal aspects of the theory of the scattering of ultrasound by flaws in elastic materials," *J. Appl. Phys.*, vol. 48, no. 7, pp. 2804–2811, 1977.

[63] J. E. Gubernatis, E. Domany, J. A. Krumhansl, and M. Huberman, "The Born approximation in the theory of the scattering of elastic waves by flaws," *J. Appl. Phys.*, vol. 48, no. 7, pp. 2812–2819, 1977.

[64] P. J. Schafbuch, R. B. Thompson, and F. J. Rizzo, "Elastic scatterer interaction via generalized Born series and far-field approximations," *J. Acoust. Soc. Am.*, vol. 93, no. 1, pp. 295–307, 1993.

[65] J. H. Rose and J. M. Richardson, "Time domain Born approximation," *J. Nondestr. Eval.*, vol. 3, no. 1, pp. 45–53, 1982.

[66] J.-M. Baik and R. B. Thompson, "Ultrasonic scattering from imperfect interfaces: A quasi-static model," *J. Nondestr. Eval.*, vol. 4, no. (3/4), pp. 177–196, 1984.

[67] F. J. Margetan, R. B. Thompson, and T. A. Gray, "Interfacial spring model for ultrasonic interactions with imperfect interfaces: Theory of oblique incidence and application to diffusion-bonded butt joints," *J. Nondestr. Eval.*, vol. 7, no. (3/4), pp. 131–152, 1988.

[68] A. Sedov and L. W. Schmerr Jr., "The time domain elastodynamic Kirchhoff approximation for cracks: The inverse problem," *Wave Motion*, vol. 8, pp. 15–26, 1986.

[69] A. Sedov and L. W. Schmerr Jr., "Pulse distortion and the elastodynamic Kirchhoff approximation for cracks. the direct and inverse problems," *SIAM J. Appl. Math.*, vol. 47, no. 6, pp. 1201–1215, 1987.

[70] J. D. Achenbach, A. K. Gautesen, and H. McMaken, *Ray methods for waves in elastic solids*. Pitman books Ltd., 1982.

[71] P. Rajagopal, *Towards higher resolution guided wave inspection: Scattering studies*. PhD thesis, Imperial College, London, 2008.

[72] L. W. Schmerr Jr., S.-J. Song, and A. Sedov, "Ultrasonic flaw sizing inverse problems," *Inverse Problems*, vol. 18, pp. 1775–1793, 2002.

[73] "Abaqus version 6.7 user's manual." `www.simulia.com` (date last viewed 2012-02-25).

[74] "Abaqus version 6.9 user's manual." `www.simulia.com` (date last viewed 2012-02-25).

[75] "Comsol user's guide version 3.5a." `www.comsol.com` (date last viewed 2012-02-25).

[76] M. B. Drozdz, *Efficient finite element modelling of ultrasound waves in elastic media*. PhD thesis, Imperial College, London, 2007.

[77] F. Moser, L. J. Jacobs, and J. Qu, "Modeling elastic wave propagation in waveguides with the finite element method," *NDT&E Int.*, vol. 32, pp. 225–234, 1999.

[78] D. Alleyne and P. Cawley, "A two-dimensional Fourier transform method for the measurement of propagating multimode signals," *J. Acoust. Soc. Am.*, vol. 89, no. 3, pp. 1159–1168, 1991.

[79] D. N. Alleyne and P. Cawley, "The interaction of Lamb waves with defects," *IEEE Trans. Ultrason. Ferroelectr. Freq. Control*, vol. 39, pp. 381–397, 1992.

[80] Y. Cho and J. L. Rose, "A boundary element solution for a mode conversion study on the edge reflection of Lamb waves," *J. Acoust. Soc. Am.*, vol. 99, no. 4, pp. 2097–2109, 1996.

[81] Y. Cho, D. D. Hongerholt, and J. L. Rose, "Lamb wave scattering analysis for reflection characterization," *IEEE Trans. Ultrason. Ferroelectr. Freq. Control*, vol. 44, pp. 44–52, 1997.

[82] T. Hayashi and K. Kawashima, "Multiple reflections of Lamb waves at a delamination," *Ultrasonics*, vol. 40, pp. 193–197, 2002.

[83] E. L. Clézio, M. Castaings, and B. Hosten, "The interaction of the S_0 Lamb mode with vertical cracks in an aluminium plate," *Ultrasonics*, vol. 40, pp. 193–197, 2002.

[84] O. Diligent and M. J. S. Lowe, "Reflection of the s_0 Lamb mode from a flat bottom circular hole," *J. Acoust. Soc. Am.*, vol. 118, no. 5, pp. 2869–2879, 2005.

[85] P. Rajagopal and M. J. S. Lowe, "Short range scattering of the fundamental shear horizontal guided wave mode normally incident at a through-thickness crack in an isotropic plate," *J. Acoust. Soc. Am.*, vol. 122, no. 3, pp. 1527–1538, 2007.

[86] P. Rajagopal and M. J. S. Lowe, "Angular influence on the scattering of fundamental shear horizontal guided waves by a through-thickness crack in an isotropic plate," *J. Acoust. Soc. Am.*, vol. 124, no. 4, pp. 2021–2030, 2008.

[87] M. Ratassepp, M. J. S. Lowe, P. Cawley, and A. Klauson, "Scattering of the fundamental shear horizontal mode in a plate when incident at a through crack aligned in the propagation direction of the mode," *J. Acoust. Soc. Am.*, vol. 124, no. 5, pp. 2873–2882, 2008.

[88] M. Drozdz, L. Moreau, M. Castaings, M. J. S. Lowe, and P. Cawley, "Efficient numerical modelling of absorbing regions for boundaries of guided waves problems," in *Review of progress in quantitative NDE* (D. Thompson and D. Chimenti, eds.), vol. 25, pp. 126–133, Portland, Or, US: Plenum Press, 30 July - 4 August 2006.

[89] M. Drozdz, E. Skelton, R. V. Craster, and M. J. S. Lowe, "Modeling bulk and guided waves in unbounded elastic media using absorbing layers in commercial finite element packages," in *Review of progress in quantitative NDE* (D. Thompson and D. Chimenti, eds.), vol. 26, pp. 87–94, Golden, Co, US: Plenum Press, 22-27 July 2007.

[90] A. Løvstad, "Modeling of transient wave propagation in comsol," in *Proceedings of the 32nd Scandinavian Symposium on Physical Acoustics*, vol. 32, Finse, NO: Norwegian Physical Society, 8-11 February 2009.

[91] P. Belanger, *Feasibility of thickness mapping using ultrasonic guided waves.* PhD thesis, Imperial College, London, 2009.

[92] P. B. Nagy, M. Blodgett, and M. Golis, "Weep hole inspection by circumferential creeping waves," *NDT&E Int.*, vol. 27, pp. 131–142, 1994.

[93] W. Hassan and P. B. Nagy, "Circumferential creeping waves around a fluid-filled cylindrical cavity in an elastic medium," *J. Acoust. Soc. Am.*, vol. 101, no. 5, pp. 2496–2503, 1997.

[94] P. Cawley and D. N. Alleyne, "The use of Lamb waves for the long range inspection of large structures," *Ultrasonics*, vol. 34, pp. 287–290, 1996.

[95] M. B. Kermani, J. Martin, and K. Esaklul, "Materials design strategy: Effects of H_2S/CO_2 corrosion on materials selection," in *Corrosion/2006*, paper 06121, (San Diego, Ca, US), NACE International, 12-16 March 2006.

[96] S. Papavinasam, A. Doiron, and R. W. Revie, "A model to predict internal pitting corrosion of oil and gas pipelines," in *Corrosion/2007*, paper 07658, (Nashville, Tn, US), NACE International, 11-15 March 2007.

[97] R. Nyborg, "Initiation and growth of mesa corrosion attack during CO_2 corrosion of carbon steel," in *Corrosion/98*, paper 48, (San Diego, Ca, US), NACE International, 22-27 March 1998.

[98] E. N. Codaro, R. Z. Nakazato, A. L. Horovistiz, L. M. F. Ribeiro, and L. R. O. Hein, "An image processing method for morphology characterization and pitting corrosion evaluation," *Mater. Sci. Eng.*, vol. A334, pp. 298–306, 2002.

[99] X. Wang, C. F. Ying, and M. Li, "Scattering of antiplane shear waves by a circular cylinder in a traction-free plate," *J. Acoust. Soc. Am.*, vol. 108, no. 3, pp. 913–923, 2000.

[100] E. Domany, O. Entin-Wohlman, and L. Mizrachi, "Multiple scattering formalism: Application to scattering by two spheres," *J. Appl. Phys.*, vol. 56, pp. 132–136, 1984.

[101] M. Grøvlen, E. Bardal, S. Berge, K. Engesvik, P. J. Haagensen, and O. Ørjasæter, "Localized corrosion on offshore tubular structures: Inspection and repair criteria," in *Offshore Technol. Conf.*, pp. 277–288, 1989.

[102] F. Chen and P. Wilcox, "The effect of load on guided wave propagation," *Ultrasonics*, vol. 47, pp. 111–122, 2007.

[103] P. Cawley, M. J. S. Lowe, D. N. Alleyne, B. Pavlakovic, and P. Wilcox, "Practical long range guided wave testing: Applications to pipes and rails," *Mater. Eval.*, vol. 61, no. 1, pp. 66–74, 2003.

[104] D. L. Olson, A. N. Lasseigne, M. Marya, and B. Mishra, "Weld features that differentiate weld and plate corrosion," *J. Pract. Failure Analysis*, vol. 3, no. 5, pp. 43–57, 2003.

[105] E. Gulbrandsen and A. Dugstad, "Corrosion loop studies of preferential weld corrosion and its inhibition in CO_2 environments," in *Corrosion/2005*, paper 05276, (Houston, Tx, US), NACE International, 3-7 April 2005.

[106] B. Hedges, K. Sprague, and T. Bieri, "A review of monitoring and inspection techniques for CO_2 & H_2S corrosion in oil & gas production facilities: Location, location, location!," in *Corrosion/2006*, paper 06120, (San Diego, Ca, US), NACE International, 12-16 March 2006.

[107] S. Papavinasam, R. W. Revie, and A. Doiron, "Predicting internal pitting corrosion of oil and gas pipelines: Review of corrosion science models," in *Corrosion/2005*, paper 05643, (Houston, Tx, US), NACE International, 3-7 April 2005.

[108] R. E. Melchers, "Probabilistic models for corrosion in structural reliability assessment – part 2: Models based on mechanics," *J. Offshore Mech Arctic Eng.*, vol. 125, pp. 273–280, 2003.

[109] R. E. Melchers, "Pitting corrosion of mild steel in marine immersion environment – part 1: Maximum pit depth," *Corrosion*, vol. 60, pp. 824–836, 2004.

[110] G. Engelhart and H.-H. Strehblow, "The determination of the shape of developing corrosion pits," *Corrosion science*, vol. 36, pp. 1711–1725, 1994.

[111] T. Nakai, H. Matsushita, N. Yamamoto, and H. Arai, "Effect of pitting corrosion on local strength of hold frames of bulk carriers (1_{st} report)," *Marine structures*, vol. 17, pp. 403–432, 2004.

[112] R. E. Melchers, "Extreme value statistics and long-term marine pitting corrosion of steel," *Prob. Eng. Mech.*, vol. 23, pp. 482–488, 2008.

[113] Y. M. Gunaltun, D. Supriyatman, and J. Achmad, "Top of line corrosion in multiphase gas lines. A case history," in *Corrosion/99*, paper 36, (San Antonio, Tx, US), NACE International, 25-30 April 1999.

[114] D. N. Alleyne and P. Cawley, "The excitation of Lamb waves in pipes using dry-coupled piezoelectric transducers," *J. Nondestr. Eval.*, vol. 15, no. 1, pp. 11–20, 1996.

[115] D. N. Alleyne, T. Vogt, and P. Cawley, "The choice of torsional or longitudinal excitation in guided wave pipe inspection," *Insight*, vol. 51, no. 7, pp. 373–377, 2009.

[116] R. Carandente and P. Cawley, "A method to estimate the size of corrosion patches with guided waves in pipes," in *Review of progress in quantitative NDE* (D. Thompson and D. Chimenti, eds.), vol. 30, pp. 121–128, San Diego, Ca, US: Plenum Press, 18-23 July 2010.

[117] R. Carandente and P. Cawley, "The effect of complex defect profiles on the reflection of the fundamental torsional mode in pipes," *NDT&E Int.*, vol. 46, pp. 41–47, 2012.

[118] R. Carandente, *Interaction between the fundamental torsional guided wave mode and complex defects in pipes.* PhD thesis, Imperial College, London, 2011.

[119] S. Papavinasam, R. W. Revie, and A. Doiron, "Predicting internal pitting corrosion of oil and gas pipelines: Review of electrochemical models," in *Corrosion/2005*, paper 05644, (Houston, Tx, US), NACE International, 3-7 April 2005.

[120] M. Simonetti, "Multiple scattering: The key to unravel the subwavelength world from the far-field pattern of a scattered wave," *Phys. Rev. E*, vol. 73, p. 036619 (13), 2006.

[121] M. Slaney, A. C. Kak, and L. E. Larsen, "Limitations of imaging with first-order diffraction tomography," *IEEE Trans. Microwave Theory Tech.*, vol. MIT-32, no. 8, pp. 860–874, 1984.

[122] K. Iwata and R. Nagata, "Calculation of refractive index distribution from interferograms using the Born and Rytov's approximation," *Jap. J. Appl. Phys.*, vol. 14, pp. 379–383, 1975.

[123] B. Chen and J. J. Stamnes, "Validity of diffraction tomography based on the first Born and the first Rytov approximations," *Appl. Optics*, vol. 37, pp. 2996–3006, 1998.

[124] F. Natterer, "An error bound for the Born approximation," *Inverse Problems*, vol. 20, pp. 447–452, 2004.

[125] F. J. Harris, "On the use of windows for harmonic analysis with the Discrete Fourier Transform," in *Proceedings of the IEEE*, vol. 66, pp. 51–83, IEEE, January 1978.